Politecnico di Milano
Scuola di Ingegneria Industriale e dell'Informazione
Corso di Laurea in Ingegneria Matematica
Dipartimento di Matematica

DISCONTINUOUS GALERKIN SPECTRAL ELEMENT METHODS FOR THE ELASTO – ACOUSTIC COUPLING

Relatore: Prof.ssa Paola Francesca ANTONIETTI
Correlatore: Dr. Ilario MAZZIERI

Tesi di Laurea Magistrale di:
Samuele MAURI Matr. 817696

Anno Accademico 2014-2015

A mio zio,
senza il quale avrei corso il rischio di crescere milanista

Contents

List of Figures

Ringraziamenti

Non posso, al termine di questo percorso durato gli ultimi cinque anni della mia vita, evitare di soffermarmi a ricordare e ringraziare le persone che mi hanno accompagnato e lo hanno reso speciale.
Senza ordini di classifica, voglio dedicarvi qualche riga di questo elaborato.

Il primo pensiero va a mio nonno: un esempio per me di fierezza e umiltà, e di come un uomo dovrebbe essere. Mi piace credere che anche io, un giorno, sarò per qualcuno la persona che tu oggi sei per me.

A mio fratello mando un abbraccio e tutto il mio sostegno. Ora che intraprendi il cammino che io mi accingo a concludere, spero che questo possa regalarti tante soddisfazioni ed indicarti le strade che conducono a quella Vita che desideri veramente. Faccio e farò sempre il tifo per te!

Ringrazio mio padre e mia madre. Benchè non abbia spesso condiviso con voi i dettagli della mia vita universitaria, il vostro supporto silenzioso è stato un'immancabile costante nonchè fondamenta sulle quali ho costruito l'uomo che sono oggi. Diceva Goethe: *"Sapersi amato dà più forza che sapersi forte"*. Per questo vi ringrazio, per la forza che mi date: grazie di cuore.

Mi piacerebbe ora citare, uno per uno, tutte le persone, gli amici ed i compagni di corso con cui ho condiviso questi cinque anni: siete il regalo più grande che il Poli potesse farmi ed è soprattutto grazie a voi se oggi mi sento più ricco e cresciuto. Grazie per i vostri suggerimenti, i confronti stimolanti, gli scontri di opinioni; ma anche per le feste, gli aperitivi, le serate in via Pecchio...Non riesco a farvi entrare tutti in poche righe, ma vi porto nel cuore e sempre custodirò quel tesoro che è stato per me l'avervi conosciuto.

Ringrazio la professoressa Antonietti e Ilario, che mi hanno invitato a questo lavoro di tesi ed assistito nel suo sviluppo durante questi ultimi mesi. Poche sono le cose più belle del vedere chi, come voi, mette e trasmette passione ed entusiasmo in ciò che fa ogni giorno.

Un pensiero mi sento anche in dovere di dedicarlo, più in generale, a questa scuola e a ciò che mi ha dato. Ho avuto l'opportunità di conoscere gente davvero in gamba, di imparare, di maturare. Nonostante tutti i difetti e le

pecche che il Poli può avere, esco da queste aule con molti ricordi felici e con la sensazione che mi sentirò sempre un po' in debito.

Grazie poi alle mie nonne, che mi ricordano l'importanza e la bellezza delle cose semplici; ai miei zii e cugini, per l'affetto e l'impegno che ci mettono nel farmi sentire a casa.

Ed infine grazie a Te, per la stima che nutri nei miei confronti e per i sorrisi che mi regali. Sei la cosa più bella a cui riesca a pensare.

Grazie a tutti voi, dal profondo del cuore.
Se oggi mi guardo indietro sono orgoglioso, sono felice.

"Arriva fino a dove puoi vedere.
Quando sarai lì, potrai vedere più lontano."
Thomas Carlyle

Abstract

This thesis deals with a transient multiphysical wave problem, commonly used for simulating seismic waves. The model involves acoustic and elastic wave equations and the coupling between them. Starting from an existing mathematical model for the approximation of elastodynamics equations, we present here a more complete and convincing model, which generalizes the previous one, in order to take account also of acoustic effects. We then approximate the resulting model by means of a Discontinuous Galerkin Spectral Element method and present a rigorous theoretical analysis as well as numerical computations.

Introduction

The analysis of seismic wave propagation is of primary importance in geophysics and seismology because of the need for accurate information on earthquakes and on the possible vibrations induced by them.
In this thesis we aim at proposing and analyzing a non-conforming numerical method which is able to simulate elastic and acoustic wave propagation in two and three dimensional configurations, characterized by the presence of irregular interfaces and heterogeneous materials.
The study of elastodynamics equations has been massively investigated in the last years, due to their capability to simulate seismic scenarios and give accurate numerical results. This study is recently grown and enriched by the analysis of materials with different physical nature, such as elastic and acoustic ones, with a special care on their coupling. Different numerical schemes, like Finite Differences and Finite Elements schemes, have been thus adopted and analyzed in both elastodynamics problems, see, e.g., [21, 18, 24, 30, 46, 27], and elasto-acoustic ones, see [8, 7, 6, 34, 22]. Nowadays the discretization method which is mostly used in computational seismology is the Spectral Element (SE) method [13, 29, 36, 48, 16, 28, 35].
SE methods are based on high-order Lagrangian interpolants sampled at the Gauss-Legendre-Lobatto (GLL) quadrature points, and combine the flexibility of finite elements (and their ability to handle complex geometries and boundary conditions) with the accuracy of spectral techniques. SE methods are also well suited for parallel computation, which is needed especially for three-dimensional problems.
However, SE methods usually employ a uniform polynomial degree on the whole domain, and this can lead to a large computational effort.
To increase the flexibility of SE methods, non-conforming high-order techniques, like the Discontinuous Galerkin Spectral Element (DGSE) method [42, 25, 3], are preferable in order to tackle the heavy computational burden. Indeed, with DGSE methods it is possible to deal with a non-uniform polynomial approximation degree as well as a locally varying mesh size. The flexibility of these schemes is thus very useful, especially for complex configurations.

The efficiency of space-time discretization of elastodynamics problems depends also on the time discretization scheme. In this thesis, we consider a second-order explicit central finite difference scheme, namely the leap-frog scheme [11, 13, 14, 19, 30]. This method is the most employed for wave propagation problems and provides a second-order accuracy.
The numerical scheme that we develop in this thesis has been implemented in the SPEED code (SPectral Elements in Elastodynamics with Discontinuous Galerkin, https://speed.mox.polimi.it). SPEED takes advantage of the DGSE method for solving elastodynamics and linear viscoelasticity problems [44, 45, 15, 17].
Thus, we have extended and enriched this code by including also a modelization of the fluid part, where acoustic waves are expressed in terms of the pressure field. In particular, we focus on the elasto-acoustic coupling at the non-matching solid-fluid interface, see, e.g., [23, 5, 49, 12].
The unknowns of the coupled problem are thus the solid displacement, which is solved in the elastic part, and the fluid pressure, which turns out from the resolution of the acoustic wave equation. Another possible formulation of the coupled problem considers as unknown in the acoustic domain the velocity potential (see, e.g., [26, 22]), but this case is not addressed in this thesis. Nevertheless, since the main advantage of the displacement-velocity potential formulation with respect to the displacement-pressure formulation is that preserve the symmetry of the problem, we will consider this formulation later on in the thesis, when we will talk about stability analysis.
The thesis is organized as follows.

- In Chapter 1, we describe the physical phenomena governing seismic waves propagation in elastic and acoustic domain. Moreover, we introduce a general mathematical framework in which the coupled problem is stated and we derive its weak formulation.
- Chapter 2 deals with the numerical methods used for spatial discretization and a detailed description of DGSE method is reported. Moreover, a rigorous stability analysis is carried out.
- In Chapter 3 we derive the algebraic formulation of the problem.
- In Chapter 4 we describe the leap-frog scheme adopted for the time integration scheme.
- In Chapter 5 we present some relevant numerical applications, both concerning two and three dimensional problems. Moreover, we validate the proposed discretization schemes on different benchmarks.

Finally, we draw some conclusions and suggest possible future developments.

Chapter 1

The mathematical model

1.1 The physical problem

Simulating wave propagation is a problem arising in many scientific fields as acoustics, electro-magnetics, fracture mechanics and elastodynamics.
In this thesis, we are interested in elastic and acoustic seismic waves and, in particular, we focus on the coupling between them.
Elastic waves propagate through elastic solid media, whose constitutive relation is subjected to the *Hooke's Law*. These waves are typically the result of earthquakes, explosions or volcanoes and their principal physical effect consists of a vibratory ground motion in the region surrounding the source.
On the other hand, acoustic waves propagate in fluids (liquid and gases) and cause a variation in the pressure field of the media through which they are traveling.
There are two types of seismic waves: body waves and surface waves.
Body waves travel through the interior of the earth and they are divided into two categories: primary (or P) waves and secondary (or S) waves. P-waves are pressure waves which produce ground vibrations longitudinal to their direction of propagation. They can travel through any type of material, both solid and fluid (see Figure 1.1). S-waves are shear waves which displace the ground perpendicular to the direction of propagation. As suggested by their name, these waves are slower and they typically follow P-waves during an earthquake. S-waves can travel only through solid materials, since fluids do not support shear stresses (see Figure 1.1). Thus, in proximity of an elasto-acoustic interface, only the normal components of forces and displacements are balanced, due to a non-penetration condition. This does not happen for the tangential components, since acoustic materials are not compatible with non-slip condition. We will talk more in detail about the coupling later in the thesis.

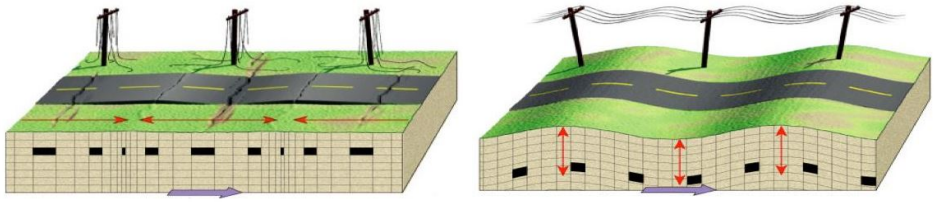

Figure 1.1: Direction of propagation and ground motion for body waves: P-waves (left) and S-waves (right).

Surface waves travel along the earth's surface. They are slower than body waves and, because of their low frequency content, long duration and large amplitude, surface waves are the most destructive type of seismic waves. There are two types of surface waves: Rayleigh waves and Love waves. Rayleigh waves cause the rolling of the ground, i.e. the motion of the rocks below the earth's surface follows the shape of an ellipse (see Figure 1.2). Love waves move the ground from side to side and this horizontal shifting can seriously damage the foundations of buildings (see Figure 1.2).

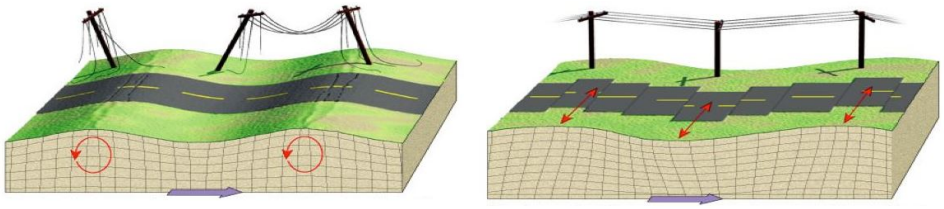

Figure 1.2: Direction of propagation and ground motion for surface waves: Rayleigh waves (left) and Love waves (right).

1.2 Governing equations

In what follows, we concentrate on the multiphysical model used for simulating the propagation of seismic waves. We consider a physical domain $\Omega \subset \mathbb{R}^d$, with $d = 2, 3$. The boundary $\Gamma = \partial\Omega$ is supposed to be composed by three disjoint portions Γ_D, Γ_N and Γ_{NR}. Γ_D and Γ_N are, respectively, the Dirichlet and the Neumann boundaries, where the wave has a prescribed value or where it is subjected to external loads. Γ_{NR} is the part of Γ where the so called non-reflecting (or absorbing) boundary conditions are imposed. These conditions are used to bound the physical domain for numerical approximation.

Absorbing boundary conditions are applied as natural boundary conditions and they are described in the next section of this chapter.
In order to differentiate elastic media from acoustic ones, we use here and in the sequel the subscripts $"e"$ for denoting elastic solids and $"a"$ for acoustics. Thus, the domain Ω may be decomposed as $\Omega = \Omega^e \cup \Omega^a$, where Ω^e and Ω^a stand for the elastic (solid) and acoustic (fluid) sub-domains, respectively (see Figure 1.3).

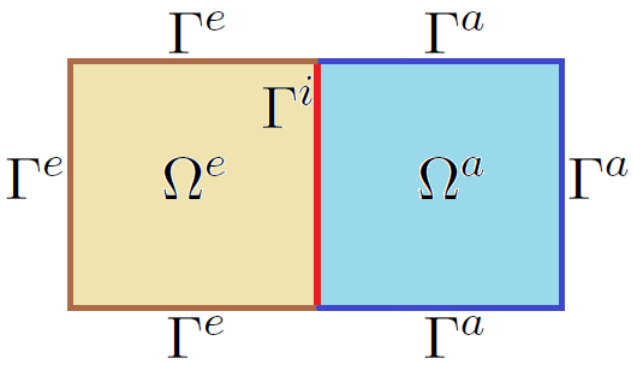

Figure 1.3: Example of a two-dimensional multiphysical domain $\Omega = \Omega^e \cup \Omega^a$. External boundary is split into Γ^e and Γ^a, whereas internal elasto-acoustic interface is called Γ^i.

Analogously, the external boundary Γ is split into Γ^e and Γ^a. Each of these boundaries is subdivided into a Dirichlet portion, a Neumann portion and a non-reflecting portion, such that $\Gamma^{e(a)} = \Gamma_D^{e(a)} \cup \Gamma_N^{e(a)} \cup \Gamma_{NR}^{e(a)}$ with $\Gamma_D^{e(a)} \cap \Gamma_N^{e(a)} \cap \Gamma_{NR}^{e(a)} = \emptyset$.
A crucial role is played by the internal elasto-acoustic interface, denoted by Γ^i, which divides solid materials from fluids. We apply suitable interface conditions in order to model the elasto-acoustic coupling, as it will be detailed later on. Notice that: $\partial\Omega^e = \Gamma^e \cup \Gamma^i$ and $\partial\Omega^a = \Gamma^a \cup \Gamma^i$, or in other words: $\partial\Omega = \partial\Omega^e \cup \partial\Omega^a \setminus \Gamma^i$ (see Figure 1.3).
Having fixed the temporal interval $[0, T]$, with T real and positive, we can write the two governing equations of seismic wave propagation in elastic and acoustic media as follows.
In the sub-domain Ω^e, the deformation of the elastic structure is modeled by the displacement $\mathbf{u} = (u_1, \ldots, u_d)^T$, which satisfies the elastodynamic equation of motion

$$\begin{cases} \rho^e \partial_{tt}\mathbf{u} - \nabla \cdot \sigma(\mathbf{u}) = \mathbf{f}^e, & \text{in } \Omega^e \times (0,T], \\ \mathbf{u} = \mathbf{0}, & \text{on } \Gamma_D^e \times [0,T], \\ \sigma(\mathbf{u})\mathbf{n}^e = \mathbf{t}^e, & \text{on } \Gamma_N^e \times [0,T], \\ \text{non-reflecting boundary conditions}, & \text{on } \Gamma_{NR}^e \times [0,T], \\ \text{coupling boundary conditions}, & \text{on } \Gamma^i \times [0,T], \\ \mathbf{u} = \mathbf{u}_0, & \text{in } \Omega^e \times \{0\}, \\ \partial_t \mathbf{u} = \mathbf{u}_1, & \text{in } \Omega^e \times \{0\}, \end{cases} \tag{1.1}$$

where ρ^e is the density of the elastic material, $\sigma(\mathbf{u})$ is the Cauchy stress tensor and $\mathbf{n}^e = (n_1^e, \ldots, n_d^e)^T$ is the outward pointing unit normal vector on the boundary $\partial\Omega^e$. The vector $\mathbf{f}^e = (f_1^e, \ldots, f_d^e)^T$ models external volume forces, $\mathbf{t}^e = (t_1^e, \ldots, t_d^e)^T$ is the vector of surface tractions on Neumann boundary, $\mathbf{u}_0$ and $\mathbf{u}_1$ are the initial conditions for displacement and velocity, respectively. Without loss of generality (see, for instance [40]), we assume that the medium is rigidly fixed on Γ_D^e.
Finally, the non-reflecting boundary conditions have the effect of introducing a fictitious traction $\tilde{\mathbf{t}}^e$ on Γ_{NR}^e, that will be defined later in this chapter (cf. [47, 11], for example). At the same way, suitable coupling conditions introduce internal surface stresses on the interface Γ^i, which depend on the acoustic pressure field p (cf. [23]).
In geophysical applications a modification of the equation of motion is introduced, in order to better modeling the behavior of viscoelastic materials. This turns out in an additional damping term, written in the form

$$\mathbf{f}_{visc}^e = -2\rho^e \xi \partial_t \mathbf{u} - \rho^e \xi^2 \mathbf{u}, \tag{1.2}$$

where ξ is a suitable decay factor with dimension the inverse of time, as in [11]. The viscoelastic force $\mathbf{f}_{visc}^e$ may be added to the volume forces vector $\mathbf{f}^e$ in order to prevent unphysical oscillations in the propagation wave.
As previously mentioned, the constitutive relation of elastic materials follows the *Hooke's law*, which relates stresses and strains with the fourth-order *Hooke's tensor* C, such that

$$\sigma(\mathbf{u}) = C\big[\epsilon(\mathbf{u})\big],$$

where $\epsilon(\mathbf{u})$ is the infinitesimal strain tensor, that is the symmetric part of the displacement gradient tensor

$$\epsilon(\mathbf{u}) = \frac{1}{2}\big[\nabla\mathbf{u} + (\nabla\mathbf{u})^T\big].$$

In the case of isotropic linear elasticity (which is the case considered here), the fourth-order tensor C satisfies the following symmetries

$$C_{ijkl} = C_{jikl} = C_{ijlk} = C_{klij} \qquad \forall i,j,k,l = 1,\ldots,d.$$

Thus, its action on the strain tensor $\epsilon(\mathbf{u})$ is characterized by only two parameters and the Cauchy stress tensor $\sigma(\mathbf{u})$ may be now written in the following form

$$\sigma(\mathbf{u}) = \lambda tr[\epsilon(\mathbf{u})]I + 2\mu\epsilon(\mathbf{u}),$$

where I is the $d \times d$ identity tensor and λ and μ are the so-called *Lamé parameters*. They are characteristics of each elastic material (like the density) and they are related to P and S body waves. Denoting by c_p and c_s the velocity of compressional and shear waves, respectively, we have

$$c_p = \sqrt{\frac{\lambda + 2\mu}{\rho^e}}, \qquad c_s = \sqrt{\frac{\mu}{\rho^e}}, \tag{1.3}$$

or, equivalently

$$\lambda = \rho^e(c_p^2 - 2c_s^2), \qquad \mu = \rho^e c_s^2. \tag{1.4}$$

Differently from elastic media, in the acoustic sub-domain Ω^a the seismic wave propagation is modeled by the pressure field p, which satisfies the following equation

$$\begin{cases} \frac{1}{\rho^a c^2}\partial_{tt}p - \nabla \cdot \left(\frac{1}{\rho^a}\nabla p\right) = f^a, & \text{in } \Omega^a \times (0,T], \\ p = 0, & \text{on } \Gamma_D^a \times [0,T], \\ \frac{1}{\rho^a}\nabla p \cdot \mathbf{n}^a = t^a, & \text{on } \Gamma_N^a \times [0,T], \\ \text{non-reflecting boundary conditions}, & \text{on } \Gamma_{NR}^a \times [0,T], \\ \text{coupling boundary conditions}, & \text{on } \Gamma^i \times [0,T], \\ p = p_0, & \text{in } \Omega^a \times \{0\}, \\ \partial_t p = p_1, & \text{in } \Omega^a \times \{0\}, \end{cases} \tag{1.5}$$

where ρ^a is the density of the fluid, c is the speed of the acoustic wave and $\mathbf{n}^a = (n_1^a, \ldots, n_d^a)^T$ is the outward pointing unit normal vector on the boundary $\partial\Omega^a$, moreover, f^a represents external volume forces, t^a is the surface load on the Neumann boundary, p_0 and p_1 are the initial conditions for the pressure and its time derivative, respectively.
Since the pressure is defined up to a constant; we consider in this thesis, without loss of generality, homogenous Dirichlet boundary conditions on Γ_D^a. Non-reflecting boundary conditions are particular natural boundary conditions which have the effect of introducing a fictitious Neumann load $\tilde{t}^a$ on Γ_{NR}^a (cf. [37]). They will be discussed in the next section of this chapter. Coupling conditions are still fictitious Neumann conditions and they introduce an internal load on the surface Γ^i, which depend on the solid displacement $\mathbf{u}$ (cf. [23]).

1.3 Non-reflecting boundary conditions

As mentioned before, absorbing, or non-reflecting, boundary conditions are natural boundary conditions which are used to bound physical domains in numerical simulations of wave propagation.
Unlike Dirichlet or Neumann boundary conditions, which lead to a total reflection of an impinging wave on the boundary of the computational domain, absorbing boundary conditions should ideally be able to propagate an incident wave without any reflection.
However, exact non-reflecting boundary conditions involve inverse and direct Fourier transforms in both time and space, through the multiplication by a non polynomial function in the Fourier variables. Thus, in practice, absorbing boundary conditions are approximated with some truncated Taylor expansions, which yield a small reflection.
For simplicity, we now show absorbing boundary conditions in a two-dimensional setting. Analogous formulation can be obtained in three dimension. Let $\mathbf{n}^e = (n_1^e, n_2^e)^T$ be the outward pointing unit normal vector to $\partial\Omega^e$ and $\boldsymbol{\tau}^e = (\tau_1^e, \tau_2^e)^T$ be the unit tangential vector on the boundary Γ_{NR}^e. Since we are now considering firstly elastic materials, the subscript $''e''$ will be sometimes omitted. The zero-order non-reflecting boundary conditions for elastic materials take the following form

$$\begin{aligned} \partial_n(\mathbf{u}\cdot\mathbf{n}^e) &= -\frac{1}{c_p}\partial_t(\mathbf{u}\cdot\mathbf{n}^e), \\ \partial_n(\mathbf{u}\cdot\boldsymbol{\tau}^e) &= -\frac{1}{c_s}\partial_t(\mathbf{u}\cdot\boldsymbol{\tau}^e). \end{aligned} \tag{1.6}$$

In order to derive the fictitious traction $\tilde{\mathbf{t}}^e = \tilde{\sigma}(\mathbf{u})\mathbf{n}^e$ on Γ_{NR}^e we proceed as follows.
We rewrite the Cauchy stress tensor $\sigma(\mathbf{u})$ in the local coordinate system $\{\boldsymbol{\tau}, \mathbf{n}\}$ as

$$\begin{aligned} \sigma_{\tau\tau} &= (\lambda+2\mu)\partial_\tau u_\tau + \lambda\partial_n u_n, \\ \sigma_{nn} &= (\lambda+2\mu)\partial_n u_n + \lambda\partial_\tau u_\tau, \\ \sigma_{\tau n} &= \mu\big(\partial_n u_\tau + \partial_\tau u_n\big), \end{aligned}$$

and therefore, using relations (1.6), we get

$$\begin{aligned} \sigma_{\tau\tau} &= (\lambda+2\mu)\partial_\tau u_\tau - \frac{\lambda}{c_p}\partial_t u_n, \\ \sigma_{nn} &= -\frac{\lambda+2\mu}{c_p}\partial_t u_n + \lambda\partial_\tau u_\tau, \\ \sigma_{\tau n} &= \mu\Big(\partial_\tau u_n - \frac{1}{c_s}\partial_t u_\tau\Big). \end{aligned}$$

In this system of coordinates, the force per unit surface $\tilde{\mathbf{t}}^e$ is thus

$$\tilde{\mathbf{t}}^e = \begin{bmatrix} \tilde{t}^e_\tau \\ \tilde{t}^e_n \end{bmatrix} = \begin{bmatrix} \sigma_{\tau n} \\ \sigma_{nn} \end{bmatrix} = \begin{bmatrix} \mu\big(\partial_\tau u_n - \frac{1}{c_s}\partial_t u_\tau\big) \\ -\frac{\lambda+2\mu}{c_p}\partial_t u_n + \lambda\partial_\tau u_\tau \end{bmatrix}.$$

Computing in the above equation the normal and tangential derivatives as $\partial_n = n_1\partial_{x_1} + n_2\partial_{x_2}$ and $\partial_\tau = \tau_1\partial_{x_1} + \tau_2\partial_{x_2} = n_2\partial_{x_1} - n_1\partial_{x_2}$ we obtain

$$\tilde{\mathbf{t}}^e = \begin{bmatrix} \mu\Big[n_1 n_2\big(\partial_{x_1}u_1 - \partial_{x_2}u_2\big) \\ \qquad\qquad - n_1^2\partial_{x_2}u_1 + n_2^2\partial_{x_1}u_2 - \dfrac{1}{c_s}\big(n_2\partial_t u_1 - n_1\partial_t u_2\big)\Big] \\ -\dfrac{\lambda+2\mu}{c_p}\big(n_1\partial_t u_1 + n_2\partial_t u_2\big) \\ \qquad\qquad + \lambda\Big[n_2^2\partial_{x_1}u_1 - n_1 n_2\big(\partial_{x_2}u_1 + \partial_{x_1}u_2\big) + n_1^2\partial_{x_2}u_2\Big] \end{bmatrix}.$$

Finally, since $\tilde{\mathbf{t}}^e$ is expressed in the local coordinate system, we project it on the global coordinate system and, using the relations (1.3) and (1.4), we express everything in terms of c_p and c_s. Thus, we get

$$\tilde{\mathbf{t}}^e = \begin{bmatrix} \tilde{t}^e_1 \\ \tilde{t}^e_2 \end{bmatrix} = \begin{bmatrix} \tilde{t}^e_\tau n_2 + \tilde{t}^e_n n_1 \\ \tilde{t}^e_n n_2 - \tilde{t}^e_\tau n_1 \end{bmatrix} = -\rho^e \begin{bmatrix} \big(c_p n_1^2 + c_s n_2^2\big)\partial_t u_1 + n_1 n_2\big(c_p - c_s\big)\partial_t u_2 \\ n_1 n_2\big(c_p - c_s\big)\partial_t u_1 + \big(c_p n_2^2 + c_s n_1^2\big)\partial_t u_2 \end{bmatrix}. \tag{1.7}$$

Clearly, a better approximation of the exact conditions will ensure less reflection of incident seismic waves. Thus, more accurate non-reflecting boundary conditions are the first-order ones

$$\begin{aligned} \partial_n(\mathbf{u}\cdot\mathbf{n}^e) &= -\frac{1}{c_p}\partial_t(\mathbf{u}\cdot\mathbf{n}^e) - \frac{c_p - c_s}{c_p}\partial_\tau(\mathbf{u}\cdot\boldsymbol{\tau}^e), \\ \partial_n(\mathbf{u}\cdot\boldsymbol{\tau}^e) &= -\frac{1}{c_s}\partial_t(\mathbf{u}\cdot\boldsymbol{\tau}^e) - \frac{c_p - c_s}{c_s}\partial_\tau(\mathbf{u}\cdot\mathbf{n}^e). \end{aligned} \tag{1.8}$$

The expression of the consequent fictitious traction $\tilde{\mathbf{t}}^e$ can be derived by following the same steps that previously brought us to get (1.7). In this case we lead to

$$\tilde{\mathbf{t}}^e = -\rho^e \begin{bmatrix} c_s\big(c_p - 2c_s\big)\Big[n_2\big(n_1^2 + n_2^2\big)\partial_{x_1}u_2 - n_1\big(n_1^2 + n_2^2\big)\partial_{x_2}u_2\Big] \\ \qquad\qquad + \big(c_p n_1^2 + c_s n_2^2\big)\partial_t u_1 + n_1 n_2\big(c_p - c_s\big)\partial_t u_2 \\ c_s\big(c_p - 2c_s\big)\Big[n_1\big(n_1^2 + n_2^2\big)\partial_{x_2}u_1 - n_2\big(n_1^2 + n_2^2\big)\partial_{x_1}u_1\Big] \\ \qquad\qquad + n_1 n_2\big(c_p - c_s\big)\partial_t u_1 + \big(c_p n_2^2 + c_s n_1^2\big)\partial_t u_2 \end{bmatrix}. \tag{1.9}$$

In the three dimensional case, absorbing boundary conditions (1.8) become

$$\begin{aligned}
\partial_n(\mathbf{u}\cdot\mathbf{n}^e) &= -\frac{1}{c_p}\partial_t(\mathbf{u}\cdot\mathbf{n}^e) - \frac{c_p-c_s}{c_p}\Big[\partial_{\tau_1}(\mathbf{u}\cdot{\boldsymbol{\tau_1}}^e) + \partial_{\tau_2}(\mathbf{u}\cdot{\boldsymbol{\tau_2}}^e)\Big],\\
\partial_n(\mathbf{u}\cdot{\boldsymbol{\tau_1}}^e) &= -\frac{1}{c_s}\partial_t(\mathbf{u}\cdot{\boldsymbol{\tau_1}}^e) - \frac{c_p-c_s}{c_s}\partial_{\tau_1}(\mathbf{u}\cdot\mathbf{n}^e),\\
\partial_n(\mathbf{u}\cdot{\boldsymbol{\tau_2}}^e) &= -\frac{1}{c_s}\partial_t(\mathbf{u}\cdot{\boldsymbol{\tau_2}}^e) - \frac{c_p-c_s}{c_s}\partial_{\tau_2}(\mathbf{u}\cdot\mathbf{n}^e),
\end{aligned} \tag{1.10}$$

where ${\boldsymbol{\tau_1}}^e$ and ${\boldsymbol{\tau_2}}^e$ are two mutually orthogonal unit normal vectors on the plane orthogonal to $\mathbf{n}^e$ (that is the tangent plane to the surface Γ^e_{NR}), such that $\{{\boldsymbol{\tau_1}}^e, {\boldsymbol{\tau_2}}^e, \mathbf{n}^e\}$ is a right handed Cartesian system. Starting from (1.10) it is possible to deduce an expression of the three dimensional $\tilde{\mathbf{t}}^e$ analogous to (1.9).

For acoustic materials, the zero-order non-reflecting boundary conditions on Γ^a_{NR} are similar to (1.6). Thus, the acoustic wave should satisfy

$$\partial_n p = -\frac{1}{c}\partial_t p. \tag{1.11}$$

This means that the fictitious surface force $\tilde{t}^a$ is simply

$$\tilde{t}^a = \frac{1}{\rho^a}\nabla\tilde{p}\cdot\mathbf{n}^a = -\frac{1}{\rho^a c}\partial_t p. \tag{1.12}$$

1.4 Coupling conditions

At the solid-fluid interface Γ^i, the non-penetration condition requires that the normal component of the mechanical surface velocity of the solid $\mathbf{v}^e$ must coincide with the normal component of the acoustic velocity of the fluid $\mathbf{v}^a$. Thus, the following relation holds

$$\mathbf{v}^e\cdot\mathbf{n}^e + \mathbf{v}^a\cdot\mathbf{n}^a = 0.$$

Computing a time derivative, we get

$$\partial_t\mathbf{v}^e\cdot\mathbf{n}^e + \partial_t\mathbf{v}^a\cdot\mathbf{n}^a = 0.$$

However, $\partial_t\mathbf{v}^e = \partial_{tt}\mathbf{u}$ and $\partial_t\mathbf{v}^a = -\frac{1}{\rho^a}\nabla p$ (using the acoustic velocity potential ψ such that $\mathbf{v}^a = -\nabla\psi$ and $p = \rho^a\partial_t\psi$). Therefore, the first elasto-acoustic coupling condition is

$$\partial_{tt}\mathbf{u}\cdot\mathbf{n}^e - \frac{1}{\rho^a}\nabla p\cdot\mathbf{n}^a = 0. \tag{1.13}$$

We note that $\mathbf{n}^e$ and $\mathbf{n}^a$ are the outward pointing unit normal vector on the boundary Γ^i, with respect to the solid (elastic) and the fluid (acoustic) part, respectively.
In addition, one has to consider the continuity of normal stresses at the internal surface Γ^i. In other words, the stress applied by the solid on the fluid must be equal to the stress applied by the fluid on the solid. Since the fluid pressure acts as a normal force on the solid media, a second elasto-acoustic coupling condition is given by

$$\sigma(\mathbf{u})\mathbf{n}^e - p\mathbf{n}^a = 0. \tag{1.14}$$

This latest condition means that, in proximity of a solid-fluid interface, the internal stresses are only pressure stresses and there are no shear stresses. This is in according with the fact that acoustic materials, since they are inviscid, do not support no-slip conditions and shear forces, i.e., only P-waves can propagate through them.

1.5 The variational formulation

Before recasting the problem in a variational form, we introduce the following notation:

$$a \cdot b = ab, \qquad \big(a,b\big)_\Omega = \int_\Omega a \cdot b d\Omega \qquad \forall a, b \in L^2(\Omega),$$

$$\mathbf{a} \cdot \mathbf{b} = \sum_{i=1}^{d} a_i b_i, \qquad \big(\mathbf{a},\mathbf{b}\big)_\Omega = \int_\Omega \mathbf{a} \cdot \mathbf{b} d\Omega \qquad \forall \mathbf{a}, \mathbf{b} \in \boldsymbol{L^2}(\Omega),$$

$$A : B = \sum_{i,j=1}^{d} A_{ij} B_{ij}, \qquad \big(A,B\big)_\Omega = \int_\Omega A : B d\Omega \qquad \forall A, B \in \big[\boldsymbol{L^2}(\Omega)\big]^d,$$

where $\boldsymbol{L^2}(\Omega) = \big[L^2(\Omega)\big]^d$ and $\big[\boldsymbol{L^2}(\Omega)\big]^d = \big[L^2(\Omega)\big]^{d\times d}$.
We recall that

$$L^2(\Omega) = \Big\{ f : \Omega \to \mathbb{R} \text{ such that } \int_\Omega f^2 d\Omega < +\infty \Big\},$$

and

$$H^1(\Omega) = \Big\{ f : \Omega \to \mathbb{R} \text{ such that } \int_\Omega f^2 d\Omega < +\infty \text{ and } \int_\Omega |\nabla f|^2 d\Omega < +\infty \Big\},$$

see [39, p. 17,20].
Let us now introduce the following Sobolev spaces (see [1]):

$$\mathbf{W} = \{\mathbf{w} \in \boldsymbol{H^1}(\Omega^e) \text{ such that } \mathbf{w} = \mathbf{0} \text{ on } \Gamma^e_D\},$$
$$V = \{v \in H^1(\Omega^a) \text{ such that } v = 0 \text{ on } \Gamma^a_D\}.$$

Choosing a test function $\mathbf{w} \in \mathbf{W}$, multiplying equation (1.1), integrating by parts using the *Green's formula* and applying boundary and coupling conditions (1.14), we get the weak formulation of the elastodynamic equation of motion

$$\left(\rho^e \partial_{tt}\mathbf{u}, \mathbf{w}\right)_{\Omega^e} + \mathcal{A}^e(\mathbf{u}, \mathbf{w}) + \mathcal{C}^e(p, \mathbf{w}) = \mathcal{L}^e(\mathbf{w}) \qquad \forall \mathbf{w} \in \mathbf{W}, \tag{1.15}$$

where, using the previous notation, we have set

$$\begin{aligned}
\mathcal{A}^e(\mathbf{u}, \mathbf{w}) &= \left(\sigma(\mathbf{u}), \epsilon(\mathbf{w})\right)_{\Omega^e}, \\
\mathcal{C}^e(p, \mathbf{w}) &= -\left(p\mathbf{n}^a, \mathbf{w}\right)_{\Gamma^i} = \left(p\mathbf{n}^e, \mathbf{w}\right)_{\Gamma^i}, \\
\mathcal{L}^e(\mathbf{w}) &= \left(\mathbf{f}^e, \mathbf{w}\right)_{\Omega^e} + \left(\mathbf{t}^e, \mathbf{w}\right)_{\Gamma^e_N} + \left(\tilde{\mathbf{t}}^e, \mathbf{w}\right)_{\Gamma^e_{NR}}.
\end{aligned}$$

We proceed analogously for the acoustic equation. We choose a test function $v \in V$, we multiply equation (1.5) and, integrating by parts using *Green's formula* and applying boundary and coupling conditions (1.13), we get the weak formulation of the acoustic wave equation

$$\left(\frac{1}{\rho^a c^2}\partial_{tt}p, v\right)_{\Omega^a} + \mathcal{A}^a(p, v) + \mathcal{C}^a(\mathbf{u}, v) = \mathcal{L}^a(v) \qquad \forall v \in V, \tag{1.16}$$

where,

$$\begin{aligned}
\mathcal{A}^a(p, v) &= \left(\frac{1}{\rho^a}\nabla p, \nabla v\right)_{\Omega^a}, \\
\mathcal{C}^a(\mathbf{u}, v) &= -\left(\partial_{tt}\mathbf{u} \cdot \mathbf{n}^e, v\right)_{\Gamma^i} = \left(\partial_{tt}\mathbf{u} \cdot \mathbf{n}^a, v\right)_{\Gamma^i}, \\
\mathcal{L}^a(v) &= \left(f^a, v\right)_{\Omega^a} + \left(t^a, v\right)_{\Gamma^a_N} + \left(\tilde{t}^a, v\right)_{\Gamma^a_{NR}}.
\end{aligned}$$

As one can see, equations (1.15) and (1.16) contain the coupling terms $\mathcal{C}^e(\cdot, \cdot)$ and $\mathcal{C}^a(\cdot, \cdot)$, respectively.
Thus, the weak formulation of the coupled elasto-acoustic wave propagation problem is:

$$\begin{aligned}
&\text{find the couple } (\mathbf{u}, p) \text{ such that } \forall t \in [0, T] \ (\mathbf{u}(t), p(t)) \in (\mathbf{W} \times V) \text{ and} \\
&\quad \left(\rho^e \partial_{tt}\mathbf{u}, \mathbf{w}\right)_{\Omega^e} + \mathcal{A}^e(\mathbf{u}, \mathbf{w}) + \mathcal{C}^e(p, \mathbf{w}) = \mathcal{L}^e(\mathbf{w}) \qquad \forall \mathbf{w} \in \mathbf{W}, \\
&\quad \left(\frac{1}{\rho^a c^2}\partial_{tt}p, v\right)_{\Omega^a} + \mathcal{A}^a(p, v) + \mathcal{C}^a(\mathbf{u}, v) = \mathcal{L}^a(v) \qquad \forall v \in V.
\end{aligned} \tag{1.17}$$

In presence of non-homogeneous Dirichlet boundary conditions, all that we have previously done is still valid. Simply, we would have to add at the right-hand side terms of (1.15) and (1.16) a suitable recovery of the Dirichlet boundaries data.

1.6 Stability analysis

The aim of this section is to prove suitable stability bounds for problem (1.17).
Before that, we recall the following result, see [20, 41] for the proof.
Firstly, we assume both the elastic and the acoustic density functions strictly positive and bounded, i.e.,

$$\rho^e \in L^\infty(\Omega^e) \text{ and } \rho^e_m \leq \rho^e(\mathbf{x}) \leq \rho^e_M \quad \forall \mathbf{x} \in \Omega^e,$$
$$\rho^a \in L^\infty(\Omega^a) \text{ and } \rho^a_m \leq \rho^a(\mathbf{x}) \leq \rho^a_M \quad \forall \mathbf{x} \in \Omega^a,$$

for some $\rho^{e(a)}_m, \rho^{e(a)}_M > 0$. Moreover, we suppose

$$c \in L^\infty(\Omega^a) \text{ and } c_m \leq c(\mathbf{x}) \leq c_M \quad \forall \mathbf{x} \in \Omega^a,$$

for some $c_m, c_M > 0$. On, the other hand, in the elastic part, we suppose that the Hooke's tensor C is bounded and positive definite, that is

$$C_m \sum_{i,j=1}^{d} \epsilon^2_{ij} \leq \sum_{i,j,k,l=1}^{d} C_{ijkl}\epsilon_{kl}\epsilon_{ij} \leq C_M \sum_{i,j=1}^{d} \epsilon^2_{ij} \quad \forall \epsilon \in \mathbb{R}^{d\times d}, \epsilon \neq 0,$$

for some $C_m, C_M > 0$.
The problem (1.17) is well-posed and thus it has a unique solution $(\mathbf{u}, p)$, see [7] for further details about the proof.
For simplicity, we consider a two-dimensional setting with zero-order absorbing boundary conditions on $\Gamma_{NR} = \Gamma^e_{NR} \cup \Gamma^a_{NR}$ and without volume forces, i.e., $\mathbf{f}^e = \mathbf{0}$ and $f^a = 0$. Moreover, we suppose to have homogeneous Neumann boundary conditions on $\Gamma_N = \Gamma^e_N \cup \Gamma^a_N$, i.e., $\mathbf{t}^e = \mathbf{0}$ and $t^a = 0$. The general case can be obtained similarly. Then, we suppose that both Γ^e_D and Γ^a_D are not empty. Finally, in order to have the same unit of measure in both elastic and acoustic subdomains, the fluid pressure is replaced by the velocity potential ψ. As we have already mentioned in Section 1.4, this substitution is nothing more that a variable changing, since the following relation holds

$$p = \rho^a \partial_t \psi.$$

We thus rewrite equations (1.15) – (1.16) as

$$\begin{aligned}
&\big(\rho^e \partial_{tt}\mathbf{u}, \mathbf{w}\big)_{\Omega^e} + \big(\sigma(\mathbf{u}), \epsilon(\mathbf{w})\big)_{\Omega^e} + \big(E\partial_t \mathbf{u}, \mathbf{w}\big)_{\Gamma^e_{NR}} - \big(\rho^a \partial_t \psi \mathbf{n}^a, \mathbf{w}\big)_{\Gamma^i} = 0,\\
&\Big(\frac{\rho^a}{c^2}\partial_{tt}\psi, v\Big)_{\Omega^a} + \big(\rho^a \nabla\psi, \nabla v\big)_{\Omega^a} + \Big(\frac{\rho^a}{c}\partial_t\psi, v\Big)_{\Gamma^a_{NR}} - \big(\rho^a \partial_t \mathbf{u}\cdot\mathbf{n}^e, v\big)_{\Gamma^i} = 0,
\end{aligned} \tag{1.18}$$

$\forall \mathbf{w} \in \mathbf{W}$ and $\forall v \in V$, where, from (1.7),

$$E = \rho^e \begin{bmatrix} c_p n_1^2 + c_s n_2^2 & (c_p - c_s) n_1 n_2 \\ (c_p - c_s) n_1 n_2 & c_s n_1^2 + c_p n_2^2 \end{bmatrix}.$$

We now define the following *energy norms*:

$$\|\mathbf{u}(t)\|^2_{E^e} = \|\sqrt{\rho^e}\partial_t\mathbf{u}(t)\|^2_{\mathbf{L}^2(\Omega^e)} + \left\|C^{\frac{1}{2}}[\epsilon(\mathbf{u}(t))]\right\|^2_{[\mathbf{L}^2(\Omega^e)]^2} \quad \forall t \in [0,T],$$

and

$$\|\psi(t)\|^2_{E^a} = \left\|\frac{\sqrt{\rho^a}}{c}\partial_t\psi(t)\right\|^2_{L^2(\Omega^a)} + \|\sqrt{\rho^a}\nabla\psi(t)\|^2_{\mathbf{L}^2(\Omega^a)} \quad \forall t \in [0,T],$$

where $C^{\frac{1}{2}}$ is the fourth-order tensor such that $C^{\frac{1}{2}}\left[C^{\frac{1}{2}}[\epsilon]\right] = C[\epsilon]\ \forall \epsilon \in \mathbb{R}^{2\times 2}$. We recall that, since C is symmetric and positive definite, also $C^{\frac{1}{2}}$ is symmetric and positive definite. Thus

$$\begin{aligned}\sigma : \epsilon = C[\epsilon] : \epsilon = C^{\frac{1}{2}}\left[C^{\frac{1}{2}}[\epsilon]\right] : \epsilon = \sum_{i,j,k,l,m,n=1}^{2} C^{\frac{1}{2}}_{ijkl}C^{\frac{1}{2}}_{klmn}\epsilon_{mn}\epsilon_{ij} = \\ = \sum_{k,l=1}^{2}\Big(\sum_{i,j=1}^{2} C^{\frac{1}{2}}_{klij}\epsilon_{ij}\Big)\Big(\sum_{m,n=1}^{2} C^{\frac{1}{2}}_{klmn}\epsilon_{mn}\Big) = C^{\frac{1}{2}}[\epsilon] : C^{\frac{1}{2}}[\epsilon].\end{aligned} \tag{1.19}$$

We choose the test functions $\mathbf{w} = \partial_t\mathbf{u}(t) \in \mathbf{W}$, $v = \partial_t\psi(t) \in V$ and, using the relation (1.19), we rewrite equations (1.18) $\forall t \in [0,T]$ as

$$\frac{1}{2}\frac{d}{dt}\|\mathbf{u}(t)\|^2_{E^e} + \big(E\partial_t\mathbf{u}(t), \partial_t\mathbf{u}(t)\big)_{\Gamma^e_{NR}} - \big(\rho^a\partial_t\psi(t)\mathbf{n}^a, \partial_t\mathbf{u}(t)\big)_{\Gamma^i} = 0, \tag{1.20}$$

$$\frac{1}{2}\frac{d}{dt}\|\psi(t)\|^2_{E^a} + \Big(\frac{\rho^a}{c}\partial_t\psi(t), \partial_t\psi(t)\Big)_{\Gamma^a_{NR}} - \big(\rho^a\partial_t\mathbf{u}(t)\cdot\mathbf{n}^e, \partial_t\psi(t)\big)_{\Gamma^i} = 0. \tag{1.21}$$

Since the matrix E is positive definite, the second terms of both the equations are non-negative in $[0,T]$. Thus, we sum the equations (1.20) and (1.21) and we get

$$\frac{d}{dt}\|\mathbf{u}(t)\|^2_{E^e} + \frac{d}{dt}\|\psi(t)\|^2_{E^a} \leq 0 \qquad \forall t \in [0,T]. \tag{1.22}$$

The two coupling terms vanish since they are equal and opposite (we recall that $\mathbf{n}^e = -\mathbf{n}^a$ on Γ^i).
We now integrate in time the inequality (1.22) and we get the following stability estimate:

$$\|\mathbf{u}(t)\|^2_{E^e} + \|\psi(t)\|^2_{E^a} \leq \|\mathbf{u}(0)\|^2_{E^e} + \|\psi(0)\|^2_{E^a} \quad \forall t \in [0,T]. \tag{1.23}$$

We note that, even if there are no external forces, the system is dissipative, due to the presence of absorbing boundary conditions on $\Gamma_{NR} = \Gamma^e_{NR} \cup \Gamma^a_{NR}$. It is straightforward to see that, if $\Gamma_{NR} = \emptyset$, the inequality (1.22) become an equality and thus the total energy would be conserved in time.

We now suppose to have volume forces $\mathbf{f}^e$ and f^a_ψ such that $\mathbf{f}^e(t) \in \mathbf{L}^2(\Omega^e)$

and $f_\psi^a(t) \in L^2(\Omega^a)\ \forall t \in [0,T]$. Thanks to the hypothesis on ρ^e, ρ^a and c, and using *Cauchy-Schwarz* and *Young* inequalities, the following bounds hold:

$$\begin{aligned}\big(\mathbf{f}^e(t), \mathbf{w}\big)_{\Omega^e} &\leq \frac{1}{2\rho_m^e}\|\mathbf{f}^e(t)\|^2_{\mathbf{L}^2(\Omega^e)} + \frac{1}{2}\|\sqrt{\rho^e}\mathbf{w}\|^2_{\mathbf{L}^2(\Omega^e)},\\ \big(\rho^a f_\psi^a(t), v\big)_{\Omega^a} &\leq \frac{\rho_M^a c_M^2}{2}\|f_\psi^a(t)\|^2_{L^2(\Omega^a)} + \frac{1}{2}\Big\|\frac{\sqrt{\rho^a}}{c}v\Big\|^2_{L^2(\Omega^a)},\end{aligned} \tag{1.24}$$

$\forall \mathbf{w} \in \mathbf{W}$, $\forall v \in V$ and $\forall t \in [0,T]$.
We use these results in inequality (1.22), which now read as

$$\begin{aligned}\frac{d}{dt}\|\mathbf{u}(t)\|^2_{E^e} + \frac{d}{dt}\|\psi(t)\|^2_{E^a} \leq& 2\big(\mathbf{f}^e(t), \partial_t\mathbf{u}(t)\big)_{\Omega^e} + 2\big(\rho^a f_\psi^a(t), \partial_t\psi(t)\big)_{\Omega^a}\\ \leq& \frac{1}{\rho_m^e}\|\mathbf{f}^e(t)\|^2_{\mathbf{L}^2(\Omega^e)} + \|\sqrt{\rho^e}\partial_t\mathbf{u}(t)\|^2_{\mathbf{L}^2(\Omega^e)}\\ &+ \rho_M^a c_M^2\|f_\psi^a(t)\|^2_{L^2(\Omega^a)} + \Big\|\frac{\sqrt{\rho^a}}{c}\partial_t\psi(t)\Big\|^2_{L^2(\Omega^a)}\\ \leq& \frac{1}{\rho_m^e}\|\mathbf{f}^e(t)\|^2_{\mathbf{L}^2(\Omega^e)} + \|\mathbf{u}(t)\|^2_{E^e}\\ &+ \rho_M^a c_M^2\|f_\psi^a(t)\|^2_{L^2(\Omega^a)} + \|\psi(t)\|^2_{E^a} \quad \forall t \in [0,T].\end{aligned} \tag{1.25}$$

We now integrate in time the inequality (1.25) and we get $\forall t \in [0,T]$,

$$\begin{aligned}&\|\mathbf{u}(t)\|^2_{E^e} + \|\psi(t)\|^2_{E^a} \leq \|\mathbf{u}(0)\|^2_{E^e} + \|\psi(0)\|^2_{E^a}\\ &+ \int_0^t \Big(\|\mathbf{u}(\tau)\|^2_{E^e} + \|\psi(\tau)\|^2_{E^a} + \frac{1}{\rho_m^e}\|\mathbf{f}^e(\tau)\|^2_{\mathbf{L}^2(\Omega^e)} + \rho_M^a c_M^2\|f_\psi^a(\tau)\|^2_{L^2(\Omega^a)}\Big)d\tau.\end{aligned} \tag{1.26}$$

We finally apply *Gronwall's lemma* (see [39, p. 28]), which gives us the following stability estimate:

$$\begin{aligned}&\|\mathbf{u}(t)\|^2_{E^e} + \|\psi(t)\|^2_{E^a} \leq e^t\Bigg[\|\mathbf{u}(0)\|^2_{E^e} + \|\psi(0)\|^2_{E^a}\\ &+ \int_0^t \Big(\frac{1}{\rho_m^e}\|\mathbf{f}^e(\tau)\|^2_{\mathbf{L}^2(\Omega^e)} + \rho_M^a c_M^2\|f_\psi^a(\tau)\|^2_{L^2(\Omega^a)}\Big)d\tau\Bigg], \quad \forall t \in [0,T].\end{aligned} \tag{1.27}$$

Note that, due to the presence of the exponential term, this estimate is meaningful as long as the observed time interval is bounded by a finite $T > 0$. Otherwise, for $T \to \infty$ the stability estimate (1.27) becomes useless.

Chapter 2

Spatial discretization – the DGSE method

In this chapter we will explain in detail how to perform the spatial discretization with the Discontinuous Galerkin Spectral Element (DGSE) method and we will derive the algebraic formulation of the semi-discrete formulation (1.15) – (1.16).
As we have shortly explained in the introduction, the reasons for using non-conforming techniques, such as DGSE method, are many. Firstly, the flexibility in handling complex geometries, retaining the high order accuracy of spectral element methods. Secondly, since they are based on the weak formulation, they are able to handle both internal interface and external boundary conditions, allowing very accurate resolutions of seismic waves. Moreover, they guarantee geometrical and polynomial flexibility, that is an important task for simulating complex wave phenomena. Finally, they retain a high level parallel structure, thus they are well suited for parallel computations, which is mandatory for three dimensional problems.
We introduce the DGSE method in a two dimensional setting, in order to ease the presentation. The extension to three dimensional cases can be obtained similarly.

2.1 The DGSE approach

The DGSE approach we employ can be described as a three-levels process. At the first (macro) level, the elastic subdomain Ω^e is partitioned into K^e non-overlapping polygonal regions Ω_k^e, $k = 1, \ldots, K^e$, such that $\Omega^e = \cup_{k=1}^{K^e} \Omega_k^e$, with $\Omega_k^e \cap \Omega_l^e = \emptyset$ for any $k \neq l$. Moreover, we define the elastic skeleton as $\mathcal{S}^e = \cup_{k=1}^{K^e} \partial\Omega_k^e \setminus \partial\Omega^e = \cup_{k=1}^{K^e} \partial\Omega_k^e \setminus \left(\Gamma^e \cup \Gamma^i\right)$ (see Figure 2.1).

This macro decomposition is done for distinguish elastic materials with different properties. In other words, each Ω_k^e should represent a part of the domain Ω^e, such as a layer in the earth subsurface, through which seismic waves propagate. Clearly, in order to be more likely with the reality, the decomposition is not supposed to be geometrically conforming, i.e., for two neighbouring subdomains Ω_k^e and Ω_l^e, the interface $\partial\Omega_k^e \cap \partial\Omega_l^e$ may not be a complete side of Ω_k^e or Ω_l^e (see Figure 2.1).

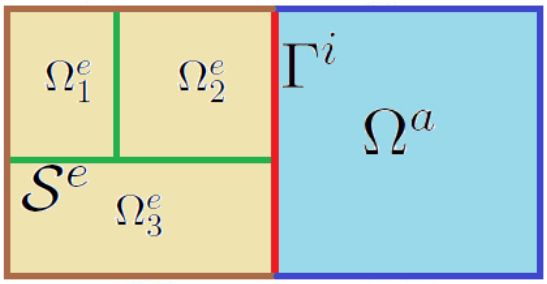

Figure 2.1: Example of a two-dimensional subdomain partition of $\Omega^e = \Omega_1^e \cup \Omega_2^e \cup \Omega_3^e$. Internal boundaries are the elasto-acoustic interface Γ^i and the elastic skeleton $\mathcal{S}^e$.

At the second (meso) level, we introduce on each Ω_k^e a conforming partition $\mathcal{T}_k^e$, made by quadrilateral elements $\Omega_{k,j}^e$ (or hexahedrals in three dimensions). We call R_k^e the number of elements in the mesh $\mathcal{T}_k^e$ and thus we get $\Omega_k^e = \cup_{j=1}^{R_k^e} \Omega_{k,j}^e$ (see Figure 2.2). The typical mesh size is $h_k^e = \max_{j=1,\dots,R_k^e} \left\{h_{k,j}^e\right\}$, where $h_{k,j}^e = \mathrm{diam}\big(\Omega_{k,j}^e\big)$. Each $\Omega_{k,j}^e$ is obtained by mapping the reference bi-dimensional element $\widehat{\Omega} = [-1,1]^2$ with a suitable bilinear map $\mathbf{F}_{k,j}^e : \widehat{\Omega} \to \Omega_{k,j}^e$ with positive Jacobian $J_{k,j}^e$.
The partition $\mathcal{T}_k^e$ is geometrically conforming in each Ω_k^e, thus the intersection of two elements $\Omega_{k,j}^e$ and $\Omega_{k,i}^e$, for any $i \neq j$, is either empty, or a vertex, or an edge (or also a face, in three dimensions) of both $\Omega_{k,j}^e$ and $\Omega_{k,i}^e$ (see Figure 2.2).
Finally, at the third (micro) level, the so-called *Gauss-Legendre-Lobatto* (GLL) points are placed in each element $\Omega_{k,j}^e$. We thus choose a spectral degree N_k^e for each macro-region Ω_k^e and we get $(N_k^e+1)^2$ GLL interpolation points on each element $\Omega_{k,j}^e$ of the mesh $\mathcal{T}_k^e$. On the reference element $\widehat{\Omega}$ these points are the tensor product of GLL points defined in the interval $[-1,1]$ as the zeros of $(1-x^2)L'_{N_k^e}(x)$, where $L'_{N_k^e}$ is the derivative of the Legendre polynomial $L_{N_k^e}$, see e.g., [9, 10] for details. Then, they are mapped on each physical element through the map $\mathbf{F}_{k,j}^e$, see Figure 2.2.

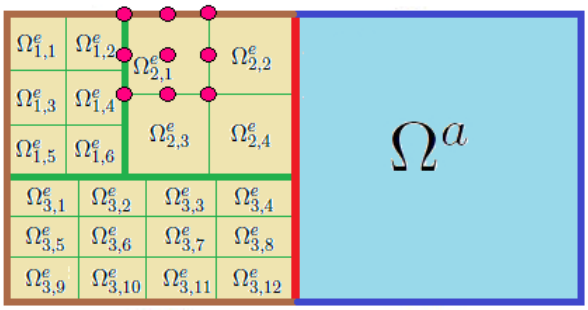

Figure 2.2: Example of two-dimensional meshes $\mathcal{T}_1^e$, $\mathcal{T}_2^e$ and $\mathcal{T}_3^e$. They have different mesh-sizes and are conforming in each macro-region Ω_1^e, Ω_2^e and Ω_3^e, respectively. Here $N_2^e = 2$ and nine GLL points are placed as example in the element $\Omega_{2,1}^e$.

Let now $\mathbb{Q}_{N_k^e}(\widehat{\Omega})$ be the space of algebraic polynomials defined on $\widehat{\Omega}$ with degree less than or equal to N_k^e in each coordinate direction. We define

$$\mathbb{Q}_{N_k^e}(\Omega_{k,j}^e) = \left\{ w : (w \circ \mathbf{F}_{k,j}^e) \in \mathbb{Q}_{N_k^e}(\widehat{\Omega}) \right\}.$$

Then, we introduce the following finite dimensional space

$$X_N(\Omega_k^e) = \left\{ w_N \in \mathbb{C}^0(\bar{\Omega}_k^e) : w_{N|\Omega_{k,j}^e} \in \mathbb{Q}_{N_k^e}(\Omega_{k,j}^e) \ \forall j = 1, \ldots, R_k^e \right\}.$$

Finally, we get

$$\mathbf{W_N} = \left\{ \mathbf{w_N} \in \boldsymbol{L^2}(\Omega^e) : \mathbf{w_N}_{|\Omega_k^e} \in \boldsymbol{X_N}(\Omega_k^e) \ \forall k = 1, \ldots, K^e \ , \ \mathbf{w_N} = \mathbf{0} \text{ on } \Gamma_D^e \right\}.$$

The subscript $"N"$ means that $\mathbf{W_N}$ is a finite dimensional space of piecewise polynomial functions. It is related to the K^e-uplets of discretization parameters $(h_1^e, \ldots, h_{K^e}^e)$ and $(N_1^e, \ldots, N_{K^e}^e)$. It is important to see that two different macro-regions Ω_k^e and Ω_l^e can be meshed with two partitions $\mathcal{T}_k^e$ and $\mathcal{T}_l^e$ with different sizes h_k^e and h_l^e, in order to take into account sharp variations in the physical parameters of the two media. Analogously, also the spectral degrees N_k^e and N_l^e may be not the same: this should assure good accuracy without refining too much the grids.
The variational formulation (1.15) of the elastodynamic equation of motion (1.1) is thus reformulated in the finite dimensional space $\mathbf{W_N}$ and then solved in each Ω_k^e, together with suitable interface conditions on the skeleton $\mathcal{S}^e$.
We thus have that

$$\int_{\Omega_k^e} f d\Omega = \sum_{j=1}^{R_k^e} \int_{\Omega_{k,j}^e} f d\Omega = \sum_{j=1}^{R_k^e} \int_{\widehat{\Omega}} (f \circ \mathbf{F}_{k,j}^e) J_{k,j}^e d\Omega,$$

where the integrals are evaluated using the GLL integration rule. Thus, they are replaced by finite sums, which use GLL interpolation points as quadrature points, in order to get

$$\int_{\widehat{\Omega}} (f \circ \mathbf{F}^e_{k,j}) J^e_{k,j} d\Omega \approx \sum_{i=1}^{(N^e_k+1)^2} (f \circ \mathbf{F}^e_{k,j})(\mathbf{p}^e_i) J^e_{k,j}(\mathbf{p}^e_i) \alpha^e_i,$$

where $\left\{\mathbf{p}^e_i\right\}_{i=1}^{(N^e_k+1)^2}$, are the elastic GLL points defined on the reference element $\widehat{\Omega}$, as explained above, and α^e_i are the respective GLL quadrature weights. Note that the GLL quadrature formula is exact for $(f \circ \mathbf{F}^e_{k,j}) J^e_{k,j} \in \mathbb{Q}_{2N^e_k-1}(\widehat{\Omega})$. We call $\mathbf{x}^e_i = \mathbf{F}^e_{k,j}(\mathbf{p}^e_i)$ and we define the elastic spectral shape functions $\left\{\Psi^e_i\right\}_{i=1}^{(N^e_k+1)^2} \subset \mathbf{W_N}$ on each $\Omega^e_{k,j}$ as $\Psi^e_i(\mathbf{x}^e_h) = \delta_{ih}$, where δ_{ih} is the Kronecker symbol. It is straightforward to see that the spectral shape functions are continuous functions on each macro-region Ω^e_k and their restriction to $\Omega^e_{k,j}$ either coincides with a Lagrange polynomial or vanishes. Moreover, the support of any shape function is limited to the neighbouring elements if the relative spectral node lies on the interface between two or more elements, while it is confined to only one element for internal nodes.
As mentioned above, solving (1.1) in each macro-region Ω^e_k, we have to take into account some transmission conditions across the skeleton $\mathcal{S}^e$. They should ensure that the local solution is the restriction to Ω^e_k of the global solution. This turns out in an additional term to the variational formulation (1.15). This term is a bilinear form $\mathcal{B}^e(\cdot,\cdot)$ which is defined as follows

$$\mathcal{B}^e_{\partial\Omega^e_k \setminus \partial\Omega^e}(\mathbf{u},\mathbf{w}) = -\big(\sigma(\mathbf{u})\mathbf{n}, \mathbf{w}\big)_{\partial\Omega^e_k \setminus \partial\Omega^e} \tag{2.1}$$

In order to get a computable expression of $\mathcal{B}^e(\cdot,\cdot)$, as we did for elasto-acoustic coupling conditions in Chapter 1, we still impose the continuity of the normal component of the displacement and stresses across the skeleton $\mathcal{S}^e$. We introduce the symbol $[\![\cdot]\!]$, that denotes the jump, defined in a suitable way that will be made clear later on, of a quantity through a given interface. Thus, the two continuity conditions read

$$[\![\mathbf{u}]\!] = 0 \qquad \text{and} \qquad [\![\sigma]\!] = 0 \tag{2.2}$$

across the skeleton $\mathcal{S}^e$.
We now rewrite the skeleton as the union of some elementary components. Thus, let $\Omega^e_{k,j} \in \Omega^e_k$ and $\Omega^e_{l,i} \in \Omega^e_l$ be two neighbouring elements belonging to different macro-regions. We set $\gamma^e_m = \partial\Omega^e_{k,j} \cap \partial\Omega^e_{l,i}$, where $m = m(i,j,k,l)$. Note that $\gamma^e_m \cap \gamma^e_p = 0$ for any $m \neq p$. The skeleton $\mathcal{S}^e$ may now be written as $\mathcal{S}^e = \cup_{m=1}^{M} \gamma^e_m$, for some positive integer M, see Figure 2.3.

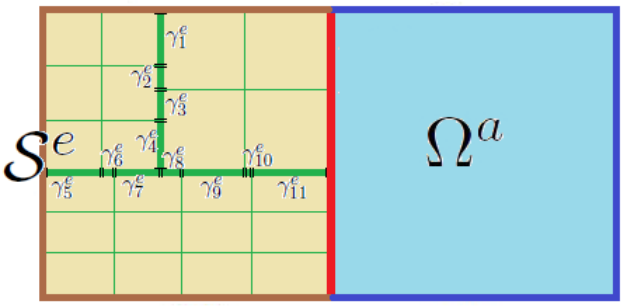

Figure 2.3: Example of two-dimensional elastic skeleton $\mathcal{S}^e$ split into $M = 11$ edges, as $\mathcal{S}^e = \cup_{m=1}^{11} \gamma_m^e$.

For any pair of adjacent elements Ω_+^e and Ω_-^e sharing a non-trivial edge γ^e, we denote by $\mathbf{u}_+$, σ_+ (resp. $\mathbf{u}_-$, σ_-) the restriction to Ω_+^e (resp. Ω_-^e) of the displacement $\mathbf{u}$ and the Cauchy stress tensor σ. We also denote by $\mathbf{n}_+$ (resp. $\mathbf{n}_-$) the outward pointing unit normal vector to Ω_+^e (resp. Ω_-^e). We now define the average and jump operators across γ^e for $\mathbf{u}$ and σ as follows

$$\{\mathbf{u}\} = \frac{1}{2}(\mathbf{u}_+ + \mathbf{u}_-), \qquad [\![\mathbf{u}]\!] = \mathbf{u}_+ \otimes \mathbf{n}_+ + \mathbf{u}_- \otimes \mathbf{n}_-, \tag{2.3}$$

and

$$\{\sigma\} = \frac{1}{2}(\sigma_+ + \sigma_-), \qquad [\![\sigma]\!] = \sigma_+ \mathbf{n}_+ + \sigma_- \mathbf{n}_-, \tag{2.4}$$

where $\mathbf{a} \otimes \mathbf{b} \in \mathcal{R}^{2\times 2}$ is the tensor with entries $(\mathbf{a} \otimes \mathbf{b})_{ij} = a_i b_j$, for any $i, j = 1, 2$.
Using definitions (2.3) and (2.4), the sum above the whole skeleton $\mathcal{S}^e$ of the bilinear terms (2.1) may be written in the following form

$$\sum_{k=1}^{K^e} \left(\sigma(\mathbf{u})\mathbf{n}, \mathbf{w}\right)_{\partial\Omega_k^e \setminus \partial\Omega^e} = \sum_{m=1}^{M} \left(\{\sigma(\mathbf{u})\}, [\![\mathbf{w}]\!]\right)_{\gamma_m^e} + \sum_{m=1}^{M} \left([\![\sigma(\mathbf{u})]\!], \{\mathbf{w}\}\right)_{\gamma_m^e},$$

and, since the second transmission condition (2.2) holds, we get

$$\sum_{k=1}^{K^e} \left(\sigma(\mathbf{u})\mathbf{n}, \mathbf{w}\right)_{\partial\Omega_k^e \setminus \partial\Omega^e} = \sum_{m=1}^{M} \left(\{\sigma(\mathbf{u})\}, [\![\mathbf{w}]\!]\right)_{\gamma_m^e}.$$

Since also the first transmission condition (2.1) holds, we can further add other terms in order to penalize and control the jump of the numerical solution (see [42, 43]). These terms read

$$\theta \sum_{m=1}^{M} \left([\![\mathbf{u}]\!], \{\sigma(\mathbf{w})\}\right)_{\gamma_m^e} + \sum_{m=1}^{M} \eta_{\gamma_m^e} \left([\![\mathbf{u}]\!], [\![\mathbf{w}]\!]\right)_{\gamma_m^e},$$

where $\theta = \{-1, 0, 1\}$ and $\eta_{\gamma_m^e}$ are positive constants depending on the discretization parameters $(h_1^e, \dots, h_{K^e}^e)$ and $(N_1^e, \dots, N_{K^e}^e)$ and on the Lamé coefficients λ and μ.
Thus, we can rewrite the term (2.1) as follows

$$\mathcal{B}^e_{\gamma_m^e}(\mathbf{u}, \mathbf{w}) = -\big(\{\sigma(\mathbf{u})\}, [\![\mathbf{w}]\!]\big)_{\gamma_m^e} + \theta\big([\![\mathbf{u}]\!], \{\sigma(\mathbf{w})\}\big)_{\gamma_m^e} + \eta_{\gamma_m^e}\big([\![\mathbf{u}]\!], [\![\mathbf{w}]\!]\big)_{\gamma_m^e}. \tag{2.5}$$

Corresponding to different choices of θ we obtain different DG schemes, namely: $\theta = -1$ leads to the symmetric interior penalty method (SIPG), $\theta = 1$ leads to the non-symmetric interior penalty method (NIPG), while $\theta = 0$ corresponds to the incomplete interior penalty method (IIPG), see [3, 42, 43, 45] for more details.

Differently from what we did in Ω^e, in the acoustic subdomain Ω^a the DGSE approach is a two-levels process. In fact, since in this thesis we consider only single-phase fluids, there is no reason for macro-partitioning Ω^a into different regions that should be related to fluids with different mechanical properties. In this case we thus have only the meso and the micro levels previously described for the elastic part.
We proceed at the same way: we first introduce a conforming mesh $\mathcal{T}^a$ of the whole acoustic subdomain Ω^a, made by quadrilateral elements Ω_j^a (or hexahedrals in three dimensions). We call R^a the number of elements in $\mathcal{T}^a$ and thus we get $\Omega^a = \cup_{j=1}^{R^a} \Omega_j^a$ (see Figure 2.4). The typical mesh size is $h^a = \max_{j=1,\dots,R^a}\{h_j^a\}$, where $h_j^a = \mathrm{diam}(\Omega_j^a)$. Each of the Ω_j^a is obtained by mapping the reference bi-dimensional element $\widehat{\Omega} = [-1, 1]^2$ with a suitable bilinear map $\mathbf{F}_j^a : \widehat{\Omega} \to \Omega_j^a$ with positive Jacobian J_j^a.
The partition $\mathcal{T}^a$ is geometrically conforming in Ω^a, thus the intersection of two elements Ω_j^a and Ω_i^a, for any $i \neq j$, is either empty, or a vertex, or an edge (or also a face, in three dimensional applications) of both Ω_j^a and Ω_i^a (see Figure 2.4).
Then, we have to set the GLL points in each element of the mesh. We choose a spectral degree N^a and we get $(N^a + 1)^2$ GLL interpolation points on each $\Omega_j^a \in \mathcal{T}^a$. These points are obtained in the same way described for the solid part: they are defined on the reference element $\widehat{\Omega}$ as the tensor product of GLL points defined in the interval $[-1, 1]$, see [9, 10], then they are mapped on each physical element through the map $\mathbf{F}_j^a$ (see Figure 2.4).
Remembering the definition of $\mathbb{Q}_{N^a}(\widehat{\Omega})$, given for the solid part, we now introduce the following functional spaces

$$\mathbb{Q}_{N^a}(\Omega_j^a) = \big\{v : (v \circ \mathbf{F}_j^a) \in \mathbb{Q}_{N^a}(\widehat{\Omega})\big\},$$

and

$$V_N(\Omega^a) = \big\{v_N \in \mathbb{C}^0(\bar{\Omega}^a) : v_{N|\Omega_j^a} \in \mathbb{Q}_{N^a}(\Omega_j^a)\ \forall j = 1, \dots, R^a\ ,\ v_N = 0 \text{ on } \Gamma_D^a\big\}.$$

The subscript $"N"$ means that V_N is a finite dimensional subspace of the infinite dimensional space V, introduced in Chapter 1. It is related to the discretization parameters h^a and N^a.

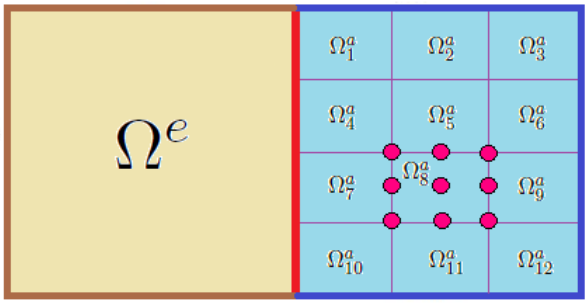

Figure 2.4: Example of a two-dimensional acoustic mesh $\mathcal{T}^a$. It is geometrically conforming in the whole subdomain Ω^a. $N^a = 2$ in this case and nine GLL points are placed as example in the element Ω_8^a.

We thus have that

$$\int_{\Omega^a} f d\Omega = \sum_{j=1}^{R^a} \int_{\Omega_j^a} f d\Omega = \sum_{j=1}^{R^a} \int_{\widehat{\Omega}} (f \circ \mathbf{F}_j^a) J_j^a d\Omega,$$

where the integrals are still evaluated using the same GLL integration rule introduced for the elastic part. Thus, we get

$$\int_{\widehat{\Omega}} (f \circ \mathbf{F}_j^a) J_j^a d\Omega \approx \sum_{i=1}^{(N^a+1)^2} (f \circ \mathbf{F}_j^a)(\mathbf{p}_i^a) J_j^a(\mathbf{p}_i^a) \alpha_i^a,$$

where $\left\{\mathbf{p}_i^a\right\}_{i=1}^{(N^a+1)^2}$, are the acoustic GLL points defined on the reference element $\widehat{\Omega}$, as explained above, and α_i^a are the respective GLL quadrature weights. Note that the GLL quadrature formula is exact for $(f \circ \mathbf{F}_j^a) J_j^a \in \mathbb{Q}_{2N^a-1}(\widehat{\Omega})$. We call $\mathbf{x}_i^a = \mathbf{F}_j^a(\mathbf{p}_i^a)$ and we define the acoustic spectral shape functions $\left\{\Psi_i^a\right\}_{i=1}^{(N^a+1)^2} \subset V_N$ on each Ω_j^a as $\Psi_i^a(\mathbf{x}_h^a) = \delta_{ih}$, where δ_{ih} is the Kronecker symbol. It is straightforward to see that the spectral shape functions are continuous functions on the whole acoustic subdomain Ω^a and their restriction to each Ω_j^a either coincides with a Lagrange polynomial or vanishes. Moreover, the support of any shape function is limited to the neighbouring elements if the relative spectral node lies on the interface between two or more elements, while it is confined to only one element for internal nodes.

Finally, we have to treat the elasto-acoustic interface Γ^i. Since elastic and acoustic meshes are, in general, non-matching at the two sides of this interface, it seems reasonable to proceed with a decomposition of Γ^i at the same way that we did for the elastic skeleton $\mathcal{S}^e$. Thus, let $\Omega^e_{k,j} \in \Omega^e_k$ and Ω^a_i be two neighbouring elements sharing a part of Γ^i. We set $\gamma^{ea}_n = \partial\Omega^e_{k,j} \cap \partial\Omega^a_i$, where $n = n(i,j,k)$. Note that $\gamma^{ea}_n \cap \gamma^{ea}_q = 0$ for any $n \neq q$. The elasto-acoustic interface Γ^i may now be written as $\Gamma^i = \cup_{n=1}^N \gamma^{ea}_n$, for some positive integer N.
Thus, the bilinear coupling terms $\mathcal{C}^e(\cdot,\cdot)$ and $\mathcal{C}^a(\cdot,\cdot)$ which appear in (1.15) and (1.16) may now be written as

$$\mathcal{C}^{e(a)}(\cdot,\cdot) = \sum_{n=1}^{N} \mathcal{C}^{e(a)}_{\gamma^{ea}_n}(\cdot,\cdot),$$

where

$$\mathcal{C}^e_{\gamma^{ea}_n}(p,\mathbf{w}) = -\big(p\mathbf{n}^a, \mathbf{w}\big)_{\gamma^{ea}_n} = \big(p\mathbf{n}^e, \mathbf{w}\big)_{\gamma^{ea}_n}, \tag{2.6}$$

and

$$\mathcal{C}^a_{\gamma^{ea}_n}(\mathbf{u},v) = -\big(\partial_{tt}\mathbf{u}\cdot\mathbf{n}^e, v\big)_{\gamma^{ea}_n} = \big(\partial_{tt}\mathbf{u}\cdot\mathbf{n}^a, v\big)_{\gamma^{ea}_n}. \tag{2.7}$$

We recall that $\mathbf{n}^e$ and $\mathbf{n}^a$ are the outward pointing unit normal vector on Γ^i with respect to the solid and the acoustic subdomain, respectively.
We would like to remark that the elasto-acoustic coupling have been already treated in previous studies only with conforming grids. Non-matching coupling is, in this sense, "something new" on which we have insisted. It constitutes the main difference of this thesis with respect to existing literature.

2.2 The semi-discrete formulation

Starting from the variational formulation (1.17) and applying the space discretization with the DGSE method introduced in the previous section, we rewrite the problem in $(\mathbf{W_N} \times V_N)$. Thus, equation (1.15) become

$$\sum_{k=1}^{K^e} \big(\rho^e \partial_{tt}\mathbf{u_N}, \mathbf{w_N}\big)_{\Omega^e_k} + \sum_{k=1}^{K^e} \mathcal{A}^e_{\Omega^e_k}(\mathbf{u_N}, \mathbf{w_N}) + \sum_{m=1}^{M} \mathcal{B}^e_{\gamma^e_m}(\mathbf{u_N}, \mathbf{w_N}) + \sum_{n=1}^{N} \mathcal{C}^e_{\gamma^{ea}_n}(p_N, \mathbf{w_N}) = \sum_{k=1}^{K^e} \mathcal{L}^e_{\Omega^e_k}(\mathbf{w_N}), \tag{2.8}$$

where the terms $\mathcal{A}^e_{\Omega^e_k}(\cdot,\cdot)$ and $\mathcal{L}^e_{\Omega^e_k}(\cdot)$ are defined as follows

$$\mathcal{A}^e_{\Omega^e_k}(\mathbf{u},\mathbf{w}) = \big(\sigma(\mathbf{u}), \epsilon(\mathbf{w})\big)_{\Omega^e_k},$$
$$\mathcal{L}^e_{\Omega^e_k}(\mathbf{w}) = \big(\mathbf{f}^e, \mathbf{w}\big)_{\Omega^e_k} + \big(\mathbf{t}^e, \mathbf{w}\big)_{\Gamma^e_N \cap \partial\Omega^e_k} + \big(\tilde{\mathbf{t}}^e, \mathbf{w}\big)_{\Gamma^e_{NR} \cap \partial\Omega^e_k}.$$

The terms $\mathcal{B}^e_{\gamma^e_m}(\cdot,\cdot)$ and $\mathcal{C}^e_{\gamma^{ea}_n}(\cdot,\cdot)$ are the ones introduced in (2.5) and (2.6), respectively.
Analogously, equation (1.16) become

$$\Big(\frac{1}{\rho^a c^2}\partial_{tt}p_N, v_N\Big)_{\Omega^a} + \mathcal{A}^a(p_N, v_N) + \sum_{n=1}^{N}\mathcal{C}^a_{\gamma^{ea}_n}(\mathbf{u_N}, v_N) = \mathcal{L}^a(v_N), \qquad (2.9)$$

where the term $\mathcal{C}^a_{\gamma^{ea}_n}(\cdot,\cdot)$ is defined in (2.7).
Thus, the semi-discrete formulation of the coupled elasto-acoustic wave propagation problem is:

$$\begin{aligned}
&\text{find } (\mathbf{u_N}, p_N) \text{ such that } \forall t\in[0,T]\ (\mathbf{u_N}(t), p_N(t)) \in (\mathbf{W_N}\times V_N) \text{ and}\\
&\sum_{k=1}^{K^e}\big(\rho^e\partial_{tt}\mathbf{u_N}, \mathbf{w_N}\big)_{\Omega^e_k} + \sum_{k=1}^{K^e}\mathcal{A}^e_{\Omega^e_k}(\mathbf{u_N}, \mathbf{w_N}) + \sum_{m=1}^{M}\mathcal{B}^e_{\gamma^e_m}(\mathbf{u_N}, \mathbf{w_N})\\
&\qquad + \sum_{n=1}^{N}\mathcal{C}^e_{\gamma^{ea}_n}(p_N, \mathbf{w_N}) = \sum_{k=1}^{K^e}\mathcal{L}^e_{\Omega^e_k}(\mathbf{w_N}), \quad \forall \mathbf{w_N}\in\mathbf{W_N},\\
&\Big(\frac{1}{\rho^a c^2}\partial_{tt}p_N, v_N\Big)_{\Omega^a} + \mathcal{A}^a(p_N, v_N) + \sum_{n=1}^{N}\mathcal{C}^a_{\gamma^{ea}_n}(\mathbf{u_N}, v_N) = \mathcal{L}^a(v_N), \quad \forall v_N\in V_N.
\end{aligned} \qquad (2.10)$$

As we did for the weak formulation in Chapter 1, we are now interested in draw suitable stability estimates for the semi-discrete problem (2.10). Before do that, we should prove its well position and thus the existence and uniqueness of its solution. However, despite [7, 26] treat this argument in the continuous case (see Section 1.6), the analysis of existence and uniqueness for the DGSE semi-discrete formulation is actually under investigation. Thus, we present the following results aware of this fact.
For simplicity, we still consider a two-dimensional problem with zero-order absorbing boundary conditions on $\Gamma_{NR} = \Gamma^e_{NR}\cup\Gamma^a_{NR}$ and homogeneous Neumann boundary conditions on $\Gamma_N = \Gamma^e_N\cup\Gamma^a_N$. The acoustic part is still expressed in terms of the velocity potential ψ_N instead of the pressure field p_N, i.e., $p_N = \rho^a\partial_t\psi_N$.
The main difference from the continuous case is that now, in the elastic part, we have to take into account the macro-partition introduced above, which leads out into the additional interface term $\mathcal{B}^e(\cdot,\cdot)$. We show the following results in the case of SIPG method, that is, substituting $\theta = -1$ in (2.5), i.e.,

$$\mathcal{B}^e(\mathbf{u},\mathbf{w})_{\gamma^e_m} = -\big(\{\sigma(\mathbf{u})\}, [\![\mathbf{w}]\!]\big)_{\gamma^e_m} - \big([\![\mathbf{u}]\!], \{\sigma(\mathbf{w})\}\big)_{\gamma^e_m} + \eta_{\gamma^e_m}\big([\![\mathbf{u}]\!], [\![\mathbf{w}]\!]\big)_{\gamma^e_m}.$$

Under the same hypothesis of those introduced in Section 1.6, we introduce the following energy norms for $\mathbf{u_N}(t)$ and $\psi_N(t)$,

$$\|\mathbf{u_N}(t)\|^2_{E^e_k} = \|\sqrt{\rho^e}\partial_t\mathbf{u_N}(t)\|^2_{\mathbf{L}^2(\Omega^e_k)} + \left\|C^{\frac{1}{2}}[\epsilon(\mathbf{u_N}(t))]\right\|^2_{[\mathbf{L}^2(\Omega^e_k)]^2}$$
$$+ \sum_{m=1}^{M} \left\|\sqrt{\eta_{\gamma^e_m}}[\![\mathbf{u_N}(t)]\!]\right\|^2_{\mathbf{L}^2(\gamma^e_m\cap\partial\Omega^e_k)} \qquad \forall k = 1,\dots,K^e, \quad \forall t\in[0,T],$$

and

$$\|\psi_N(t)\|^2_{E^a} = \left\|\frac{\sqrt{\rho^a}}{c}\partial_t\psi_N(t)\right\|^2_{L^2(\Omega^a)} + \|\sqrt{\rho^a}\nabla\psi_N(t)\|^2_{\mathbf{L}^2(\Omega^a)} \qquad \forall t\in[0,T],$$

respectively.
We thus rewrite the equations (2.8) – (2.9) as the semi-discrete formulation of (1.18), obtaining

$$\sum_{k=1}^{K^e}\left(\rho^e\partial_{tt}\mathbf{u_N},\mathbf{w_N}\right)_{\Omega^e_k} + \sum_{k=1}^{K^e}\left(\sigma(\mathbf{u_N}),\epsilon(\mathbf{w_N})\right)_{\Omega^e_k} + \sum_{k=1}^{K^e}\left(E\partial_t\mathbf{u_N},\mathbf{w_N}\right)_{\Gamma^e_{NR}\cap\partial\Omega^e_k}$$
$$-\sum_{m=1}^{M}\left(\{\sigma(\mathbf{u_N})\},[\![\mathbf{w_N}]\!]\right)_{\gamma^e_m} - \sum_{m=1}^{M}\left([\![\mathbf{u_N}]\!],\{\sigma(\mathbf{w_N})\}\right)_{\gamma^e_m} + \sum_{m=1}^{M}\eta_{\gamma^e_m}\left([\![\mathbf{u_N}]\!],[\![\mathbf{w_N}]\!]\right)_{\gamma^e_m}$$
$$-\sum_{n=1}^{N}\left(\rho^a\partial_t\psi_N\mathbf{n}^a,\mathbf{w_N}\right)_{\gamma^{ea}_n} = \sum_{k=1}^{K^e}\left(\mathbf{f}^e,\mathbf{w_N}\right)_{\Omega^e_k} \qquad \forall\mathbf{w_N}\in\mathbf{W_N}, \quad (2.11)$$

and

$$\left(\frac{\rho^a}{c^2}\partial_{tt}\psi_N, v_N\right)_{\Omega^a} + \left(\rho^a\nabla\psi_N,\nabla v_N\right)_{\Omega^a} + \left(\frac{\rho^a}{c}\partial_t\psi_N, v_N\right)_{\Gamma^a_{NR}}$$
$$-\sum_{n=1}^{N}\left(\rho^a\partial_t\mathbf{u_N}\cdot\mathbf{n}^e, v_N\right)_{\gamma^{ea}_n} = \left(\rho^a f^a_\psi, v_N\right)_{\Omega^a} \qquad \forall v_N\in V_N. \quad (2.12)$$

Now we choose the test functions $\mathbf{w_N} = \partial_t\mathbf{u_N}(t)\in\mathbf{W_N}$, $v_N = \partial_t\psi_N(t)\in V_N$. Using the energy norms previously defined, equations (2.11) – (2.12) become

$$\frac{1}{2}\frac{d}{dt}\sum_{k=1}^{K^e}\|\mathbf{u_N}(t)\|^2_{E^e_k} - \frac{d}{dt}\sum_{m=1}^{M}\left(\{\sigma(\mathbf{u_N}(t))\},[\![\mathbf{u_N}(t)]\!]\right)_{\gamma^e_m}$$
$$+\sum_{k=1}^{K^e}\left(E\partial_t\mathbf{u_N}(t),\partial_t\mathbf{u_N}(t)\right)_{\Gamma^e_{NR}\cap\partial\Omega^e_k} - \sum_{n=1}^{N}\left(\rho^a\partial_t\psi_N(t)\mathbf{n}^a,\partial_t\mathbf{u_N}(t)\right)_{\gamma^{ea}_n}$$
$$= \sum_{k=1}^{K^e}\left(\mathbf{f}^e(t),\partial_t\mathbf{u_N}(t)\right)_{\Omega^e_k} \qquad \forall t\in[0,T], \quad (2.13)$$

and

$$\frac{1}{2}\frac{d}{dt}\|\psi_N(t)\|^2_{E^a}+\Big(\frac{\rho^a}{c}\partial_t\psi_N(t),\partial_t\psi_N(t)\Big)_{\Gamma^a_{NR}}-\sum_{n=1}^{N}\big(\rho^a\partial_t\mathbf{u_N}(t)\cdot\mathbf{n}^e,\partial_t\psi_N(t)\big)_{\gamma^{ea}_n}$$
$$=\big(\rho^a f^a_\psi(t),\partial_t\psi_N(t)\big)_{\Omega^a}\qquad\forall t\in[0,T].\quad(2.14)$$

Since the volume forces are supposed to be such that $\mathbf{f}^e(t)\in\mathbf{L}^2(\Omega^e)$ and $f^a_\psi(t)\in L^2(\Omega^a)$, inequalities (1.24) still hold. We thus sum equations (2.13) and (2.14) and get $\forall t\in[0,T]$ the following expression

$$\frac{d}{dt}\sum_{k=1}^{K^e}\|\mathbf{u_N}(t)\|^2_{E^e_k}-2\frac{d}{dt}\sum_{m=1}^{M}\big(\{\sigma(\mathbf{u_N}(t))\},[\![\mathbf{u_N}(t)]\!]\big)_{\gamma^e_m}+\frac{d}{dt}\|\psi_N(t)\|^2_{E^a}\leq$$
$$\frac{1}{\rho^e_m}\sum_{k=1}^{K^e}\|\mathbf{f}^e(t)\|^2_{\mathbf{L}^2(\Omega^e_k)}+\sum_{k=1}^{K^e}\|\mathbf{u_N}(t)\|^2_{E^e_k}+\rho^a_M c^2_M\|f^a_\psi(t)\|^2_{L^2(\Omega^a)}+\|\psi(t)\|^2_{E^a}.\quad(2.15)$$

We now integrate in time the inequality (2.15) and we get $\forall t\in[0,T]$,

$$\sum_{k=1}^{K^e}\|\mathbf{u_N}(t)\|^2_{E^e_k}-2\sum_{m=1}^{M}\big(\{\sigma(\mathbf{u_N}(t))\},[\![\mathbf{u_N}(t)]\!]\big)_{\gamma^e_m}+\|\psi_N(t)\|^2_{E^a}\leq$$
$$\sum_{k=1}^{K^e}\|\mathbf{u_N}(0)\|^2_{E^e_k}-2\sum_{m=1}^{M}\big(\{\sigma(\mathbf{u_N}(0))\},[\![\mathbf{u_N}(0)]\!]\big)_{\gamma^e_m}+\|\psi_N(0)\|^2_{E^a}$$
$$+\int_0^t\Big(\frac{1}{\rho^e_m}\sum_{k=1}^{K^e}\|\mathbf{f}^e(\tau)\|^2_{\mathbf{L}^2(\Omega^e_k)}+\rho^a_M c^2_M\|f^a_\psi(\tau)\|^2_{L^2(\Omega^a)}$$
$$+\sum_{k=1}^{K^e}\|\mathbf{u_N}(\tau)\|^2_{E^e_k}+\|\psi(\tau)\|^2_{E^a})\Big)d\tau.\quad(2.16)$$

It can be proven that the following inequalities holds (see [2]),

$$\sum_{k=1}^{K^e}\|\mathbf{u_N}(t)\|^2_{E^e_k}-2\sum_{m=1}^{M}\big(\{\sigma(\mathbf{u_N}(t))\},[\![\mathbf{u_N}(t)]\!]\big)_{\gamma^e_m}\geq\sum_{k=1}^{K^e}\|\mathbf{u_N}(t)\|^2_{E^e_k},$$
$$\forall t\in(0,T],\text{while, for } t=0 \text{ we have,}\quad(2.17)$$
$$\sum_{k=1}^{K^e}\|\mathbf{u_N}(0)\|^2_{E^e_k}-2\sum_{m=1}^{M}\big(\{\sigma(\mathbf{u_N}(0))\},[\![\mathbf{u_N}(0)]\!]\big)_{\gamma^e_m}\leq\sum_{k=1}^{K^e}\|\mathbf{u_N}(0)\|^2_{E^e_k}.$$

Using (2.17) in (2.16) and applying *Gronwall's lemma* (see [39, p. 28]), we get the following stability estimate of the semi-discrete formulation (2.10)

$$\sum_{k=1}^{K^e} \|\mathbf{u_N}(t)\|^2_{E^e_k} + \|\psi_N(t)\|^2_{E^a} \leq e^t \Bigg[\sum_{k=1}^{K^e} \|\mathbf{u_N}(0)\|^2_{E^e_k} + \|\psi_N(0)\|^2_{E^a} + \int_0^t \Big(\frac{1}{\rho^e_m} \sum_{k=1}^{K^e} \|\mathbf{f}^e(\tau)\|^2_{\mathbf{L}^2(\Omega^e_k)} + \rho^a_M c^2_M \|f^a_\psi(\tau)\|^2_{L^2(\Omega^a)} \Big) d\tau \Bigg], \quad \forall t \in [0, T]. \tag{2.18}$$

The presence of the exponential term makes this estimate meaningful as long as the observed time interval is bounded by a finite $T > 0$. Otherwise, for $T \to \infty$ the stability estimate (2.18) becomes useless.

Chapter 3

Algebraic formulation

In this section we show how to get the algebraic formulation of the semi-discrete problem (2.10). For simplicity, we consider $\Omega \in \mathbb{R}^2$. The extension to three-dimensional problems follows similarly.
We denote by N^e_{tot} the total number of GLL nodes in the elastic subdomain Ω^e. N^e_{tot} is related to the number of macro-regions Ω^e_k, $k = 1, \dots, K^e$, to the number of elements of the partition $\mathcal{T}^e_k$ of each Ω^e_k and finally to the spectral degree N^e_k, which determines the number $(N^e_k + 1)^2$ of GLL nodes in each $\Omega^e_{k,j}$. It is straightforward to see that the dimension of each component of $\mathbf{w_N} \in \mathbf{W_N}$ is N^e_{tot}. Thus, the spectral shape functions $\left\{\Psi^e_i\right\}_{i=1}^{N^e_{tot}}$, introduced in the Section 2.1, form a basis for each component of the finite dimensional space $\mathbf{W_N}$. In other words, calling $\mathbf{\Psi}^{e,1}_i = (\Psi^e_i, 0)^T$ and $\mathbf{\Psi}^{e,2}_i = (0, \Psi^e_i)^T$, we have that $\left\{\mathbf{\Psi}^{e,1}_i, \mathbf{\Psi}^{e,2}_i\right\}_{i=1}^{N^e_{tot}}$ is a basis for $\mathbf{W_N}$.
Following the same argument, we call N^a_{tot} the total number of GLL nodes in the acoustic subdomain Ω^a. N^a_{tot} depends only on the number of elements of the mesh $\mathcal{T}^a$ and on the spectral degree N^a. Then, the spectral shape functions $\left\{\Psi^a_i\right\}_{i=1}^{N^a_{tot}}$ introduced in Section 2.1 form a basis for the finite dimensional space V_N.
Thus, we write the discretized elastic displacement $\mathbf{u_N} \in \mathbf{W_N}$ as linear combination of the relative basis functions, i.e.,

$$\mathbf{u_N}(\mathbf{x}, t) = \sum_{i=1}^{N^e_{tot}} \Psi^e_i \mathbf{U}_i(t) = \sum_{i=1}^{N^e_{tot}} \left[\mathbf{\Psi}^{e,1}_i U^1_i(t) + \mathbf{\Psi}^{e,2}_i U^2_i(t)\right],$$

where $\mathbf{U}_i(t) = \mathbf{u_N}(\mathbf{x}^e_i, t)$ for each $i = 1, \dots, N^e_{tot}$ and $t \in [0, T]$, being $\mathbf{x}^e_i$ a GLL elastic node.
Then, we define, for each $k = 1, \dots, K^e$, the integers a_k and b_k and we order the basis functions such that

$$\mathbf{u_N}_{|\Omega^e_k}(\mathbf{x}, t) = \sum_{i=a_k}^{b_k} \Psi^e_i \mathbf{U}_i(t) = \sum_{i=a_k}^{b_k} \left[\mathbf{\Psi}^{e,1}_i U^1_i(t) + \mathbf{\Psi}^{e,2}_i U^2_i(t)\right].$$

Clearly, we have $a_1 = 1$ and $b_{K^e} = N^e_{tot}$.
At the same way, the discretized acoustic pressure $p_N \in V_N$ may now be written as

$$p_N(\mathbf{x}, t) = \sum_{i=1}^{N^a_{tot}} \Psi^a_i P_i(t),$$

where $P_i(t) = p_N(\mathbf{x}^a_i, t)$ for each $i = 1, \ldots, N^a_{tot}$ and $t \in [0, T]$, being $\mathbf{x}^a_i$ a GLL acoustic node.
With the notation just introduced, we can write equation (2.8) for any test function $\mathbf{w_N} = \mathbf{\Psi}^{e,1}_i$ and $\mathbf{w_N} = \mathbf{\Psi}^{e,2}_i$, with $i = 1, \ldots, N^e_{tot}$, obtaining the following linear system

$$M^e \ddot{\mathbf{U}} + (E^e - S^e)\dot{\mathbf{U}} + (A^e + B^e + D^e - R^e)\mathbf{U} + C^e \mathbf{P} = \mathbf{F}^e. \tag{3.1}$$

We do the same for equation (2.9), choosing $v_N = \Psi^a_i$, $i = 1, \ldots, N^a_{tot}$, and obtaining

$$M^a \ddot{\mathbf{P}} - S^a \dot{\mathbf{P}} + A^e \mathbf{P} + C^a \ddot{\mathbf{U}} = \mathbf{F}^a. \tag{3.2}$$

The unknown vectors $\mathbf{U} \in \mathbb{R}^{2N^e_{tot}}$ and $\mathbf{P} \in \mathbb{R}^{N^a_{tot}}$ are defined, respectively, as

$$\mathbf{U} = (U^1_1, \ldots, U^1_{N^e_{tot}}, U^2_1, \ldots, U^2_{N^e_{tot}})^T, \qquad \mathbf{P} = (P_1, \ldots, P_{N^a_{tot}})^T.$$

The dots over them in equations (3.1) and (3.2) stand for the times derivatives. Note that, thanks to the previous ordering of elastic basis functions, we have

$$\mathbf{U} = (U^1_{a_1}, \ldots, U^1_{b_1}, U^1_{a_2}, \ldots, U^1_{b_{K^e}}, U^2_{a_1}, \ldots, U^2_{b_1}, U^2_{a_2}, \ldots, U^2_{b_{K^e}})^T.$$

In the following subsections we detail the structure of the matrices appearing in (3.1) – (3.2).

Mass matrices

The elastic mass matrix $M^e \in \mathbb{R}^{2N^e_{tot} \times 2N^e_{tot}}$ is related to the first term of equation (2.8) and it has a block diagonal structure

$$M^e = \begin{bmatrix} M^{e,1} & 0 \\ 0 & M^{e,2} \end{bmatrix},$$

where $M^{e,1}$ and $M^{e,2}$ have in turn a diagonal structure. Thus we have

$$M^{e,l} = \begin{bmatrix} M^{e,l}_1 & & \\ & \ddots & \\ & & M^{e,l}_{K^e} \end{bmatrix},$$

for $l = 1, 2$. Each block $M_k^{e,l}$ is associated to the macro-region Ω_k^e and

$$M_k^{e,l}(i,j) = \left(\rho^e \Psi_j^e, \Psi_i^e\right)_{\Omega_k^e} \qquad \forall i,j = a_k, \dots, b_k.$$

With the same argument, the acoustic mass matrix $M^a \in \mathbb{R}^{N_{tot}^a \times N_{tot}^a}$ is related to the first term of equation (2.9) and

$$M^a(i,j) = \left(\frac{1}{\rho^a c^2}\Psi_j^a, \Psi_i^a\right)_{\Omega^a} \qquad \forall i,j = 1, \dots, N_{tot}^a.$$

Stiffness matrices

The matrix $A^e \in \mathbb{R}^{2N_{tot}^e \times 2N_{tot}^e}$ is associated to the second term of equation (2.8), that is the bilinear form $\mathcal{A}^e(\cdot,\cdot)$, and it takes the form

$$A^e = \begin{bmatrix} A^{e,1} & A^{e,2} \\ A^{e,3} & A^{e,4} \end{bmatrix},$$

where each $A^{e,l}$, $l = 1, \dots, 4$, has a block diagonal structure

$$A^{e,l} = \begin{bmatrix} A_1^{e,l} & & \\ & \ddots & \\ & & A_{K^e}^{e,l} \end{bmatrix}.$$

Each block $A_k^{e,l}$ is associated to the macro-region Ω_k^e and

$$\begin{aligned} A_k^{e,1}(i,j) &= \left(\sigma(\boldsymbol{\Psi}_j^{e,1}), \epsilon(\boldsymbol{\Psi}_i^{e,1})\right)_{\Omega_k^e}, & A_k^{e,2}(i,j) &= \left(\sigma(\boldsymbol{\Psi}_j^{e,2}), \epsilon(\boldsymbol{\Psi}_i^{e,1})\right)_{\Omega_k^e}, \\ A_k^{e,3}(i,j) &= \left(\sigma(\boldsymbol{\Psi}_j^{e,1}), \epsilon(\boldsymbol{\Psi}_i^{e,2})\right)_{\Omega_k^e}, & A_k^{e,4}(i,j) &= \left(\sigma(\boldsymbol{\Psi}_j^{e,2}), \epsilon(\boldsymbol{\Psi}_i^{e,2})\right)_{\Omega_k^e}, \end{aligned}$$

for $i,j = a_k, \dots, b_k$, or, equivalently,

$$\begin{aligned} A_k^{e,1}(i,j) &= \left(\rho^e c_p^2 \partial_{x_1}\Psi_j^e, \partial_{x_1}\Psi_i^e\right)_{\Omega_k^e} + \left(\rho^e c_s^2 \partial_{x_2}\Psi_j^e, \partial_{x_2}\Psi_i^e\right)_{\Omega_k^e}, \\ A_k^{e,2}(i,j) &= \left(\rho^e (c_p^2 - 2c_s^2) \partial_{x_2}\Psi_j^e, \partial_{x_1}\Psi_i^e\right)_{\Omega_k^e} + \left(\rho^e c_s^2 \partial_{x_1}\Psi_j^e, \partial_{x_2}\Psi_i^e\right)_{\Omega_k^e}, \\ A_k^{e,3}(i,j) &= \left(\rho^e (c_p^2 - 2c_s^2) \partial_{x_1}\Psi_j^e, \partial_{x_2}\Psi_i^e\right)_{\Omega_k^e} + \left(\rho^e c_s^2 \partial_{x_2}\Psi_j^e, \partial_{x_1}\Psi_i^e\right)_{\Omega_k^e}, \\ A_k^{e,4}(i,j) &= \left(\rho^e c_p^2 \partial_{x_2}\Psi_j^e, \partial_{x_2}\Psi_i^e\right)_{\Omega_k^e} + \left(\rho^e c_s^2 \partial_{x_1}\Psi_j^e, \partial_{x_1}\Psi_i^e\right)_{\Omega_k^e}. \end{aligned}$$

With the same argument, the acoustic stiffness matrix $A^a \in \mathbb{R}^{N_{tot}^a \times N_{tot}^a}$ is associated to the second term of equation (2.9), that is the bilinear form $\mathcal{A}^a(\cdot,\cdot)$, and it takes the form

$$A^a(i,j) = \left(\frac{1}{\rho^a}\partial_{x_1}\Psi_j^a, \partial_{x_1}\Psi_i^a\right)_{\Omega^a} + \left(\frac{1}{\rho^a}\partial_{x_2}\Psi_j^a, \partial_{x_2}\Psi_i^a\right)_{\Omega^a} \quad \forall i,j = 1, \dots, N_{tot}^a.$$

Discontinuous Galerkin elastic matrix

The Discontinuous Galerkin elastic matrix $B^e \in \mathbb{R}^{2N^e_{tot}\times 2N^e_{tot}}$ corresponds to the bilinear form $\mathcal{B}^e(\cdot,\cdot)$ in (2.8). It takes the following form

$$B^e = \begin{bmatrix} B^{e,1} & B^{e,2} \\ B^{e,3} & B^{e,4} \end{bmatrix},$$

where

$$B^{e,l} = \begin{bmatrix} B^{e,l}_{1,1} & \cdots & B^{e,l}_{1,K^e} \\ \vdots & \ddots & \vdots \\ B^{e,l}_{K^e,1} & \cdots & B^{e,l}_{K^e,K^e} \end{bmatrix},$$

for $l = 1,\dots,4$. Each $B^{e,l}_{h,k}$ takes into account the transmission conditions (2.2) across $\mathcal{S}^e \cap \partial\Omega^e_h \cap \partial\Omega^e_k$, for $h,k = 1,\dots,K^e$.

$$B^{e,1}_{h,k}(i,j) = \sum_{m=1}^{M} \mathcal{B}^e(\boldsymbol{\Psi}^{e,1}_j, \boldsymbol{\Psi}^{e,1}_i)_{\gamma^e_m}, \qquad B^{e,2}_{h,k}(i,j) = \sum_{m=1}^{M} \mathcal{B}^e(\boldsymbol{\Psi}^{e,2}_j, \boldsymbol{\Psi}^{e,1}_i)_{\gamma^e_m},$$
$$B^{e,3}_{h,k}(i,j) = \sum_{m=1}^{M} \mathcal{B}^e(\boldsymbol{\Psi}^{e,1}_j, \boldsymbol{\Psi}^{e,2}_i)_{\gamma^e_m}, \qquad B^{e,4}_{h,k}(i,j) = \sum_{m=1}^{M} \mathcal{B}^e(\boldsymbol{\Psi}^{e,2}_j, \boldsymbol{\Psi}^{e,2}_i)_{\gamma^e_m},$$

for $i = a_h,\dots,b_h$ and $j = a_k,\dots,b_k$. More specifically we have

$$B^{e,1}_{h,k}(i,j) = \sum_{m=1}^{M} \Bigg[-\big(\{\sigma(\boldsymbol{\Psi}^{e,1}_j)\}, [\![\boldsymbol{\Psi}^{e,1}_i]\!]\big)_{\gamma^e_m} + \theta\big([\![\boldsymbol{\Psi}^{e,1}_j]\!], \{\sigma(\boldsymbol{\Psi}^{e,1}_i)\}\big)_{\gamma^e_m} + \eta_{\gamma^e_m}\big([\![\boldsymbol{\Psi}^{e,1}_j]\!], [\![\boldsymbol{\Psi}^{e,1}_i]\!]\big)_{\gamma^e_m} \Bigg],$$

$$B^{e,2}_{h,k}(i,j) = \sum_{m=1}^{M} \Bigg[-\big(\{\sigma(\boldsymbol{\Psi}^{e,2}_j)\}, [\![\boldsymbol{\Psi}^{e,1}_i]\!]\big)_{\gamma^e_m} + \theta\big([\![\boldsymbol{\Psi}^{e,2}_j]\!], \{\sigma(\boldsymbol{\Psi}^{e,1}_i)\}\big)_{\gamma^e_m} + \eta_{\gamma^e_m}\big([\![\boldsymbol{\Psi}^{e,2}_j]\!], [\![\boldsymbol{\Psi}^{e,1}_i]\!]\big)_{\gamma^e_m} \Bigg],$$

$$B^{e,3}_{h,k}(i,j) = \sum_{m=1}^{M} \Bigg[-\big(\{\sigma(\boldsymbol{\Psi}^{e,1}_j)\}, [\![\boldsymbol{\Psi}^{e,2}_i]\!]\big)_{\gamma^e_m} + \theta\big([\![\boldsymbol{\Psi}^{e,1}_j]\!], \{\sigma(\boldsymbol{\Psi}^{e,2}_i)\}\big)_{\gamma^e_m} + \eta_{\gamma^e_m}\big([\![\boldsymbol{\Psi}^{e,1}_j]\!], [\![\boldsymbol{\Psi}^{e,2}_i]\!]\big)_{\gamma^e_m} \Bigg],$$

$$B^{e,4}_{h,k}(i,j) = \sum_{m=1}^{M} \Bigg[-\big(\{\sigma(\boldsymbol{\Psi}^{e,2}_j)\}, [\![\boldsymbol{\Psi}^{e,2}_i]\!]\big)_{\gamma^e_m} + \theta\big([\![\boldsymbol{\Psi}^{e,2}_j]\!], \{\sigma(\boldsymbol{\Psi}^{e,2}_i)\}\big)_{\gamma^e_m} + \eta_{\gamma^e_m}\big([\![\boldsymbol{\Psi}^{e,2}_j]\!], [\![\boldsymbol{\Psi}^{e,2}_i]\!]\big)_{\gamma^e_m} \Bigg].$$

Clearly, if Ω_h^e and Ω_k^e are not two neighbouring elements, the intersection $\mathcal{S}^e \cap \partial\Omega_h^e \cap \partial\Omega_k^e$ will be empty. Thus, the corresponding DG matrices will be void.

Viscoelastic damping matrices

As mentioned in Chapter 1, in order to better modeling the behavior of viscoelastic materials, it is sometimes useful introducing the damping term (1.2). This turns out in an additional external force

$$\mathbf{F}_{visc}^e = -D^e\mathbf{U}^e - E^e\dot{\mathbf{U}}^e,$$

where $D^e, E^e \in \mathbb{R}^{2N_{tot}^e \times 2N_{tot}^e}$ and

$$D^e = \begin{bmatrix} D^{e,1} & 0 \\ 0 & D^{e,2} \end{bmatrix}, \qquad E^e = \begin{bmatrix} E^{e,1} & 0 \\ 0 & E^{e,2} \end{bmatrix}.$$

Each $D^{e,l}, E^{e,l}$, $l = 1, 2$, has a block diagonal structure, i.e.,

$$D^{e,l} = \begin{bmatrix} D_1^{e,l} & & \\ & \ddots & \\ & & D_{K^e}^{e,l} \end{bmatrix}, \qquad E^{e,l} = \begin{bmatrix} E_1^{e,l} & & \\ & \ddots & \\ & & E_{K^e}^{e,l} \end{bmatrix}.$$

Each block $D_k^{e,l}, E_k^{e,l}$ is associated to the macro-region Ω_k^e and takes the form

$$\begin{aligned} D_k^{e,l}(i,j) &= \left(\rho^e \xi^2 \Psi_j^e, \Psi_i^e\right)_{\Omega_k^e} \qquad \forall i,j = a_k, \ldots, b_k, \\ E_k^{e,l}(i,j) &= \left(2\rho^e \xi \Psi_j^e, \Psi_i^e\right)_{\Omega_k^e} \qquad \forall i,j = a_k, \ldots, b_k. \end{aligned}$$

Absorbing boundary conditions matrices

As described in Chapter 1, absorbing, or non-reflecting, boundary conditions have the effect of introducing some fictitious tractions on the boundary $\Gamma_{NR} = \Gamma_{NR}^e \cup \Gamma_{NR}^a$.
On Γ_{NR}^e, zero and first-order boundary conditions are expressed by (1.6) and(1.8), respectively. The corresponding fictitious traction $\tilde{\mathbf{t}}^e$ are described in (1.7) and (1.9), respectively. As one can see, $\tilde{\mathbf{t}}^e$ involves space and time derivatives of $\mathbf{u}$, thus the discretized boundary conditions take the form

$$\mathbf{F}_{abc}^e = R^e\mathbf{U}^e + S^e\dot{\mathbf{U}}^e,$$

where $R^e, S^e \in \mathbb{R}^{2N_{tot}^e \times 2N_{tot}^e}$ and

$$R^e = \begin{bmatrix} 0 & R^{e,1} \\ R^{e,2} & 0 \end{bmatrix}, \qquad S^e = \begin{bmatrix} S^{e,1} & S^{e,2} \\ S^{e,3} & S^{e,4} \end{bmatrix}.$$

Each block $R^{e,l}$, $l = 1, 2$, and $S^{e,l}$, $l = 1, \ldots, 4$, has the following diagonal structure

$$R^{e,l} = \begin{bmatrix} R_1^{e,l} & & \\ & \ddots & \\ & & R_{K^e}^{e,l} \end{bmatrix}, \qquad S^{e,l} = \begin{bmatrix} S_1^{e,l} & & \\ & \ddots & \\ & & S_{K^e}^{e,l} \end{bmatrix},$$

where $R_k^{e,l}$ and $S_k^{e,l}$ are associated to the macro-region Ω_k^e. Either in the case of zero and first-order absorbing boundary conditions, each $S_k^{e,l}$ takes the following form

$$\begin{aligned} S_k^{e,1}(i,j) &= \big(-\rho^e (c_p n_1^2 + c_s n_2^2) \Psi_j^e, \Psi_i^e \big)_{\partial\Omega_k^e \cap \Gamma_{NR}^e}, \\ S_k^{e,2}(i,j) &= \big(-\rho^e n_1 n_2 (c_p - c_s) \Psi_j^e, \Psi_i^e \big)_{\partial\Omega_k^e \cap \Gamma_{NR}^e}, \\ S_k^{e,3}(i,j) &= \big(-\rho^e n_1 n_2 (c_p - c_s) \Psi_j^e, \Psi_i^e \big)_{\partial\Omega_k^e \cap \Gamma_{NR}^e}, \\ S_k^{e,4}(i,j) &= \big(-\rho^e (c_p n_2^2 + c_s n_1^2) \Psi_j^e, \Psi_i^e \big)_{\partial\Omega_k^e \cap \Gamma_{NR}^e}, \end{aligned}$$

for $i, j = a_k, \ldots, b_k$. On the other hand, the terms $R_k^{e,l}$ depend on the order of the absorbing boundary conditions. In fact, for the zero-order ones, $R_k^{e,l} = 0$ for any $k = 1, \ldots, K^e$ and $l = 1, 2$ (see (1.7)). Otherwise, in the case of first-order conditions, we have

$$\begin{aligned} R_k^{e,1}(i,j) &= \big(-\rho^e c_s (c_p - 2c_s)(n_1^2 n_2 + n_2^3) \partial_{x_1} \Psi_j^e, \Psi_i^e \big)_{\partial\Omega_k^e \cap \Gamma_{NR}^e} \\ &\quad + \big(-\rho^e c_s (2c_s - c_p)(n_1^3 + n_1 n_2^2) \partial_{x_2} \Psi_j^e, \Psi_i^e \big)_{\partial\Omega_k^e \cap \Gamma_{NR}^e}, \\ R_k^{e,2}(i,j) &= \big(-\rho^e c_s (2c_s - c_p)(n_1^2 n_2 + n_2^3) \partial_{x_1} \Psi_j^e, \Psi_i^e \big)_{\partial\Omega_k^e \cap \Gamma_{NR}^e} \\ &\quad + \big(-\rho^e c_s (c_p - 2c_s)(n_1^3 + n_1 n_2^2) \partial_{x_2} \Psi_j^e, \Psi_i^e \big)_{\partial\Omega_k^e \cap \Gamma_{NR}^e}, \end{aligned}$$

for $i, j = a_k, \ldots, b_k$ (see (1.9)). We recall that n_1 and n_2 are the component of $\mathbf{n}^e = (n_1, n_2)^T$, that is the outward pointing unit normal vector to the boundary Γ_{NR}^e. Clearly, if $\partial\Omega_k^e \cap \Gamma_{NR}^e = \emptyset$, the corresponding matrices $S_k^{e,l}$ and $R_k^{e,l}$ will be void.

On Γ_{NR}^a, only zero-order boundary conditions are performed (see (1.11)). The corresponding fictitious traction $\tilde{t}^a$ is expressed by (1.12) and thus the discretized boundary conditions take the form

$$\mathbf{F}_{abc}^a = S^a \dot{\mathbf{U}}^a,$$

where $S^a \in \mathbb{R}^{N_{tot}^a \times N_{tot}^a}$ is expressed by

$$S^a(i,j) = \big(-\frac{1}{\rho^a c} \Psi_j^a, \Psi_i^a \big)_{\Gamma_{NR}^a} \qquad \forall i, j = 1, \ldots, N_{tot}^a.$$

Coupling matrices

The coupling matrices $C^{e(a)}$ are related to the bilinear forms $\mathcal{C}^{e(a)}(\cdot,\cdot)$, described in (2.6) and (2.7), respectively.
On one hand, looking first at $C^e \in \mathbb{R}^{2N^e_{tot}\times N^a_{tot}}$; we have that

$$C^e = \begin{bmatrix} C^{e,1} \\ C^{e,2} \end{bmatrix},$$

where each $C^{e,l} \in \mathbb{R}^{N^e_{tot}\times N^a_{tot}}$, for $l = 1, 2$, and has the following structure

$$C^{e,l} = \begin{bmatrix} C^{e,l}_1 \\ \vdots \\ C^{e,l}_{K^e} \end{bmatrix}.$$

Each $C^{e,l}_k$ takes into account the coupling along $\Gamma^i \cap \partial\Omega^e_k$ and it is such that

$$C^{e,1}_k(i,j) = \sum_{n=1}^{N} \mathcal{C}^e(\Psi^a_j, \boldsymbol{\Psi}^{e,1}_i)_{\gamma^{ea}_n} = \sum_{n=1}^{N} -(\Psi^a_j n^a_1, \Psi^e_i)_{\gamma^{ea}_n} = \sum_{n=1}^{N} (\Psi^a_j n^e_1, \Psi^e_i)_{\gamma^{ea}_n},$$
$$C^{e,2}_k(i,j) = \sum_{n=1}^{N} \mathcal{C}^e(\Psi^a_j, \boldsymbol{\Psi}^{e,2}_i)_{\gamma^{ea}_n} = \sum_{n=1}^{N} -(\Psi^a_j n^a_2, \Psi^e_i)_{\gamma^{ea}_n} = \sum_{n=1}^{N} (\Psi^a_j n^e_2, \Psi^e_i)_{\gamma^{ea}_n},$$

for $i = a_k, \ldots, b_k$ and $j = 1, \ldots, N^a_{tot}$.

On the other hand, the matrix $C^a \in \mathbb{R}^{N^a_{tot}\times 2N^e_{tot}}$ takes the form

$$C^a = \begin{bmatrix} C^{a,1} & C^{a,2} \end{bmatrix},$$

where each $C^{a,l} \in \mathbb{R}^{N^a_{tot}\times N^e_{tot}}$, for $l = 1, 2$, has the following structure

$$C^{a,l} = \begin{bmatrix} C^{a,l}_1 & \cdots & C^{a,l}_{K^e} \end{bmatrix}.$$

Each $C^{a,l}_k$ takes into account the coupling along $\Gamma^i \cap \partial\Omega^e_k$ and it is such that

$$C^{a,1}_k(i,j) = \sum_{n=1}^{N} \mathcal{C}^a(\boldsymbol{\Psi}^{e,1}_j, \Psi^a_i)_{\gamma^{ea}_n} = \sum_{n=1}^{N} -(\Psi^e_j n^e_1, \Psi^a_i)_{\gamma^{ea}_n} = \sum_{n=1}^{N} (\Psi^e_j n^a_1, \Psi^a_i)_{\gamma^{ea}_n},$$
$$C^{a,2}_k(i,j) = \sum_{n=1}^{N} \mathcal{C}^a(\boldsymbol{\Psi}^{e,2}_j, \Psi^a_i)_{\gamma^{ea}_n} = \sum_{n=1}^{N} -(\Psi^e_j n^e_2, \Psi^a_i)_{\gamma^{ea}_n} = \sum_{n=1}^{N} (\Psi^e_j n^a_2, \Psi^a_i)_{\gamma^{ea}_n},$$

for $i = 1, \ldots, N^a_{tot}$ and $j = a_k, \ldots, b_k$. We recall that $n^e_{1(2)}$ and $n^a_{1(2)}$ are the first (resp. second) component of the outward pointing unit normal vector to the elasto-acoustic interface Γ^i with respect to the solid and the acoustic part, respectively. Clearly, if $\partial\Omega^e_k \cap \Gamma^i = \emptyset$, the corresponding matrices $C^{e,l}_k$ and $C^{a,l}_k$ will be void.

External loads vectors

The vectors of externally applied loads are $\mathbf{F}^e \in \mathbb{R}^{2N^e_{tot}}$ and $\mathbf{F}^a \in \mathbb{R}^{N^a_{tot}}$. They take into account volume forces and Neumann loads.
Thus, in the elastic part we have

$$\mathbf{F}^e = \begin{bmatrix} \mathbf{F}^{e,1} \\ \mathbf{F}^{e,2} \end{bmatrix},$$

where, for each $l = 1, 2$

$$F^{e,l}_i = \left(\mathbf{f}^e, \mathbf{\Psi}^{e,l}_i\right)_{\Omega^e} + \left(\mathbf{t}^e, \mathbf{\Psi}^{e,l}_i\right)_{\Gamma^e_N} \qquad \forall i = 1, \ldots, N^e_{tot}.$$

At the same way, in the acoustic part we have

$$F^a_i = \left(f^a, \Psi^a_i\right)_{\Omega^a} + \left(t^a, \Psi^a_i\right)_{\Gamma^a_N} \qquad \forall i = 1, \ldots, N^a_{tot}.$$

Chapter 4

Time discretization

In this chapter, we describe how the second ordinary differential system of equations (3.1) – (3.2) can be solved. The temporal approach that we have performed in the code is a simple and very popular time-stepping scheme for wave propagation: the leap-frog (LF) method (e.g. [13, 31, 30, 32, 24, 15, 12, 14, 36, 4]). Based on a second order finite difference scheme, LF method is thus second order accurate, explicit and conditionally stable.
In the first part of this chapter, we show how the leap-frog scheme is implemented and how it leads to the fully-discretized formulation of the problem. In the second part, we focus on the Courant-Friedrichs-Lewy (CFL) stability condition, which links spatial and temporal discretization parameters in order to make the numerical solution of (2.10) stable.

4.1 The leap-frog method

After dividing the time interval $[0, T]$ into N_t time steps, each of size $\Delta t = T/N_t$, we replace first and second times derivatives in (3.1) – (3.2) with

$$\dot{\mathbf{U}}(t) \simeq \frac{\mathbf{U}_{n+1} - \mathbf{U}_{n-1}}{2\Delta t}, \qquad \ddot{\mathbf{U}}(t) \simeq \frac{\mathbf{U}_{n+1} - 2\mathbf{U}_n + \mathbf{U}_{n-1}}{\Delta t^2},$$

and

$$\dot{\mathbf{P}}(t) \simeq \frac{\mathbf{P}_{n+1} - \mathbf{P}_{n-1}}{2\Delta t}, \qquad \ddot{\mathbf{P}}(t) \simeq \frac{\mathbf{P}_{n+1} - 2\mathbf{P}_n + \mathbf{P}_{n-1}}{\Delta t^2},$$

where $\mathbf{U}_n = \mathbf{U}(t_n)$, $\mathbf{P}_n = \mathbf{P}(t_n)$ and $t_n = n\Delta t \ \forall n = 1, \ldots, N_t$.

Giving the initial conditions $\mathbf{U}_0 = \mathbf{U}(0)$, $\mathbf{U}_1 = \mathbf{U}(\Delta t)$ and $\mathbf{P}_0 = \mathbf{P}(0)$, $\mathbf{P}_1 = \mathbf{P}(\Delta t)$, we thus obtain the fully-discretized problem

$$M^e\frac{\mathbf{U}_{n+1}-2\mathbf{U}_n+\mathbf{U}_{n-1}}{\Delta t^2}+(E^e-S^e)\frac{\mathbf{U}_{n+1}-\mathbf{U}_{n-1}}{2\Delta t}+(A^e+B^e+D^e-R^e)\mathbf{U}_n+$$
$$+C^e\mathbf{P}_n=\mathbf{F}_n^e,\qquad\qquad \forall n=1,\dots,N_t-1,$$

$$M^a\frac{\mathbf{P}_{n+1}-2\mathbf{P}_n+\mathbf{P}_{n-1}}{\Delta t^2}-S^a\frac{\mathbf{P}_{n+1}-\mathbf{P}_{n-1}}{2\Delta t}+A^e\mathbf{P}_n+$$
$$+C^a\frac{\mathbf{U}_{n+1}-2\mathbf{U}_n+\mathbf{U}_{n-1}}{\Delta t^2}=\mathbf{F}_n^a,\qquad\qquad \forall n=1,\dots,N_t-1, \tag{4.1}$$

where $\mathbf{F}_n^{e(a)}=\mathbf{F}^{e(a)}(t_n)$.
Thus, at each step, giving $\mathbf{U}_{n-1},\mathbf{U}_n,\mathbf{P}_{n-1},\mathbf{P}_n$, we first determine $\mathbf{U}_{n+1}$ solving

$$\begin{aligned}\big(2M^e+\Delta t(E^e-S^e)\big)\mathbf{U}_{n+1}=&2\Delta t^2\mathbf{F}_n^e+\big(-2M^e+\Delta t(E^e-S^e)\big)\mathbf{U}_{n-1}+\\&+\big(4M^e-2\Delta t^2(A^e+B^e+D^e-R^e)\big)\mathbf{U}_n-\\&-2\Delta t^2C^e\mathbf{P}_n.\end{aligned} \tag{4.2}$$

Then, we compute $\mathbf{P}_{n+1}$ from

$$\begin{aligned}(2M^a-\Delta tS^a)\mathbf{P}_{n+1}=&2\Delta t^2\mathbf{F}_n^a+(-2M^a-\Delta tS^a)\mathbf{P}_{n-1}+\\&+(4M^a-2\Delta t^2A^a)\mathbf{P}_n-\\&-2C^a(\mathbf{U}_{n+1}-2\mathbf{U}_n+\mathbf{U}_{n-1}).\end{aligned} \tag{4.3}$$

We note that the updated elastic displacement $\mathbf{U}_{n+1}$ plays the role of right-hand side term in the acoustic equation, as an effect of the elasto-acoustic coupling which links the two equations at each time step.

We give here a sample of the LF scheme:

LF scheme:
Given some initial conditions $\mathbf{U}_0,\mathbf{U}_1$ and $\mathbf{P}_0,\mathbf{P}_1$,
for $n=1,...,N_t-1$ **do**
solve equation (4.2) for $\mathbf{U}_{n+1}$;
solve equation (4.3) for $\mathbf{P}_{n+1}$;
end for

The LF method provides a second-order accuracy, so it represents a good choice as long as the spatial discretization order is not too high. In the case

of very fine meshes or very high spectral degrees, different time discretization methods can be used, such as high-order Runge-Kutta methods [33]. This should assure a balance in the space-time discretization error, at price of increasing the computational cost.

4.2 CFL stability condition

In this section we are interested in determining the largest time step Δt that we are allowed to use in order to prevent possible unphysical oscillations in the numerical solution.
In the literature, the so-called Courant-Friedrichs-Lewy (CFL) imposes a restriction on Δt of the form

$$\Delta t \leq C_{CFL} \frac{\Delta x}{\tilde{c}},$$

where Δx is the minimum distance between two neighbouring discretization nodes and $\tilde{c}$ is a characteristic velocity. The Courant number C_{CFL} depends on the dimension, the order of the scheme and the mesh geometry. In some applications it is empirically chosen between 0.3 and 0.6 (see, for example, [30, 29, 38, 11]).
As one can see, the CFL condition relates spatial and time discretization. Thus, as long as the mesh is refined and/or the spectral degree is increased the critical time step has to be set according to

$$\Delta t \leq \min\Big\{ C_1^e \frac{h_1^e}{c_{p,1}(N_1^e)^2}; \ldots; C_{K^e}^e \frac{h_{K^e}^e}{c_{p,K^e}(N_{K^e}^e)^2}; C^a \frac{h^a}{c(N^a)^2} \Big\},$$

in order to prevent numerical instability.
In our case (as in [15]), C_k^e, h_k^e, $c_{p,k}$ and N_k^e are, respectively, a positive constant, the typical mesh size, the speed of P-waves and the spectral degree associated to the elastic macro region $\Omega_k^e \forall k = 1, \ldots, K^e$. Analogously, C^a, h^a, c and N^a are related to the acoustic subdomain Ω^a. The constants C_k^e and C^a depend on the properties of the elastic and acoustic media, i.e., densities $\rho^{e(a)}$, Lamé parameters λ, μ, velocity of waves propagation c, and, in the case of the elastic ones, also on the Discontinuous Galerkin scheme adopted (see Section 2.1).

Chapter 5

Numerical results

In this chapter we validate the numerical method presented in Chpater 2 – 4 on test problems and we apply it to some applications of geophysical interest, addressing both two and three dimensional benchmarks.
In order to verify the accuracy of the DGSE method and its order of convergence, we present first a two-dimensional test case, with known exact solution. Then, in a second example, we simulate a real benchmark and we analyze the wave propagation and the effect of the elasto-acoustic interface.
In the second part of this chapter, we extend the previous test case in a three-dimensional setting and we test the accuracy of the method both with matching and non-matching grids. Finally, a more realistic case is presented in the last example, where we investigate whether or not the presence of a fluid layer affects the propagation seismic waves.
We recall that the numerical code implemented for this work is included in the SPEED code (https://speed.mox.polimi.it).

5.1 Two-dimensional problems

We start by considering a two-dimensional example for which the analytical solution is known. Thus, we investigate the convergence properties of DGSE method both with respect to spatial and temporal discretization parameters. Next, we present a test of geophysical interest, where non-reflecting boundary conditions are applied on the whole external boundary, both elastic and acoustic.
For both cases, we consider the computational domain shown in Figure 1.3 and reported in Figure 5.1. More precisely, we set $\Omega^e = (-1, 0) \times (0, 1)$ and $\Omega^a = (0, 1)^2$. The elasto-acoustic interface is defined as follows

$$\Gamma^i = \big\{(x, y) \in \mathbb{R}^2 : x = 0 \text{ and } 0 \leq y \leq 1\big\}.$$

Moreover, we suppose homogeneous elastic and acoustic materials. Thus, spatial discretization does not deal with macro-partitions and it will concern only into a meso (mesh) and a micro (GLL interpolation points) partition. The DG approach is then applied only to the elasto-acoustic interface Γ^i.

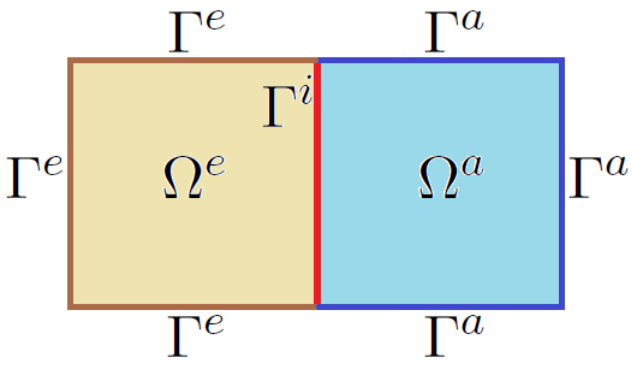

Figure 5.1: Two-dimensional multiphysical domain $\Omega = \Omega^e \cup \Omega^a$. External boundary is split into Γ^e and Γ^a, whereas internal elasto-acoustic interface is called Γ^i.

Example 1. Accuracy and convergence properties

In this first example, we are interested in testing the accuracy and the order of convergence of the proposed method.
We consider the domain shown in Figure 5.1. Spatial discretization is performed introducing two Cartesian matching grids $\mathcal{T}^e$ and $\mathcal{T}^a$ of size $h^e = h^a = 0.1$ and choosing the same spectral degree $N^e = N^a = 2$ in both Ω^e and Ω^a (for non-conforming meshes, see Section 4.2). Time discretization is performed with the leap-frog scheme presented in Chapter 4, choosing a maximum time of simulation $T = 5$ and a time step $\Delta t = 0.001$.
External forces $\mathbf{f}^e$ and f^a are chosen such that the exact solution of (1.1) – (1.5) is

$$\begin{aligned} \mathbf{u_{ex}} &= \left(\cos\left(\frac{\omega \cdot \mathbf{x}}{c_p}\right)\cos(\omega t), \cos\left(\frac{\omega \cdot \mathbf{x}}{c_s}\right)\cos(\omega t)\right)^T, \\ p_{ex} &= \omega\rho^a \cos\left(\frac{\omega \cdot \mathbf{x}}{c}\right)\cos(\omega t), \end{aligned} \tag{5.1}$$

where $\omega = (\omega, 0)^T$, with $\omega = 4\pi$. We choose for the elastic region $\rho^e = 2.7$, $c_p = 6.2$ and $c_s = 3.12$, while for the acoustic one $\rho^a = 1$ and $c = 1$. All these quantities are supposed to be dimensionless.
Initial conditions and Dirichlet boundary conditions on the whole external

boundary are defined according to (5.1). Note that, in this example, we suppose $\Gamma_{NR} = \Gamma_N = \emptyset$ and $\partial\Omega = \Gamma_D$.
In Figure 5.2 – 5.5, we compare the numerical solutions with the analytical one in some points of the domain. More specifically, Figure 5.2 and Figure 5.3 show the elastic displacement at $(-0.6, 0.5)$ and $(-0.2, 0.5)$, while Figure 5.4 and Figure 5.5 show the acoustic pressure field at $(0.4, 0.5)$ and $(0.8, 0.5)$. As one can see, the numerical results are in good agreement with the analytical ones.

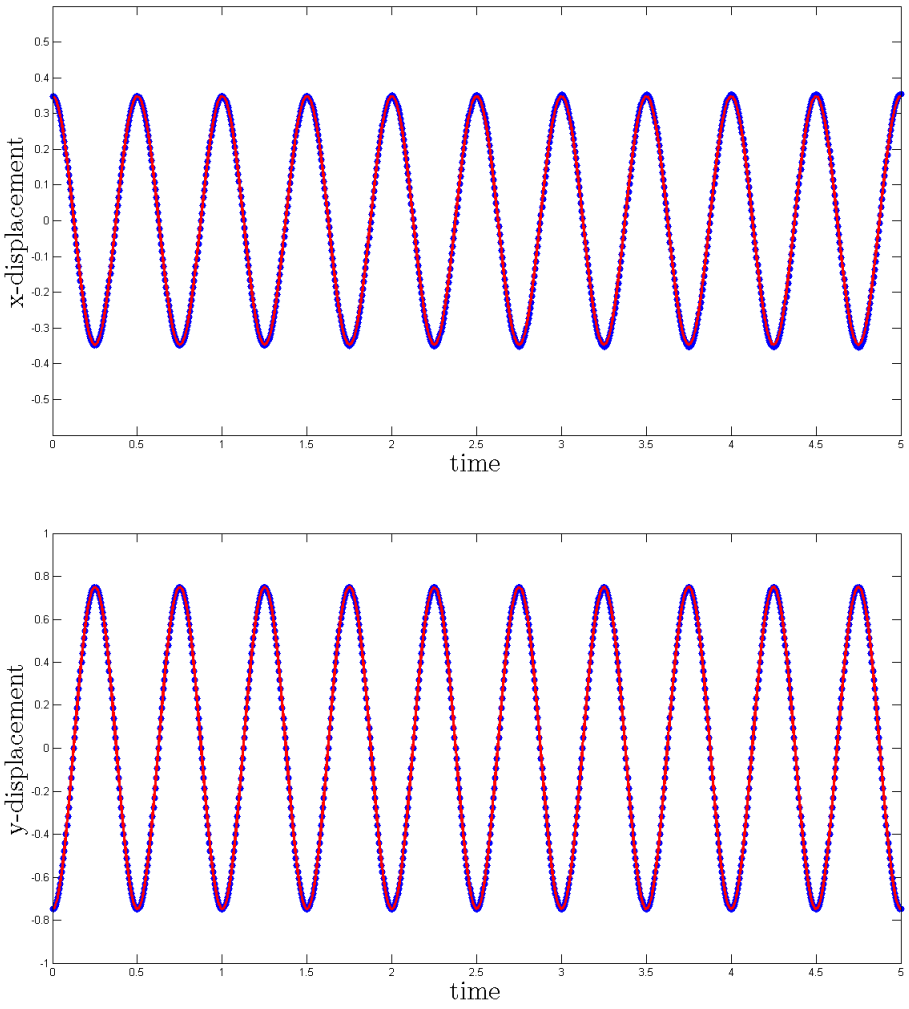

Figure 5.2: Example 1. Elastic displacement at point $\mathbf{x} = (-0.6, 0.5)$. Numerical results (blue dots $\bullet$) are compared with analytical ones (red line $\sim$).

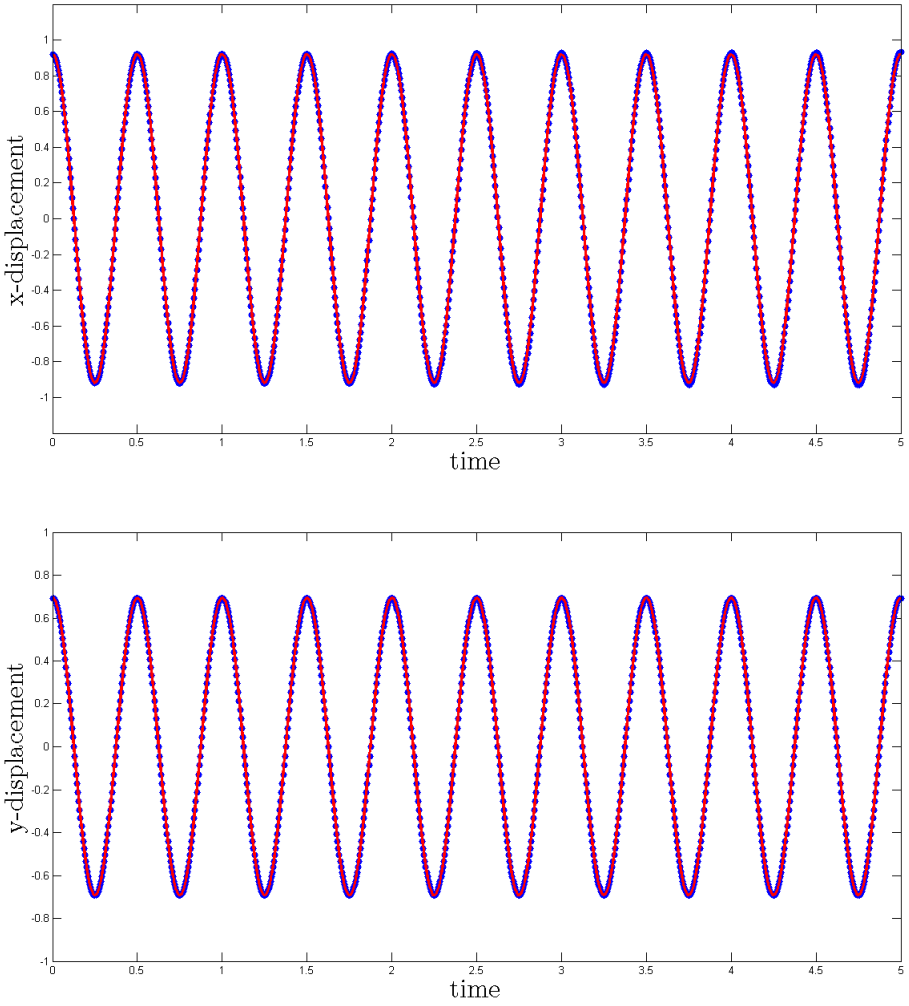

Figure 5.3: Example 1. Elastic displacement at point $\mathbf{x} = (-0.2, 0.5)$. Numerical results (blue dots $\bullet$) are compared with analytical ones (red line $\sim$).

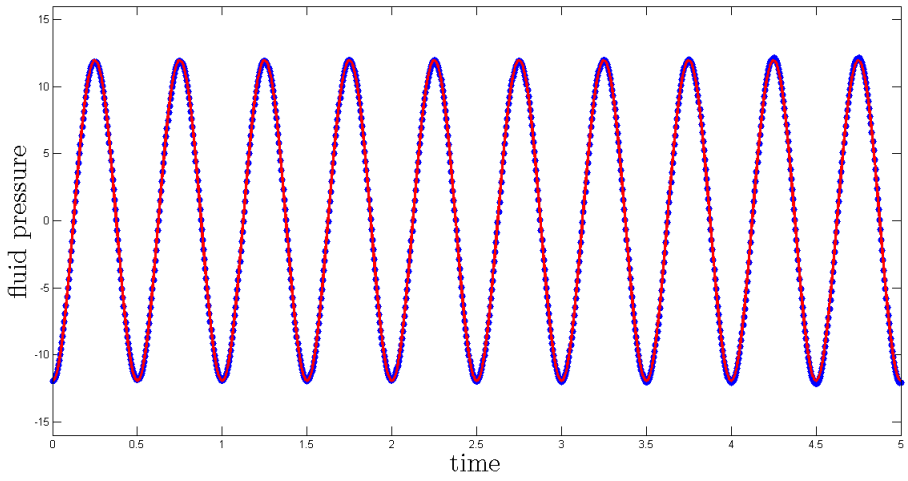

Figure 5.4: Example 1. Acoustic pressure field at point $\mathbf{x} = (0.4, 0.5)$. Numerical results (blue dots $\bullet$) are compared with analytical ones (red line $\sim$).

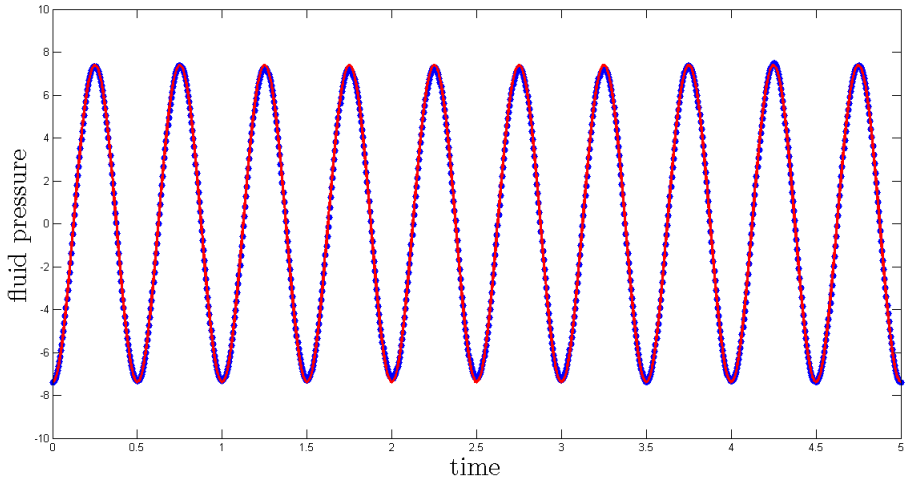

Figure 5.5: Example 1. Acoustic pressure field at point $\mathbf{x} = (0.8, 0.5)$. Numerical results (blue dots $\bullet$) are compared with analytical ones (red line $\sim$).

Now, we are interested in checking the convergence properties of the numerical method implemented. In particular, we investigate the convergence of DGSE method coupled with the leap-frog scheme, with respect to the spatial discretization parameters (h^e, h^a) and (N^e, N^a), and the temporal discretization parameter Δt.
We thus report, in Figure 5.6 – 5.8, the computed L^2-error as a function of space and time discretization parameters. More precisely:

- varying $N^{e(a)} = 2, 3, 4, 5$, with fixed Δt and $h^{e(a)}$ (see Figure 5.6). From a theoretical analysis (see [39, p. 228]), since the solution is analytical, we expect an exponential convergence, i.e.,

$$\|\mathbf{u_N} - \mathbf{u_{ex}}\|_{L^2(\Omega^e)} = \mathcal{O}\big(e^{-\gamma N^e}\big),$$
$$\|p_N - p_{ex}\|_{L^2(\Omega^a)} = \mathcal{O}\big(e^{-\beta N^a}\big);$$

- varying $h^{e(a)} = 0.1, 0.05, 0.025$, with fixed Δt and $N^{e(a)}$ (see Figure 5.7). In this case an algebraic convergence is expected (again, see [39, p. 228]). Moreover, from our knowledge on Finite Element method (see [39, p. 97]), it seems reasonable that

$$\|\mathbf{u_N} - \mathbf{u_{ex}}\|_{L^2(\Omega^e)} = \mathcal{O}\big((h^e)^{N^e+1}\big),$$
$$\|p_N - p_{ex}\|_{L^2(\Omega^a)} = \mathcal{O}\big((h^a)^{N^a+1}\big);$$

- varying $\Delta t = 0.3125, 0.625, 1.25, 2.5, 5 \times 10^{-3}$, with fixed $h^{e(a)}$ and $N^{e(a)}$ (see Figure 5.8). Since the leap-frog scheme is a second-order method, we expect a quadratic convergence, that is

$$\|\mathbf{u_N} - \mathbf{u_{ex}}\|_{L^2(\Omega^e)} = \mathcal{O}\big(\Delta t^2\big),$$
$$\|p_N - p_{ex}\|_{L^2(\Omega^a)} = \mathcal{O}\big(\Delta t^2\big).$$

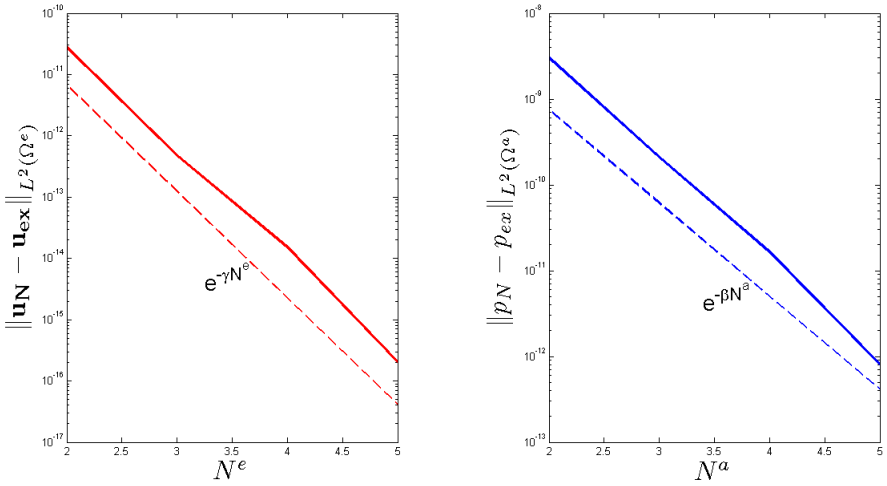

Figure 5.6: Example 1. Computed L^2-errors for elastic displacement (left) and acoustic pressure (right) as a function of polynomial approximation degrees N^e and N^a. Continuous lines are the computed errors, while dashed lines are the exponential decays.

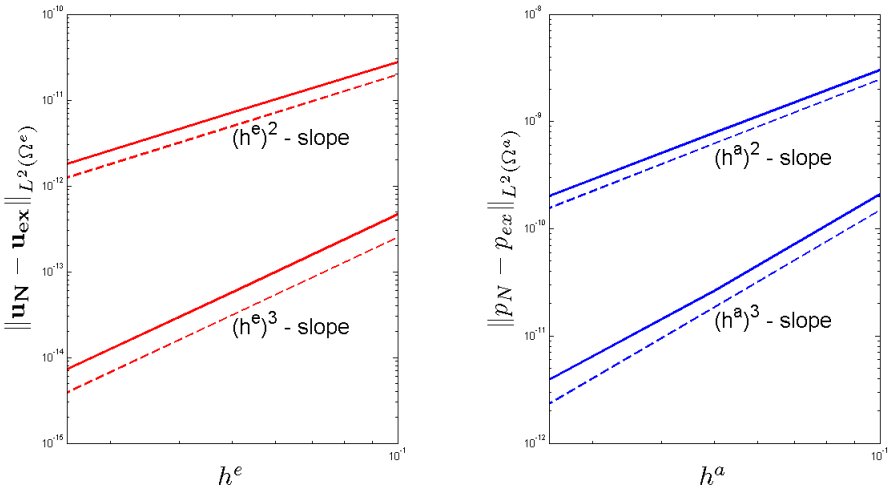

Figure 5.7: Example 1. Computed L^2-errors for elastic displacement (left) and acoustic pressure (right) as a function of the mesh sizes h^e and h^a. Continuous lines are the computed errors, while dashed lines are the algebraic decays. Two trials are shown: the first one (on the top) is obtained with $N^e = N^a = 2$, while the other one (on the bottom) is obtained with $N^e = N^a = 3$.

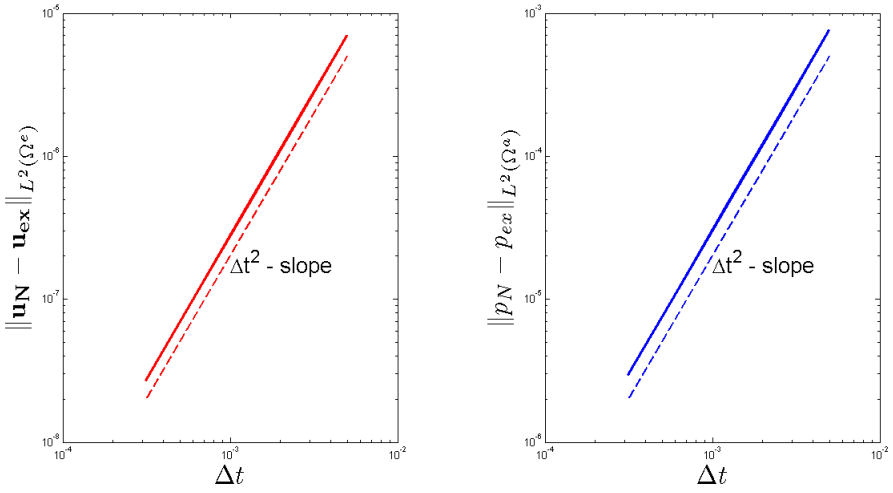

Figure 5.8: Example 1. Computed L^2-errors for elastic displacement (left) and acoustic pressure (right) as a function of the time step Δt^2. Continuous lines are the computed errors, while dashed lines are the expected order of convergence.

We clearly observe an exponential decay of L^2-errors with respect to the spectral degrees N^e and N^a, the algebraic behavior with respect to the mesh sizes h^e and h^a and the quadratic behavior with respect to the time step Δt. However, the algebraic convergence with respect to the mesh size is one order less than the optimal decay. Probably this behavior is due to the skew-symmetric coupling used in the numerical simulations (displacement-pressure field formulation). This will be the subject of further theoretical investigation.

Example 2. Simulated seismogram

In this second two-dimensional example, we consider the same computational domain of the previous case (see Figure 5.1) and, in order to simulate aseismic source, we place a point source load of the form

$$f^a = \begin{cases} -1152\pi\Big(1 - 1152\pi(t-1)^2\Big)e^{-576\pi(t-1)^2}, & \mathbf{x} = (0.9, 0.5), \\ 0, & \mathbf{x} \neq (0.9, 0.5). \end{cases} \tag{5.2}$$

The time function f^a is a Ricker wave (see Figure 5.9), which is widely used in seismology and is set in the acoustic subdomain. On the other hand, the elastic external load function $\mathbf{f}^e$ is null.
The material parameters are $\rho^e = 2.5$, $c_p = 4$ and $c_s = 2$ for the elastic

domain and $\rho^a = 1$ and $c = 1.5$ for the acoustic one. We recall that these quantities are supposed to be dimensionless.
DGSE spatial discretization is performed with two conforming grids of size $h^e = h^a = 0.05$ and spectral degree $N^e = N^a = 4$. Temporal discretization is performed with $T = 5$ and $\Delta t = 0.0001$.
In this case, we consider zero-order absorbing boundary condition on the whole external boundary Γ, i.e., $\Gamma_D = \Gamma_N = \emptyset$ and $\Gamma = \Gamma_{NR}$.
Moreover, we suppose homogeneous initial conditions for $\mathbf{u}$ and p. Then, around the time $t = 1$, the Ricker function has a sort of impulse (see Figure 5.9), which generates an acoustic wave. This wave propagates through Ω^a and, when the elasto-acoustic interface Γ^i is reached, it turns out in elastic vibrations in Ω^e.

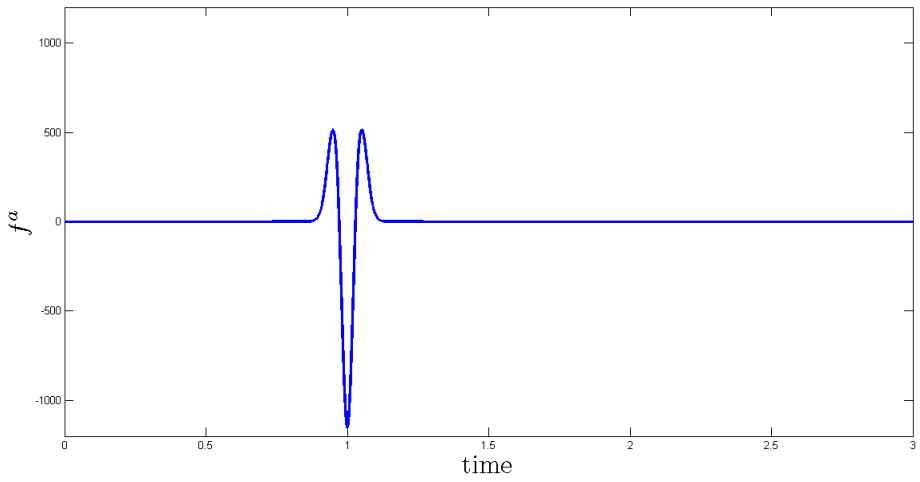

Figure 5.9: Example 2. Ricker time shape function f^a introduced in (5.2).

The following Figure 5.10 and Figure 5.11 show the elastic displacement at $(-0.3, 0.5)$ and the acoustic pressure field at the point $(0.7, 0.5)$, respectively. We can clearly observe that the vertical displacement at $(-0.3, 0.5)$ is null. This is a natural consequence of the coupling: it propagates only longitudinal stresses through the elasto-acoustic interface, since fluids do not support shear stresses. Thus, since the monitored elastic point is horizontally aligned with the hypocentre, the vertical displacement vanishes.

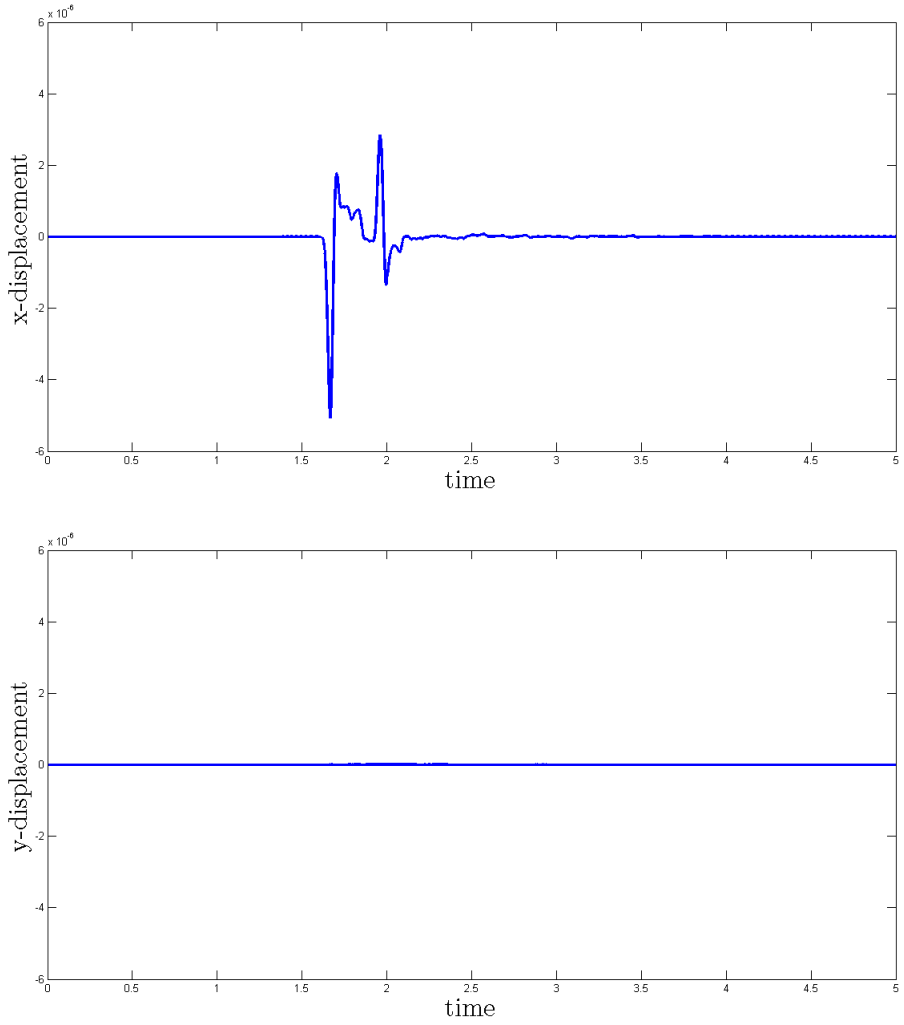

Figure 5.10: Example 2. Elastic displacement at point $\mathbf{x} = (-0.3, 0.5)$.

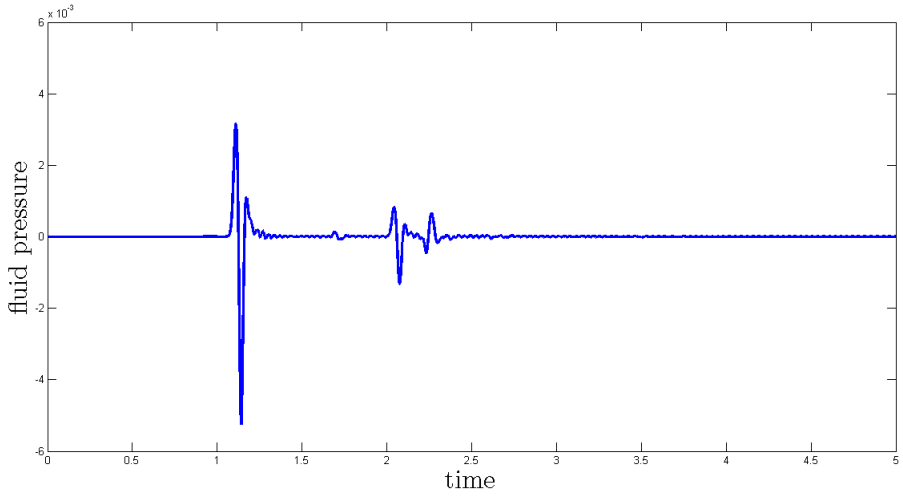

Figure 5.11: Example 2. Acoustic pressure field at point $\mathbf{x} = (0.7, 0.5)$.

5.2 Three-dimensional problems

We now show two relevant three-dimensional numerical applications of the proposed method. The main difference between the implementation of the algorithm in two or three dimensions consists in the assembly of the linear systems (3.1) – (3.2). In fact, due to the very large size of the matrices involved, they are not stored in memory, but it is directly computed their effect on the vectors $\mathbf{U}$ and $\mathbf{P}$. Moreover, to deal with realistic simulations, the three-dimensional code is manually designed for working in parallel machines, relying on the message passing technique.

The first example shown in this section is the three-dimensional extension of the previous two-dimensional test case treated in Section 4.1. We thus validate the numerical scheme comparing the numerical solution with the analytical one. Here, we consider either conforming and non-conforming discretizations.

In the second and last example we present the simulation of an earthquake in a cubic domain. In particular, we compare the wave motion in presence or not of a layer of fluid material and we investigate the effect of the elasto-acoustic interfaces.

Example 3. Accuracy

In this example, we check the accuracy of the three-dimensional numerical code. Thus, we consider the natural three-dimensional extension of the computational domain shown in Figure 5.1, that is made up by two adjacent cubes: $\Omega^e = (-1, 0) \times (0, 1)^2$ and $\Omega^a = (0, 1)^3$ (see Figure 5.12). The internal elasto-acoustic interface is thus

$$\Gamma^i = \big\{(x, y, z) \in \mathbb{R}^3 : x = 0 \ , \ 0 \leq y \leq 1 \text{ and } 0 \leq z \leq 1\big\}.$$

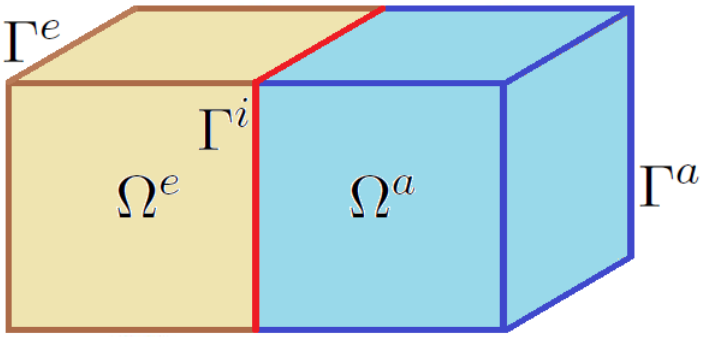

Figure 5.12: Example 3. Three-dimensional multiphysical domain $\Omega = \Omega^e \cup \Omega^a$. External boundary is split into Γ^e and Γ^a, whereas internal elasto-acoustic interface is called Γ^i.

We still consider homogeneous elastic and acoustic subdomains, i.e., we do not deal with macro partition. Thus, spatial discretization is performed with a meso partition of both Ω^e and Ω^a with two Cartesian conforming grids $\mathcal{T}^e$ and $\mathcal{T}^a$ of typical mesh size $h^e = h^a = 0.1$. Then, on each element of $\mathcal{T}^e$ and $\mathcal{T}^a$, we have adopted a polynomial approximation degree $N^e = N^a = 3$. Time discretization is performed with the leap-frog scheme introduced in Chpater 4, choosing a maximum time of simulation $T = 5$ and a time step $\Delta t = 0.0001$.
We consider an analytical solution given by

$$\begin{aligned} \mathbf{u_{ex}} &= \left(\cos\Big(\frac{\omega \cdot \mathbf{x}}{c_p}\Big)\cos(\omega t), \cos\Big(\frac{\omega \cdot \mathbf{x}}{c_s}\Big)\cos(\omega t), \cos\Big(\frac{\omega \cdot \mathbf{x}}{c_s}\Big)\cos(\omega t)\right)^T, \\ p_{ex} &= \omega \rho^a \cos\Big(\frac{\omega \cdot \mathbf{x}}{c}\Big)\cos(\omega t), \end{aligned} \tag{5.3}$$

where $\omega = (\omega, 0, 0)^T$, with $\omega = 4\pi$. The material parameters are the same of the two-dimensional test case, that are $\rho^e = 2.7$, $c_p = 6.2$ and $c_s = 3.12$ in

the elastic part, $\rho^a = 1$ and $c = 1$ in the acoustic one.
External forces $\mathbf{f}^e$ and f^a, such as initial conditions and Dirichlet boundary conditions are defined according to (5.3). As was for the two-dimensional case, we still suppose to have not the absorbing and the Neumann part on the external boundary, i.e., $\Gamma_{NR} = \Gamma_N = \emptyset$ and $\partial\Omega = \Gamma_D$.

After the first simulation, we have performed another one with non-conforming grids. In this second case, we have chosen different mesh size and spectral degree for $\mathcal{T}^e$ and $\mathcal{T}^a$. In particular, we have $h^e = 0.05$, $h^a = 0.1$, $N^e = 2$, $N^a = 4$. Thus, the global number of nodes in the two subdomains is the same, that should assure the same accuracy for the elastic and the acoustic part. Anyway, since the GLL points are placed differently, the elasto-acoustic interface is non-matching.

We present, in the following Figure 5.13 – 5.16, the numerical solution compared with the exact one, see (5.3), both on conforming and non-conforming meshes. In particular, in Figure 5.13, Figure 5.14 and Figure 5.15 we show the elastic displacement at the point $(-0.6, 0.5, 0.5)$, while in Figure 5.16 we report the acoustic pressure field at $(0.2, 0.5, 0.5)$.
As one can see, both conforming and non-conforming approximation are in good agreement with the exact solution.

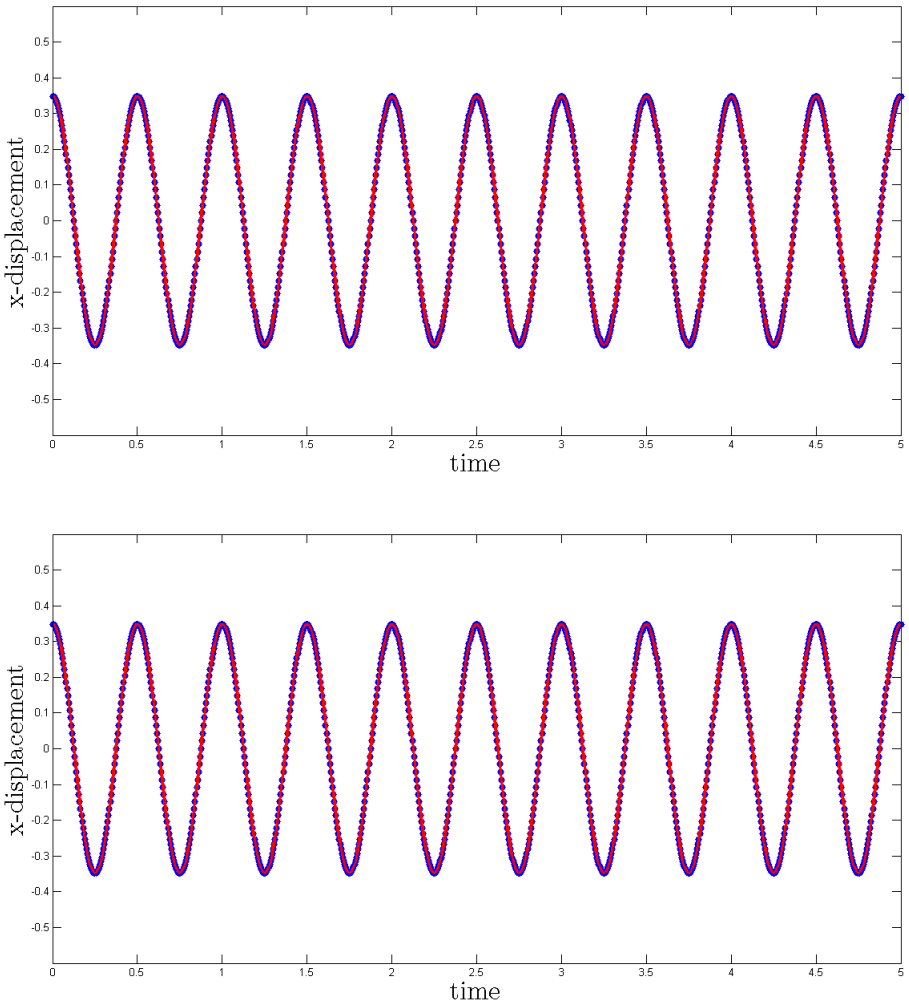

Figure 5.13: Example 3. Elastic x-displacement at point $\mathbf{x} = (-0.6, 0.5, 0.5)$ for conforming (top) and non-conforming (bottom) grids. Numerical results (blue dots $\bullet$) are compared with analytical ones (red line $\sim$).

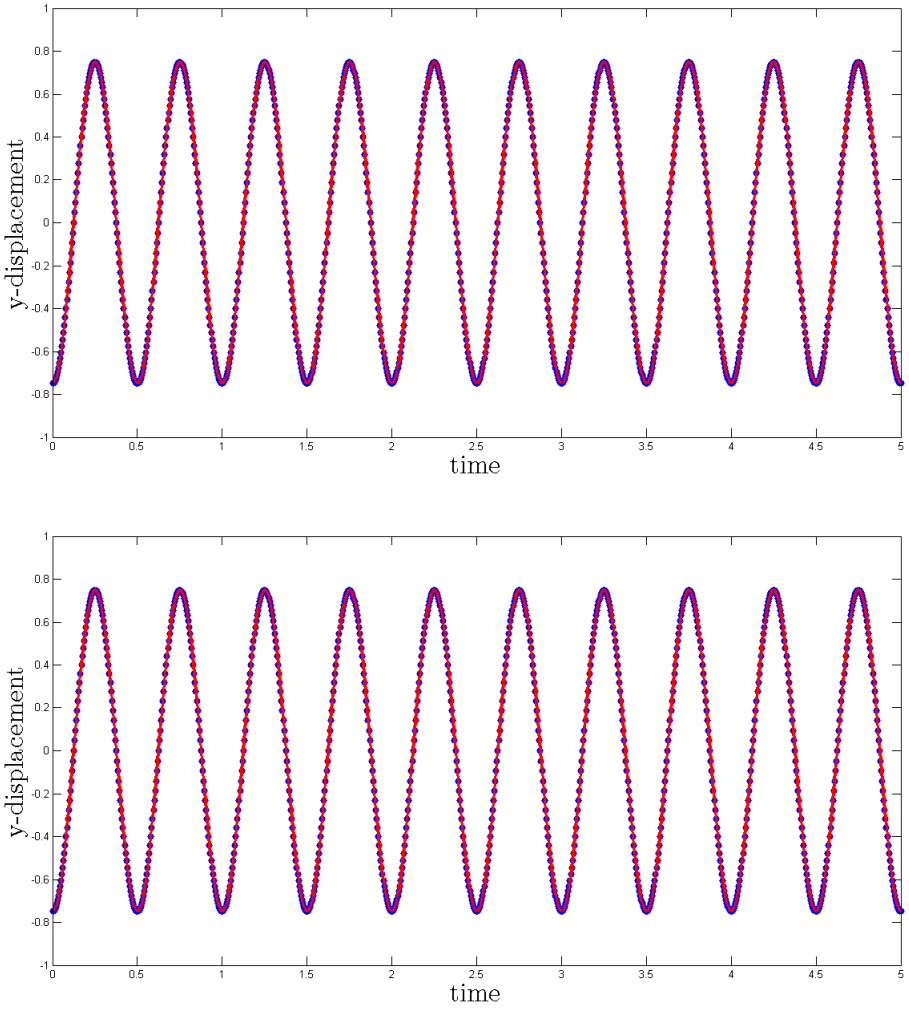

Figure 5.14: Example 3. Elastic y-displacement at point $\mathbf{x} = (-0.6, 0.5, 0.5)$ for conforming (top) and non-conforming (bottom) grids. Numerical results (blue dots $\bullet$) are compared with analytical ones (red line $\sim$).

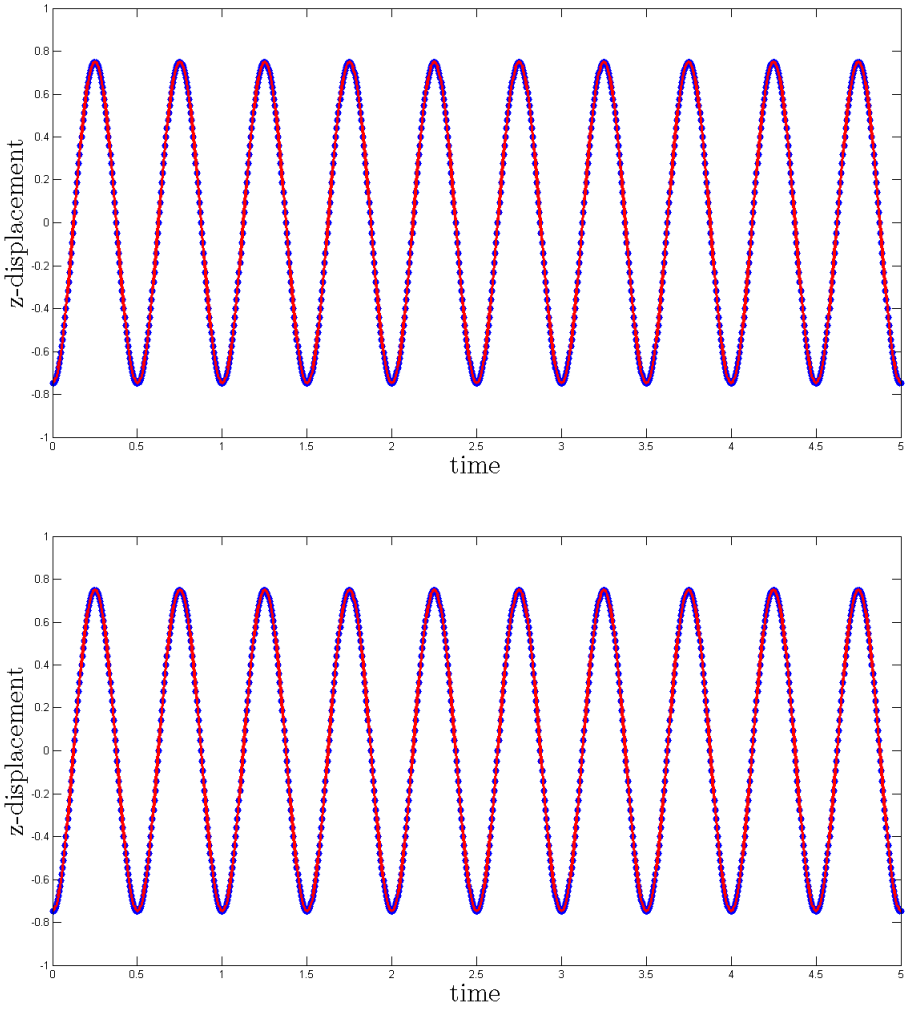

Figure 5.15: Example 3. Elastic z-displacement at point $\mathbf{x} = (-0.6, 0.5, 0.5)$ for conforming (top) and non-conforming (bottom) grids. Numerical results (blue dots $\bullet$) are compared with analytical ones (red line $\sim$).

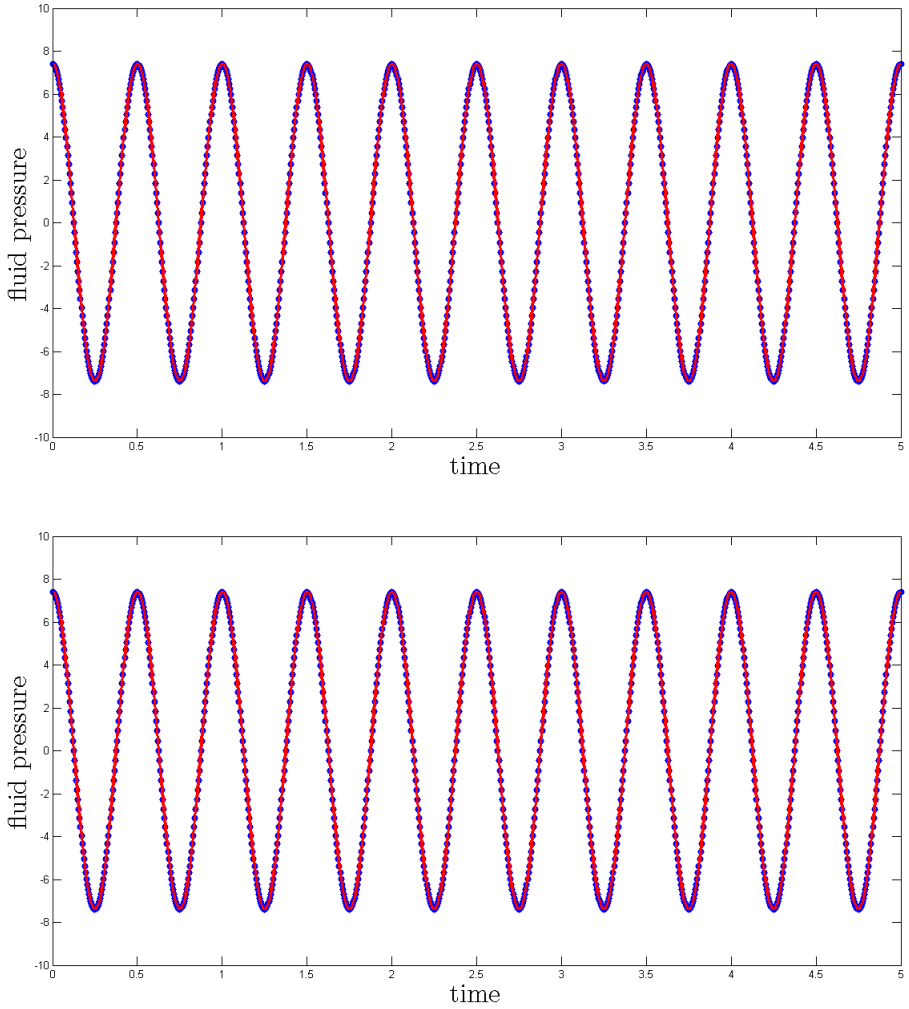

Figure 5.16: example 3. Acoustic pressure field at point $\mathbf{x} = (0.2, 0.5, 0.5)$ for conforming (top) and non-conforming (bottom) grids. Numerical results (blue dots •) are compared with analytical ones (red line ∼).

Example 4. Simulated seismogram

In this last example, we propose a three-dimensional benchmark application. It concerns on the simulation of an earthquake in a cubic domain of elastic material. We investigate the propagation of the elastic wave induced by the earthquake and, in particular, we analyze the differences introduced by the presence of a layer of acoustic material at the half of the domain.
Figure 5.17 (left) shows the computational domain of interest. We consider the cube $(-1,1)^3$, made up by the same elastic material introduced in the previous test case, that is characterized by the dimensionless quantities $\rho^e = 2.7$, $c_p = 6.2$ and $c_s = 3.12$. The earthquake is generated by assigning a seismic moment source in the hypocentre $\mathbf{x_H} = (0, -0.8, 0)$, with a fault plane of normal vector $(0, 0, 1)$. The time history is given by a Ricker function with the same parameters of the one that we have introduced in (5.2). As it shown in Figure 5.17 (right), the domain Ω presents a layer of fluid material for $-0.2 \leq y \leq 0.2$. The mechanical properties of this fluid are the same of the previous case, i.e., $\rho^a = 1$ and $c = 1$.

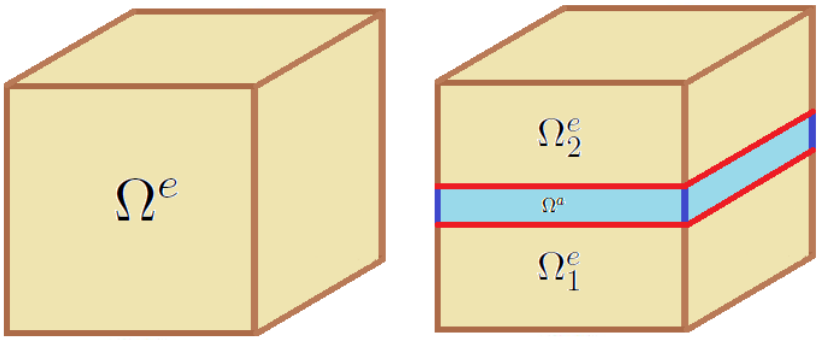

Figure 5.17: Example 4. On the left, cubic elastic domain $\Omega = \Omega^e = (-1,1)^3$. On the right, multiphysical domain $\Omega = \Omega^e \cup \Omega^a$, where $\Omega^e = \Omega_1^e \cup \Omega_2^e$.

We define $\Omega_1^e = (-1,1)\times(-1,-0.2)\times(-1,1)$ and $\Omega_2^e = (-1,1)\times(0.2,1)\times(-1,1)$. We introduce two partitions $\mathcal{T}_1^e$ and $\mathcal{T}_2^e$ for the respective elastic macro-region, with a typical mesh size $h_1^e = h_2^e = 0.1$ and a polynomial approximation degree $N_1^e = N_2^e = 4$. The two internal DG elasto-acoustic interfaces are conforming in the solid and fluid part, since we choose for the acoustic partition $\mathcal{T}^a$ a mesh size $h^a = 0.1$ and a polynomial approximation degree $N^a = 4$.
We apply zero-order non-reflecting boundary conditions on the whole external boundary, i.e., $\Gamma_D = \Gamma_N = \emptyset$ and $\partial\Omega = \Gamma_{NR}$. Moreover, we consider zero initial conditions for displacement and pressure (and their respective time

derivatives).
We choose as a final observation time $T = 6$, with a time step $\Delta t = 0.0005$.

We choose three points of the computational domain and set $A = (0, 0.8, 0)$, $B = (0.2, 0.8, 0.2)$ and $C = (-0.5, 0.8, -0.5)$. Then, we show the elastic displacement at points A, B and C in Figure 5.18, 5.19 and 5.20, respectively. In each plot we compare the "purely elastic" case (cfr. Figure 5.17, left) and the "elasto-acoustic" one (cfr. Figure 5.17, right), in order to analyze the differences and thus the effect of introducing a layer of acoustic material in the elastic domain.

Looking on the elastic case, we see that, around time $t = 1$, the Ricker function has a sort of impulse (see Figure 5.9), which generates a perturbation in the displacement. When we introduce the acoustic layer, the consequences are, substantially, two. The first one is that the perturbation of the elastic displacement at the same points is now delayed of a small time, this is due to the fact that the acoustic speed wave c is less than the velocities c_p and c_s of elastic P and S-waves, respectively. The second one is that, in presence of the fluid, the amplitude of the perturbation of the elastic displacement is definitely reduced with respect to the previous case. Indeed in this case only longitudinal stresses are propagated by the fluid, since it does not support the shear ones. This clearly turns out in a reduction of the consequent deformation of the elastic structure.

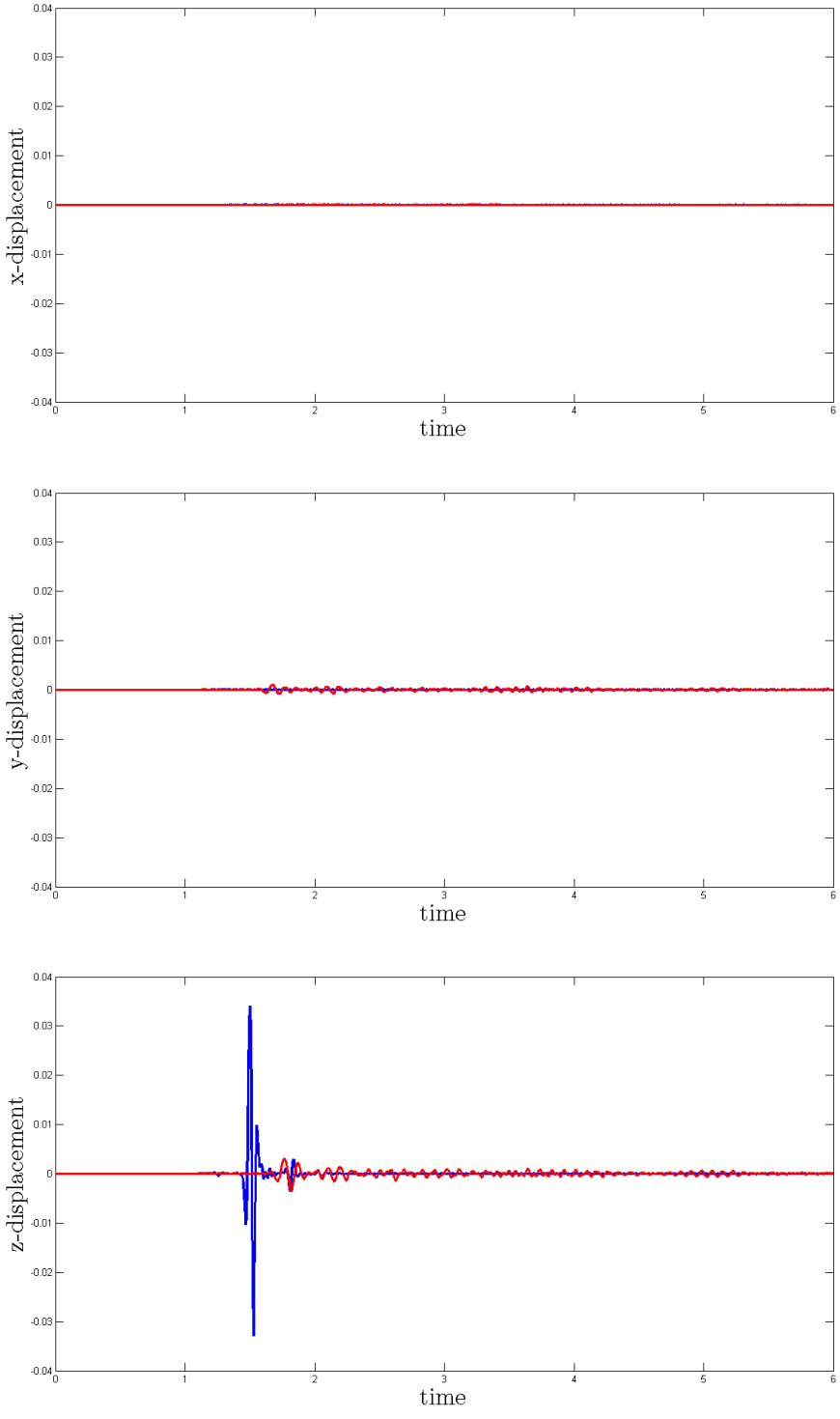

Figure 5.18: Example 4. Elastic displacement at the point $(0, 0.8, 0)$. We compare the "purely elastic" case (blue) with the "elasto-acoustic" one (red).

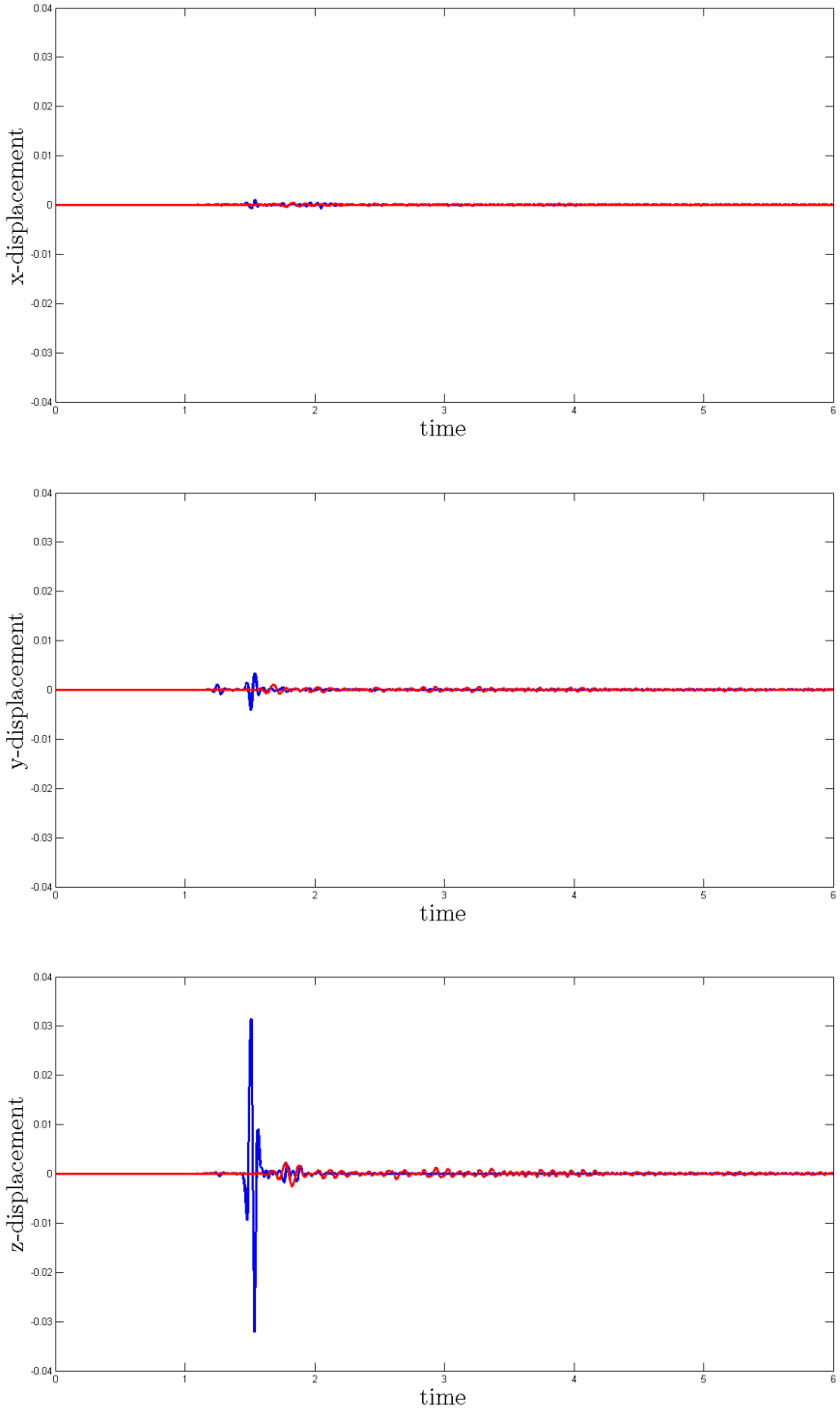

Figure 5.19: Example 4. Elastic displacement at the point $(0.2, 0.8, 0.2)$. We compare the "purely elastic" case (blue) with the "elasto-acoustic" one (red).

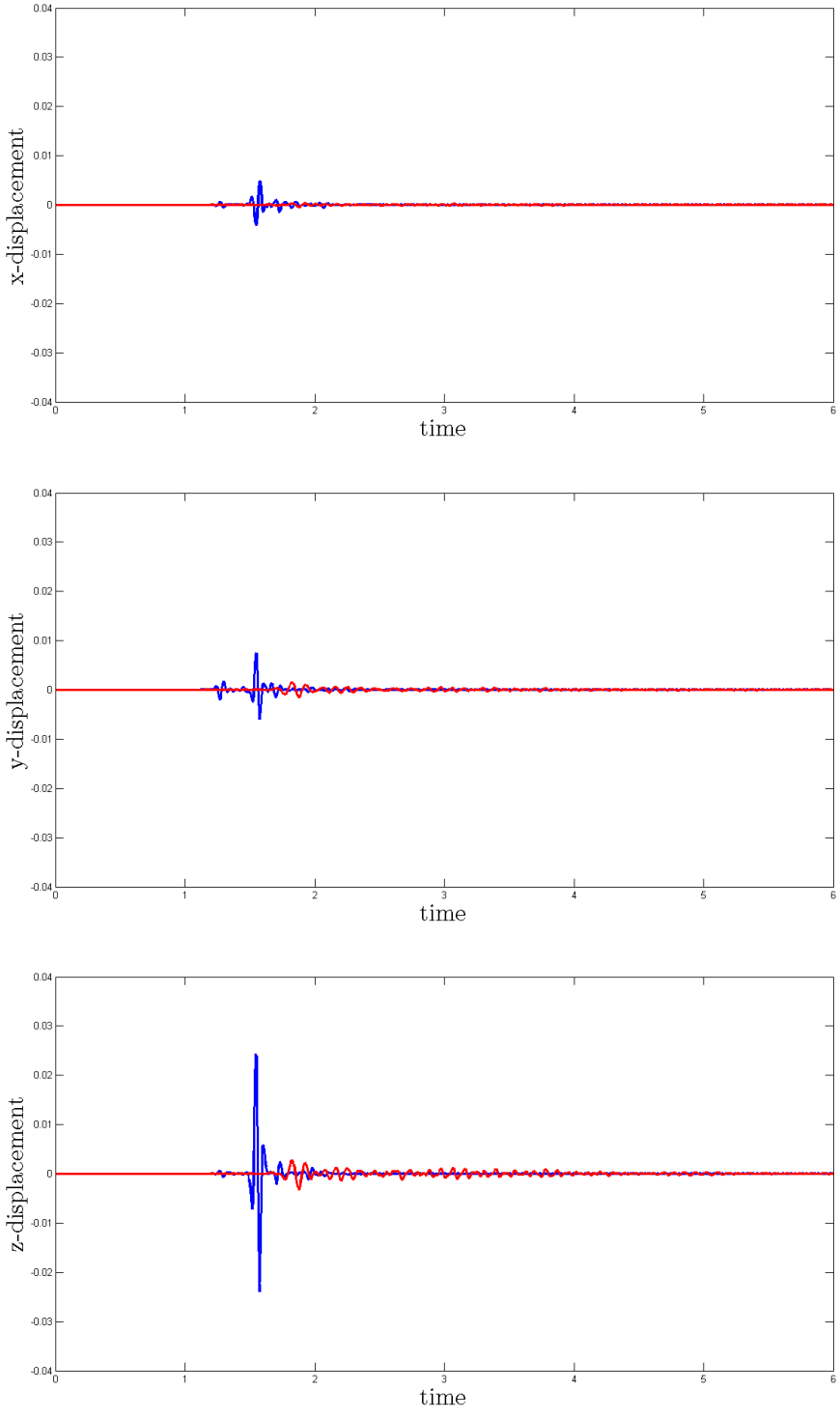

Figure 5.20: Example 4. Elastic displacement at the point $(-0.5, 0.8, -0.5)$. We compare the "purely elastic" case (blue) with the "elasto-acoustic" one (red).

Conclusions and perspectives

The Discontinuous Galerkin Spectral Element method is a high-order numerical technique well suited for seismic wave propagation in heterogeneous media. The possibility of treating non-conforming subdomain partitions where both the mesh size and the spectral degree can be independently tuned make this method really flexible and accurate.
Starting from the main governing equations of the phenomena under consideration, we have employed a multi-phase numerical model able to simulate wave propagation both in solid and fluid media in two and three-dimensional settings. The more innovative and complex feature explained in this thesis is the elasto-acoustic coupling applied in a DG framework. As presented in Chapter 4, the DGSE numerical implementation gives reliable results, which are in agreement with physical observations. We have validated the method and, for the two-dimensional code, we have also investigated the order of convergence with respect to space and time discretization parameters.
Several further developments are possible, both at a theoretical and numerical level. Possible future numerical perspectives go toward the simulation of more realistic earthquake scenarios in domains which involve both the elastic and the acoustic part (for example, ground and water). Moreover, we should test the code performance and its scalability when it works in parallel on a multi-core setting.
On the other hand, at a theoretical level, the well-position and the stability analysis should be more investigated, especially for the DGSE semi-discrete formulation. Moreover, we should study the discretization error analysis, in order to explain the "non-optimal" behavior of the algebraic convergence with respect to the mesh size.
Further applications may involve the seismic response of dams or, in a different contest, the acoustic comfort of specific environments which involve solid-fluid interaction, such as cars, racing helmets or rooms.

Appendix A

Numerical integration

We give here some details about the algorithmic aspects of the DGSE method, describing its implementation in SPEED (https://speed.mox.polimi.it).
In particular, we focus on the strategy employed for computing the interface integrals related to the bilinear forms $\mathcal{B}^e(\cdot,\cdot)$, $\mathcal{C}^e(\cdot,\cdot)$ and $\mathcal{C}^a(\cdot,\cdot)$, that are associated to the matrices B^e, C^e, C^a in the algebraic formulation (3.1) – (3.2). We detail the presentation in a two-dimensional setting, for sake of simplicity. The same arguments are applied in a three-dimensional setting.

We recall that, from equation (2.5), we have

$$\begin{aligned}\mathcal{B}^e(\boldsymbol{\Psi}_i^{e,1(2)},\boldsymbol{\Psi}_j^{e,1(2)})_{\gamma_m^e} = &-\big(\{\sigma(\boldsymbol{\Psi}_i^{e,1(2)})\},[\![\boldsymbol{\Psi}_j^{e,1(2)}]\!]\big)_{\gamma_m^e}\\ &+\theta\big([\![\boldsymbol{\Psi}_i^{e,1(2)}]\!],\{\sigma(\boldsymbol{\Psi}_j^{e,1(2)})\}\big)_{\gamma_m^e}\\ &+\eta_{\gamma_m^e}\big([\![\boldsymbol{\Psi}_i^{e,1(2)}]\!],[\![\boldsymbol{\Psi}_j^{e,1(2)}]\!]\big)_{\gamma_m^e}.\end{aligned}$$

We now denote by Ω^+ and Ω^- the two elastic macro-regions which share the edge γ_m^e on the internal skeleton $\mathcal{S}^e$ (see Figure A.1). We use the definitions (2.3) – (2.4) of the operators $[\![\cdot]\!]$ and $\{\cdot\}$ and the structure of the Cauchy stress tensor, in order to rewrite each integral that appears in the previous formula as the combination of the following "elementary" terms

$$\begin{aligned}\big(\partial_{x_1}\Psi_j^{\pm},\Psi_i^{\pm}\big)_{\gamma_m^e} &= \int_{\gamma_m^e}\partial_{x_1}\Psi_j^{\pm}\cdot\Psi_i^{\pm}d\gamma,\\ \big(\partial_{x_2}\Psi_j^{\pm},\Psi_i^{\pm}\big)_{\gamma_m^e} &= \int_{\gamma_m^e}\partial_{x_2}\Psi_j^{\pm}\cdot\Psi_i^{\pm}d\gamma,\\ \big(\partial_{x_1}\Psi_j^{\pm},\Psi_i^{\mp}\big)_{\gamma_m^e} &= \int_{\gamma_m^e}\partial_{x_1}\Psi_j^{\pm}\cdot\Psi_i^{\mp}d\gamma,\\ \big(\partial_{x_2}\Psi_j^{\pm},\Psi_i^{\mp}\big)_{\gamma_m^e} &= \int_{\gamma_m^e}\partial_{x_2}\Psi_j^{\pm}\cdot\Psi_i^{\mp}d\gamma.\end{aligned}\tag{A.1}$$

We then use the fact that both Ω^+ and $\Omega-$ are the images of the reference element $\widehat{\Omega} = [-1,1]^2$ through a suitable bilinear $\mathbf{F}^+$ and $\mathbf{F}^-$, respectively. More precisely, $\mathbf{F}^{\pm}(\xi,\eta) = (x_1^{\pm}(\xi,\eta), x_2^{\pm}(\xi,\eta))$.
Therefore, it holds

$$\begin{aligned}\partial_\xi \Psi_i^{\pm} &= \partial_\xi x_1^{\pm} \partial_{x_1} \Psi_i^{\pm} + \partial_\xi x_2^{\pm} \partial_{x_2} \Psi_i^{\pm},\\ \partial_\eta \Psi_i^{\pm} &= \partial_\eta x_1^{\pm} \partial_{x_1} \Psi_i^{\pm} + \partial_\eta x_2^{\pm} \partial_{x_2} \Psi_i^{\pm}.\end{aligned}$$

We call $J^{\pm} = \partial_\xi x_1^{\pm} \partial_\eta x_2^{\pm} - \partial_\eta x_1^{\pm} \partial_\xi x_2^{\pm}$ the Jacobian of the transformation $\mathbf{F}^{\pm}$. We thus have

$$\begin{aligned}\partial_{x_1} \Psi_i^{\pm} &= \frac{1}{|J^{\pm}|}\big(\partial_\eta x_2^{\pm} \partial_\xi \Psi_i^{\pm} - \partial_\xi x_2^{\pm} \partial_\eta \Psi_i^{\pm}\big),\\ \partial_{x_2} \Psi_i^{\pm} &= \frac{1}{|J^{\pm}|}\big(\partial_\xi x_1^{\pm} \partial_\eta \Psi_i^{\pm} - \partial_\eta x_1^{\pm} \partial_\xi \Psi_i^{\pm}\big).\end{aligned}$$

Then, we can rewrite the "elementary" integrals (A.1) as follows

$$\begin{aligned}\big(\partial_{x_1} \Psi_j^{\pm}, \Psi_i^{\pm}\big)_{\gamma_m^e} &= \big(\partial_\eta x_2^{\pm} \partial_\xi \Psi_j^{\pm} - \partial_\xi x_2^{\pm} \partial_\eta \Psi_j^{\pm}, \Psi_i^{\pm}\big)_{\widehat{\gamma}_m^{e,\pm}},\\ \big(\partial_{x_2} \Psi_j^{\pm}, \Psi_i^{\pm}\big)_{\gamma_m^e} &= \big(\partial_\xi x_1^{\pm} \partial_\eta \Psi_j^{\pm} - \partial_\eta x_1^{\pm} \partial_\xi \Psi_j^{\pm}, \Psi_i^{\pm}\big)_{\widehat{\gamma}_m^{e,\pm}},\\ \big(\partial_{x_1} \Psi_j^{\pm}, \Psi_i^{\mp}\big)_{\gamma_m^e} &= \big(\partial_\eta x_2^{\pm} \partial_\xi \Psi_j^{\pm} - \partial_\xi x_2^{\pm} \partial_\eta \Psi_j^{\pm}, \Psi_i^{\mp}\big)_{\widehat{\gamma}_m^{e,\pm}},\\ \big(\partial_{x_2} \Psi_j^{\pm}, \Psi_i^{\mp}\big)_{\gamma_m^e} &= \big(\partial_\xi x_1^{\pm} \partial_\eta \Psi_j^{\pm} - \partial_\eta x_1^{\pm} \partial_\xi \Psi_j^{\pm}, \Psi_i^{\mp}\big)_{\widehat{\gamma}_m^{e,\pm}},\end{aligned}$$

where $\gamma_m^e = \mathbf{F}^{\pm}(\widehat{\gamma}_m^{e,\pm})$. These integrals are computed using a GLL quadrature rule with N_e^* nodes, where N_e^* is chosen such that the GLL quadrature formula is exact for the integrand under consideration. Thus, they are replaced with finite sums as shown in the following, i.e.,

$$\begin{aligned}&\big(\partial_\eta x_2^{\pm} \partial_\xi \Psi_j^{\pm} - \partial_\xi x_2^{\pm} \partial_\eta \Psi_j^{\pm}, \Psi_i^{\pm}\big)_{\widehat{\gamma}_m^{\pm}} =\\ &\qquad = \frac{|\widehat{\gamma}_m^{e,\pm}|}{2} \sum_{k=1}^{N_e^*} \big(\partial_\eta x_2^{\pm} \partial_\xi \Psi_j^{\pm} - \partial_\xi x_2^{\pm} \partial_\eta \Psi_j^{\pm}\big)(\mathbf{p}_k) \Psi_i^{\pm}(\mathbf{p}_k) \alpha_k,\\ &\big(\partial_\xi x_1^{\pm} \partial_\eta \Psi_j^{\pm} - \partial_\eta x_1^{\pm} \partial_\xi \Psi_j^{\pm}, \Psi_i^{\pm}\big)_{\widehat{\gamma}_m^{e,\pm}} =\\ &\qquad = \frac{|\widehat{\gamma}_m^{e,\pm}|}{2} \sum_{k=1}^{N_e^*} \big(\partial_\xi x_1^{\pm} \partial_\eta \Psi_j^{\pm} - \partial_\eta x_1^{\pm} \partial_\xi \Psi_j^{\pm}\big)(\mathbf{p}_k) \Psi_i^{\pm}(\mathbf{p}_k) \alpha_k,\\ &\big(\partial_\eta x_2^{\pm} \partial_\xi \Psi_j^{\pm} - \partial_\xi x_2^{\pm} \partial_\eta \Psi_j^{\pm}, \Psi_i^{\mp}\big)_{\widehat{\gamma}_m^{e,\pm}} =\\ &\qquad = \frac{|\widehat{\gamma}_m^{e,\pm}|}{2} \sum_{k=1}^{N_e^*} \big(\partial_\eta x_2^{\pm} \partial_\xi \Psi_j^{\pm} - \partial_\xi x_2^{\pm} \partial_\eta \Psi_j^{\pm}\big)(\mathbf{p}_k) \Psi_i^{\mp}(\mathbf{p}_k) \alpha_k,\\ &\big(\partial_\xi x_1^{\pm} \partial_\eta \Psi_j^{\pm} - \partial_\eta x_1^{\pm} \partial_\xi \Psi_j^{\pm}, \Psi_i^{\mp}\big)_{\widehat{\gamma}_m^{e,\pm}} =\\ &\qquad = \frac{|\widehat{\gamma}_m^{e,\pm}|}{2} \sum_{k=1}^{N_e^*} \big(\partial_\xi x_1^{\pm} \partial_\eta \Psi_j^{\pm} - \partial_\eta x_1^{\pm} \partial_\xi \Psi_j^{\pm}\big)(\mathbf{p}_k) \Psi_i^{\mp}(\mathbf{p}_k) \alpha_k,\end{aligned}$$

where $\{\mathbf{p}_k\}_{k=1}^{N_e^*}$ are the GLL quadrature points, which are defined on the segment $\widehat{\gamma}_m^{e,\pm} \subset \partial\widehat{\Omega}$, and α_k are the corresponding GLL quadrature weights.

Next, we recall equations (2.6) – (2.7),

$$\mathcal{C}^e(\Psi_j^a, \mathbf{\Psi}_i^{e,1(2)})_{\gamma_n^{ea}} = -\big(\Psi_j^a \mathbf{n}^a, \mathbf{\Psi}_i^{e,1(2)}\big)_{\gamma_n^{ea}} = \big(\Psi_j^a \mathbf{n}^e, \mathbf{\Psi}_i^{e,1(2)}\big)_{\gamma_n^{ea}},$$
$$\mathcal{C}^a(\mathbf{\Psi}_j^{e,1(2)}, \Psi_i^a)_{\gamma_n^{ea}} = -\big(\partial_{tt}\mathbf{\Psi}_j^{e,1(2)} \cdot \mathbf{n}^e, \Psi_i^a\big)_{\gamma_n^{ea}} = \big(\partial_{tt}\mathbf{\Psi}_j^{e,1(2)} \cdot \mathbf{n}^a, \Psi_i^a\big)_{\gamma_n^{ea}}.$$

With the same notation adopted before, we now call Ω^+ and Ω^- two neighbouring element which share the edge γ_n^{ea} on the elasto-acoustic interface Γ^i (see Figure A.1). As we did for the DG elastic interface, we can split the computation of the coupling integrals above into a combination of the following "elementary" terms

$$\big(\Psi_j^{\pm} n_1^{\mp}, \Psi_i^{\mp}\big)_{\gamma_n^{ea}} = \int_{\gamma_n^{ea}} \Psi_j^{\pm} n_1^{\mp} \cdot \Psi_i^{\mp} d\gamma,$$
$$\big(\Psi_j^{\pm} n_2^{\mp}, \Psi_i^{\mp}\big)_{\gamma_n^{ea}} = \int_{\gamma_n^{ea}} \Psi_j^{\pm} n_2^{\mp} \cdot \Psi_i^{\mp} d\gamma.$$

Repeating the same procedure described previously, we can evaluate these integrals with a numerical technique based on N_{ea}^* GLL quadrature nodes. Thus, we have

$$\big(\Psi_j^{\pm} n_1^{\mp}, \Psi_i^{\mp}\big)_{\gamma_n^{ea}} = \frac{|\widehat{\gamma}_n^{ea,\pm}|}{2} \sum_{k=1}^{N_{ea}^*} \big(\Psi_j^{\pm} n_1^{\mp}\big)(\mathbf{p}_k) \Psi_i^{\mp}(\mathbf{p}_k) J^{\pm}(\mathbf{p}_k) \alpha_k,$$
$$\big(\Psi_j^{\pm} n_2^{\mp}, \Psi_i^{\mp}\big)_{\gamma_m^{e}} = \frac{|\widehat{\gamma}_n^{ea,\pm}|}{2} \sum_{k=1}^{N_{ea}^*} \big(\Psi_j^{\pm} n_2^{\mp}\big)(\mathbf{p}_k) \Psi_i^{\mp}(\mathbf{p}_k) J^{\pm}(\mathbf{p}_k) \alpha_k,$$

where $\gamma_n^{ea} = \mathbf{F}^{\pm}(\widehat{\gamma}_n^{ea,\pm})$. The GLL quadrature points $\{\mathbf{p}_k\}_{k=1}^{N_{ea}^*}$ are defined on the segment $\widehat{\gamma}_n^{ea,\pm} \subset \partial\widehat{\Omega}$ and the corresponding GLL quadrature weights are still α_k.

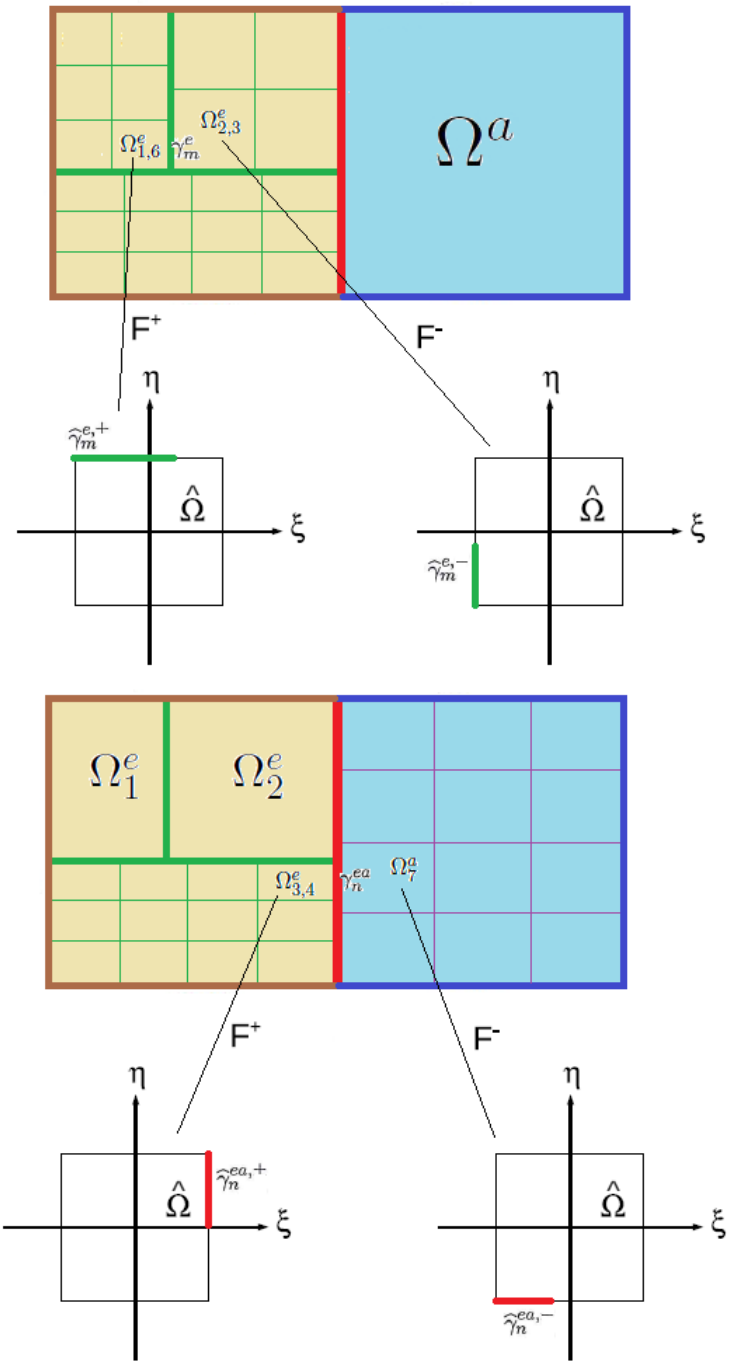

Figure A.1: Example of domain decomposition for DGSE discretization. In this case $\gamma^e_m = \partial\Omega^e_{1,6} \cap \partial\Omega^e_{2,3}$ and $\gamma^{ea}_n = \partial\Omega^e_{3,4} \cap \partial\Omega^a_7$.

Bibliography

[1] R. A. Adams and J. J. F. Fournier. *Sobolev spaces*, volume 140 of *Pure and Applied Mathematics*. Elsevier, Amsterdam, second edition, 2003.

[2] P. F. Antonietti, B. Ayuso de Dios, I. Mazzieri, and A. Quarteroni. Stability analysis for Discontinuous Galerkin approximations to the elastodynamics problem. *SIAM Journal on Scientific*, 2015.

[3] D. N. Arnold, F. Brezzi, B. Cockburn, and L. D. Marini. Unified analysis of discontinuous Galerkin methods for elliptic problems. *SIAM Journal on Numerical Analysis*, 39(5):1749–1779, 2001/02.

[4] H. Bao, J. Bielak, O. Ghattas, L. F. Kallivokas, D. R. O'Hallaron, J. R. Shewchuk, and J. Xu. Large-scale simulation of elastic wave propagation in heterogeneous media on parallel computers. *Computer Methods in Applied Mechanics and Engineering*, 152(1–2):85 – 102, 1998.

[5] H. Barucq, R. Djellouli, and E. Estecahandy. Efficient dg-like formulation equipped with curved boundary edges for solving elasto-acoustic scattering problems. *International Journal for Numerical Methods in Engineering*, 98(10):747–780, 2014.

[6] A. Bermudez, L. Hervella-Nieto, and R. Rodriguez. Finite element computation of three-dimensional elastoacoustic vibrations. *Journal of Sound and Vibration*, 219(2):279 – 306, 1999.

[7] A. Bermudez, R. Rodriguez, and D. Santamarina. Finite element approximation of a displacement formulation for time-domain elastoacoustic vibrations. *Journal of Computational and Applied Mathematics*, 152(1–2):17 – 34, 2003.

[8] D. Brunner, M. Junge, and L. Gaul. A comparison of fe–be coupling schemes for large-scale problems with fluid–structure interaction. *International Journal for Numerical Methods in Engineering*, 77(5):664–688, 2009.

[9] C. Canuto, M. Y. Hussaini, A. Quarteroni, and T. A. Zang. *Spectral methods - Fundamentals in single domains*. Scientific Computation. Springer-Verlag, Berlin, 2006.

[10] C. Canuto, M. Y. Hussaini, A. Quarteroni, and T. A. Zang. *Spectral methods - Evolution to complex geometries and applications to fluid dynamics*. Scientific Computation. Springer, Berlin, 2007.

[11] F. Casadei, E. Gabellini, G. Fotia, F. Maggio, and A. Quarteroni. A mortar spectral/finite element method for complex 2D and 3D elastodynamic problems. *Computer Methods in Applied Mechanics and Engineering*, 191(45):5119–5148, 2002.

[12] E. Chaljub, Y. Capdeville, and J.-P. Vilotte. Solving elastodynamics in a fluid-solid heterogeneous sphere: a parallel spectral element approximation on non-conforming grids. *Journal of Computational Physics*, 187(2):457–491, 2003.

[13] E. Chaljub, D. Komatitsch, J.-P. Vilotte, Y. Capdeville, B. Valette, and G. Festa. Spectral element analysis in seismology. In Ru-Shan Wu and Valérie Maupin, editors, *Advances in wave propagation in heterogeneous media*, volume 48 of *Advances in Geophysics*, pages 365–419. Elsevier - Academic Press, London, UK, 2007.

[14] G. C. Cohen. *Higher-order numerical methods for transient wave equations*. Scientific Computation. Springer-Verlag, Berlin, 2002.

[15] J. De Basabe and M. K. Sen. Stability of the high-order finite elements for acoustic or elastic wave propagation with high-order time stepping. *Geophysical Journal International*, 181(1):577–590, 2010.

[16] J. De Basabe and M. K. Sen. A comparison of finite-difference and spectral-element methods for elastic wave propagation in media with a fluid-solid interface. *Geophysical Journal International*, 200(1):278–298, 2015.

[17] J. De Basabe, M. K. Sen, and M. F. Wheeler. The interior penalty discontinuous Galerkin method for elastic wave propagation: grid dispersion. *Geophysical Journal International*, 175(1):83–93, 2008.

[18] J. de la Puente, M. Käser, M. Dumbser, and H. Igel. An Arbitrary High Order Discontinuous Galerkin Method for Elastic Waves on Unstructured Meshes IV: Anisotropy. *Geophysical Journal International*, 169(3):1210–1228, 2007.

[19] J. Diaz and M. J. Grote. Energy conserving explicit local time stepping for second-order wave equations. *SIAM Journal on Scientific*, 31(3):1985–2014, 2009.

[20] G. Duvaut and J.-L. Lions. *Inequalities in mechanics and physics*. Springer-Verlag, Berlin, 1976. Translated from the French by C. W. John, Grundlehren der Mathematischen Wissenschaften, 219.

[21] E. Faccioli, F. Maggio, R. Paolucci, and A. Quarteroni. 2d and 3d elastic wave propagation by a pseudo-spectral domain decomposition method. *Journal of Seismology*, 1(3):237–251, 1997.

[22] B. Flemisch, M. Kaltenbacher, S. Triebenbacher, and B. I. Wohlmuth. The equivalence of standard and mixed finite element methods in applications to elasto-acoustic interaction. *SIAM Journal on Scientific Computing*, 32(4):1980–2006, 2010.

[23] B. Flemisch, M. Kaltenbacher, and B. I. Wohlmuth. Elasto–acoustic and acoustic–acoustic coupling on non-matching grids. *International Journal for Numerical Methods in Engineering*, 67(13):1791–1810, 2006.

[24] M. J. Grote, A. Schneebeli, and D. Schötzau. Discontinuous Galerkin finite element method for the wave equation. *SIAM Journal on Numerical Analysis*, 44(6):2408–2431, 2006.

[25] J. S. Hesthaven and T. Warburton. *Nodal discontinuous Galerkin methods*, volume 54 of *Texts in Applied Mathematics*. Springer, Berlin, 2008.

[26] G. C. Hsiao, F.-J. Sayas, and R. J. Weinacht. Time-dependent fluid-structure interaction. *Mathematical Methods in the Applied Sciences*, 2015.

[27] M. Käser and M. Dumbser. An Arbitrary High Order Discontinuous Galerkin Method for Elastic Waves on Unstructured Meshes I: The Two-Dimensional Isotropic Case with External Source Terms. *Geophysical Journal International*, 166(2):855–877, 2006.

[28] D. Komatitsch, C. Barnes, and J. Tromp. Wave propagation near a fluid-solid interface: A spectral-element approach. *Geophysics*, 65(2):623–631, 2000.

[29] D. Komatitsch, J. Ritsema, and J. Tromp. The spectral-element method, Beowulf computing, and global seismology. *Science*, 298(5599):1737–1742, 2002.

[30] D. Komatitsch and J. Tromp. Introduction to the spectral-element method for 3-D seismic wave propagation. *Geophysical Journal International*, 139(3):806–822, 1999.

[31] D. Komatitsch, S. Tsuboi, and J. Tromp. The spectral-element method in seismology. In Alan Levander and Guust Nolet, editors, *Seismic Earth: Array Analysis of Broadband Seismograms*, volume 157 of *Geophysical Monograph*, pages 205–228. American Geophysical Union, Washington DC, USA, 2005.

[32] D. Komatitsch and J.-P. Vilotte. The spectral-element method: an efficient tool to simulate the seismic response of 2D and 3D geological

structures. *Bulletin of the Seismological Society of America*, 88(2):368–392, 1998.

[33] J. D. Lambert. *Numerical Methods for Ordinary Differential Systems: The Initial Value Problem*. John Wiley & Sons, Inc., New York, NY, USA, 1991.

[34] H.-Y. Lee, S.-C. Lim, D.-J. Min, B.-D. Kwon, and M. Park. 2d time-domain acoustic-elastic coupled modeling: a cell-based finite-difference method. *Geosciences Journal*, 13(4):407–414, 2009.

[35] Y. Luo, J. Tromp, B. Denel, and H. Calandra. 3d coupled acoustic-elastic migration with topography and bathymetry based on spectral-element and adjoint methods. *Geophysics*, 78(4):S193–S202, 2013.

[36] E. D. Mercerat, J.-P. Vilotte, and F. J. Sànchez-Sesma. Triangular spectral element simulation of two-dimensional elastic wave propagation using unstructured triangular grids. *Geophysical Journal International*, 166(2):679–698, 2006.

[37] F. Nataf. Absorbing boundary conditions and perfectly matched layers in wave propagation problems. In *Direct and Inverse problems in Wave Propagation and Applications*, volume 14, pages 219–231. 2013.

[38] T. Nissen-Meyer, A. Fournier, and F. A. Dahlen. A 2-d spectral-element method for computing spherical-earth seismograms—ii. waves in solid–fluid media. *Geophysical Journal International*, 174(3):873–888, 2008.

[39] A. Quarteroni. *Numerical models for differential problems*, volume 8 of *MS&A. Modeling, Simulation and Applications*. Springer-Verlag Italia, Milan, 2014.

[40] A. Quarteroni and A. Valli. *Numerical approximation of partial differential equations*, volume 23 of *Springer Series in Computational Mathematics*. Springer-Verlag, Berlin, 1994.

[41] P.-A. Raviart and J.-M. Thomas. *Introduction à l'analyse numérique des équations aux dérivées partielles*. Collection Mathématiques Appliquées pour la Maîtrise. Masson, Paris, 1983.

[42] B. Rivière. *Discontinuous Galerkin methods for solving elliptic and parabolic equations - Theory and implementation*, volume 35 of *Frontiers in Applied Mathematics*. Society for Industrial and Applied Mathematics (SIAM), Philadelphia, PA, 2008.

[43] B. Rivière, S. Shaw, M. F. Wheeler, and J. R. Whiteman. Discontinuous Galerkin finite element methods for linear elasticity and quasistatic linear viscoelasticity. *Numerische Mathematik*, 95(2):347–376, 2003.

[44] B. Rivière, S. Shaw, and J. R. Whiteman. Discontinuous Galerkin finite element methods for dynamic linear solid viscoelasticity problems. *Numerical Methods for Partial Differential Equations*, 23(5):1149–1166, 2007.

[45] B. Rivière and M. F. Wheeler. Discontinuous finite element methods for acoustic and elastic wave problems. In *Current trends in scientific computing (Xi'an, 2002)*, volume 329 of *Contemporary Mathematics*, pages 271–282. Amer. Math. Soc., Providence, RI, 2003.

[46] G. Seriani, E. Priolo, and A. Pregarz. Modelling waves in anisotropic media by a spectral element method. In G. Cohen, editor, *Proceedings of the third international conference on mathematical and numerical aspects of wave propagation*, pages 289–298. SIAM, Philadephia, PA, 1995.

[47] R. Stacey. Improved transparent boundary formulations for the elastic-wave equation. *Bullettin of the Seismological Society of America*, 78(6):2089–2097, 1988.

[48] M. Stupazzini, R. Paolucci, and H. Igel. Near-fault earthquake ground-motion simulation in the grenoble valley by a high-performance spectral element code. *Bulletin of the Seismological Society of America*, 99(1):286–301, 2009.

[49] L. C. Wilcox, G. Stadler, C. Burstedde, and O. Ghattas. A high-order discontinuous Galerkin method for wave propagation through coupled elastic-acoustic media. *Journal of Computational Physics*, 229(24):9373 – 9396, 2010.